

---

## **Study for the numerical resolution of conservation equations of mass, momentum and energy to be applied to the aerodynamics of airfoil-shaped bodies**

---



**Escola Tècnica Superior d'Enginyeries Industrial i Aeronàutica de Terrassa  
(ETSEIAT)**

---

**Degree:** Aerospace Technologies Engineering (GrETA)

**Date of submission:** 12<sup>th</sup> June 2015 (SPRING)

**Name:** Marc Artola i Magrans

**Director:** Assensi Oliva Llena

**Co-Director:** F. Xavier Trias

## **Abstract**

A set of benchmark problems concerning laminar and incompressible flows are solved by means of self-developed software written in C++ language and based in the Finite Volume Method. This problems include the Smith-Hutton problem, the Lid Driven Cavity and the Differentially Heated Cavity, as well as an approach to turbulence phenomenon with Burgers' equation (in this case spectral methods are to be used).

Developed codes are verified through comparisons with benchmark solutions and through the analysis of the order of accuracy of the obtained results. A specific case of study on external flow analysis is done, including the resolution of a confined flow past a square cylinder aiming to solve flows over more complex geometries such as airfoil-shaped bodies.

Finally, recommendations on how to extend this study to turbulent and compressible flows are presented.

## **Acknowledgements**

Firstly, I would like to thank the CTTC group and the passionate and enthusiast director of my study, Assensi Oliva, for having provided me with the opportunity to discover the fascinating world of CFD.

I wish to offer my special thanks to F. Xavier Trias since he has been the person whom I contacted every time I had a difficulty and has mentored me throughout all the study, as well as for his disinterested lectures and seminars on CFD and turbulence.

Finally, I thank my family, especially my parents who, as always, have put up with my most stressful moments and have given me their unconditional support.

## Table of contents

|          |   |           |
|----------|---|-----------|
| <b>1</b> | <b>Introduction .....</b>   | <b>9</b>  |
| 1.1      | Aim of the study.....   | 9         |
| 1.2      | Background and justification.....                                 | 9         |
| 1.3      | Scope .....   | 11        |
| 1.4      | Specifications .....  | 12        |
| 1.5      | CFD. Finite volume method. Brief review and state of the art..... | 13        |
| 1.5.1    | Brief History .....   | 13        |
| 1.5.2    | Finite Volume Method .....  | 14        |
| 1.5.3    | Approximation process .....                                       | 19        |
| <b>2</b> | <b>2D Transient Conduction Problem.....</b>                       | <b>24</b> |
| 2.1      | Definition of the problem .....                                   | 24        |
| 2.1.1    | General description.....  | 24        |
| 2.1.2    | Nomenclature .....  | 25        |
| 2.1.3    | Governing equations.....  | 25        |
| 2.2      | Numerical methods.....  | 26        |
| 2.2.1    | Time-integration .....  | 26        |
| 2.2.2    | Spatial integration.....  | 26        |
| 2.3      | Results and discussion .....                                      | 28        |
| <b>3</b> | <b>Smith Hutton Problem .....</b>                                 | <b>31</b> |
| 3.1      | Definition of the problem .....                                   | 31        |
| 3.1.1    | General description.....  | 31        |
| 3.1.2    | Nomenclature .....  | 32        |
| 3.1.3    | Governing equations.....  | 32        |
| 3.2      | Numerical methods.....  | 33        |
| 3.2.1    | Time-integration .....  | 33        |
| 3.2.2    | Spatial-integration .....   | 34        |
| 3.3      | Results and discussion .....                                      | 36        |
| 3.3.1    | Case A (CDS) .....  | 36        |
| 3.3.2    | Case B (Upwind) .....   | 38        |
| 3.3.3    | Code verification .....   | 40        |
| <b>4</b> | <b>Lid Driven Cavity.....</b>                                     | <b>41</b> |
| 4.1      | Definition of the problem .....                                   | 41        |

|   |           |
|---|-----------|
| 4.1.1 General description.....                        | 41        |
| 4.1.2 Nomenclature .....                              | 41        |
| 4.1.3 Governing equations.....                        | 42        |
| <b>4.2 Numerical methods.....</b>                     | <b>43</b> |
| 4.2.1 Time-integration .....                          | 43        |
| 4.2.2 Spatial-integration .....                       | 44        |
| <b>4.3 Results and discussion .....</b>               | <b>49</b> |
| 4.3.1 Contour plots .....                             | 50        |
| 4.3.2 Comparison with benchmark solution .....        | 53        |
| 4.3.3 Code verification .....                         | 56        |
| <b>5 Differentially Heated Cavity.....</b>            | <b>58</b> |
| <b>5.1 Definition of the problem .....</b>            | <b>58</b> |
| 5.1.1 General description.....                        | 58        |
| 5.1.2 Nomenclature .....                              | 59        |
| 5.1.3 Governing equations.....                        | 59        |
| <b>5.2 Numerical methods.....</b>                     | <b>61</b> |
| 5.2.1 Time-integration .....                          | 61        |
| 5.2.2 Spatial-integration .....                       | 62        |
| <b>5.3 Results and discussion .....</b>               | <b>65</b> |
| 5.3.1 Contour plots .....                             | 66        |
| 5.3.2 Comparison with benchmark solution .....        | 71        |
| <b>6 Burgers' equation.....</b>                       | <b>73</b> |
| <b>6.1 Definition of the problem .....</b>            | <b>73</b> |
| 6.1.1 General description.....                        | 73        |
| 6.1.2 Nomenclature .....                              | 73        |
| 6.1.3 Governing equations.....                        | 73        |
| <b>6.2 Numerical methods.....</b>                     | <b>77</b> |
| 6.2.1 Time-integration .....                          | 77        |
| 6.2.2 Spatial approximation .....                     | 77        |
| <b>6.3 Results and discussion .....</b>               | <b>79</b> |
| <b>7 Specific case. External Flow simulation.....</b> | <b>82</b> |
| <b>7.1 Definition of the problem .....</b>            | <b>82</b> |
| 7.1.1 General description.....                        | 82        |
| 7.1.2 Nomenclature .....                              | 82        |
| 7.1.3 Governing equations.....                        | 83        |
| <b>7.2 Numerical methods.....</b>                     | <b>84</b> |
| 7.2.1 Time-integration .....                          | 84        |

|   |            |
|---|------------|
| 7.2.2 Spatial integration.....                                    | 84         |
| <b>7.3 Results and discussion .....</b>                           | <b>86</b>  |
| 7.3.1 Confined flow over a square cylinder .....                  | 87         |
| 7.3.2 Confined flow over an airfoil.....                          | 100        |
| <b>8 Conclusions and recommendations for future research.....</b> | <b>103</b> |
| <b>9 Study's Budget .....</b>                                     | <b>105</b> |
| <b>10 Environmental impact .....</b>                              | <b>106</b> |
| <b>11 References.....</b>   | <b>108</b> |

## List of figures

|  |    |
|--|----|
| Figure 1: relation cfd/wind tunnel.....  | 14 |
| Figure 2: general arrangement of a control volume and its main associated parameters. ....                       | 16 |
| Figure 3: general scheme of the problem. ....  | 24 |
| Figure 4: sketch of a side in contact with two different materials. ....   | 28 |
| Figure 5: comparison with benchmark results (left) .....   | 28 |
| Figure 6: temperature contour plots at different simulation times. ....  | 30 |
| Figure 7: temperature temporal evolution of two points. ....   | 30 |
| Figure 8: general scheme of the problem .....  | 31 |
| Figure 9: variable's profile at the cavity inlet. ....   | 31 |
| Figure 10: streamlines of the prescribed velocity field. ....  | 33 |
| Figure 11: $\phi$ contour plots for different $\rho/\Gamma$ ratios. Results obtained with a cds scheme. ....     | 37 |
| Figure 12: comparison of the outlet the inlet profile. Results obtained with a cds scheme. ....                  | 37 |
| Figure 13: $\phi$ contour plots for different $\rho/\Gamma$ ratios. Results obtained with an upwind scheme. .... | 39 |
| Figure 14: comparison of the outlet and the inlet profile. Results obtained with an upwind scheme. ....          | 39 |
| Figure 15: error vs mesh size corresponding to second order approximations. ....                                 | 40 |
| Figure 16: sketch of the lid driven cavity problem .....   | 41 |
| Figure 17: mesh distribution for a mesh concentration factor of $\gamma = 1.5$ .....                             | 48 |
| Figure 18: collocated mesh (left), x-direction (middle) and y-direction (right) staggered meshes .....           | 49 |
| Figure 19: velocity horizontal component $u$ contour plots for different $Re$ .....                              | 50 |
| Figure 20: velocity vertical component $v$ contour plots for different $Re$ . ....                               | 51 |
| Figure 21: stream function contour plots for different $Re$ .....  | 52 |
| Figure 22: comparison of horizontal component $u$ with benchmark solution (blue dots) . ....                     | 54 |
| Figure 23: comparison of vertical component $v$ with benchmark solution (blue dots) .....                        | 55 |
| Figure 24: error plot for $A_u = A_v = 1.0, n_u = 1.0, m_u = 2.0, n_v = 3.0$ and $m_v = 4.0$ .....               | 57 |
| Figure 25: error plot for $A_u = A_v = 1.0, n_u = 0.25, m_u = 1.0, n_v = 1.0$ and $m_v = 0.5$ . ....             | 57 |
| Figure 26: sketch of the problem. ....   | 58 |
| Figure 27: temperature contour plots for different $Ra$ . ....   | 66 |
| Figure 28: horizontal velocity component $u$ contour plots for different $Ra$ . ....                             | 67 |
| Figure 29: vertical velocity component $v$ contour plots for different $Ra$ .....                                | 68 |
| Figure 30: stream function $\psi$ contour plots for different $Ra$ .....   | 69 |
| Figure 31: vorticity $\zeta$ contour plots for different $Ra$ .....  | 70 |
| Figure 32: possible interactions between modes.....  | 78 |
| Figure 33: energy spectrum for dns (at the top) and les (at the bottom). ....                                    | 79 |
| Figure 34: superimposed energy spectra .....   | 80 |
| Figure 35: burgers' equation steady solution for dns and les methods .....                                       | 81 |
| Figure 36: domain of the problem and prescribed inlet velocity (confined flow) .....                             | 82 |
| Figure 37: non-uniform mesh example .....  | 85 |
| Figure 38: detail of the mesh in the obstacle's vicinity .....   | 85 |
| Figure 39: horizontal velocity contour plots for different Reynolds numbers. ....                                | 88 |
| Figure 40: vertical velocity contour plots for different Reynolds numbers.....                                   | 88 |
| Figure 41: pressure coefficient $C_p$ contour plots for different Reynolds numbers. ....                         | 89 |
| Figure 42: streamlines for different Reynolds numbers.....   | 90 |
| Figure 43: $C_d$ vs $Re$ comparison .....  | 91 |
| Figure 44: $L_r$ comparison .....  | 92 |
| Figure 45: recirculation length measurement .....  | 92 |
| Figure 46: kinetic energy contour plots for different Reynolds numbers. ....                                     | 93 |
| Figure 47: pressure coefficient contour plots for different Reynolds numbers. ....                               | 94 |

|  |     |
|--|-----|
| Figure 48: streamlines for different Reynolds numbers.....                                     | 95  |
| Figure 49: lift coefficient time evolution and amplitude spectrum for different Reynolds. .... | 97  |
| Figure 50: $St(Re)$ curve comparison.....  | 97  |
| Figure 51: drag coefficient time evolution for different Reynolds. ....                        | 98  |
| Figure 52: $C_d(Re)$ curve comparison. ....  | 99  |
| Figure 53: mesh detail at the airfoils's vicinity. ....  | 100 |
| Figure 54: contour plot of different computed variables at a certain time. ....                | 102 |
| Figure 55: world's largest wind tunnel at NASA Ames Research Center, in California.....        | 106 |

## List of tables

|  |     |
|--|-----|
| Table 1: parameters of the convection-diffusion equation.....                              | 16  |
| Table 2: properties of each material. ....   | 24  |
| Table 3: coordinates of the problem. ....  | 24  |
| Table 4: conduction case simulation parameters.....  | 28  |
| Table 5: simulation parameters of each case. ....  | 36  |
| Table 6: lid driven cavity problem simulation parameters. ....                             | 49  |
| Table 7: differentially heated cavity problem simulation parameters. ....                  | 65  |
| Table 8: comparison between the obtained results and the benchmark solution. ....          | 72  |
| Table 9: relative error (%) of the obtained results with respect to benchmark values. .... | 72  |
| Table 10: burgers' equation simulation parameters. ....                                    | 79  |
| Table 11: example mesh parameters. ....  | 85  |
| Table 12: geometrical parameters of the problem. ....                                      | 87  |
| Table 13: obtained $C_d$ and $C_l$ results.....  | 91  |
| Table 14: recirculation area length obtained . ....  | 91  |
| Table 15: computed strouhal numbers. ....  | 97  |
| Table 16: computed mean drag coefficients. ....  | 99  |
| Table 17: geometrical parameters of the airfoil case.....                                  | 100 |
| Table 18: airfoil's case mesh parameters. ....   | 101 |
| Table 19: computed lift and drag coefficients. ....  | 102 |
| Table 20: budget of the study. ....  | 105 |

## 1 Introduction

### 1.1 Aim of the study

This study is intended to provide knowledge and expertise in computational and numerical simulation by means of the development, validation and verification of own codes, which will be related to the resolution of the conservation equations of mass, momentum and energy applied to several benchmark problems and to a specific case on a field of interest.

### 1.2 Background and justification

Navier-Stokes equations are a set of coupled differential equations which describe the motion of fluids. These equations are called conservation equations of mass, momentum and energy too. Its general form may be seen below:

$$\frac{\partial \rho}{\partial t} + \nabla \cdot (\rho \mathbf{v}) = 0 \quad (1.1a)$$

$$\rho \left( \frac{\partial \mathbf{v}}{\partial t} + (\mathbf{v} \cdot \nabla) \mathbf{v} \right) = -\nabla p + \nabla \bar{\tau} + \rho \mathbf{g} \quad (1.2a)$$

$$\rho \left( \frac{\partial e}{\partial t} + \mathbf{v} \cdot \nabla e \right) = \nabla(\lambda \nabla T) - \mathbf{v} \cdot \nabla p + \mathbf{v} \cdot \nabla \bar{\tau} + \rho \mathbf{v} \cdot \mathbf{g} + \Phi \quad (1.3a)$$

Equation 1.1a is the equation of mass conservation, 1.2a of linear momentum conservation and 1.3a of energy conservation.

Despite this set of equations were derived, independently, in the early 1800's by G.G. Stokes and Navier, it has not yet been mathematically proven the existence of smooth solutions, or that if they do exist, they have bounded energy per unit mass [1]. This is called the Navier-Stokes existence and smoothness problem, and belongs to the so-called Millennium Prize Problems<sup>1</sup>.

Even though these equations are widely used in engineering, the theoretical understanding of the solutions to these equations is incomplete, and in particular, turbulence is considered to be one of the greatest unsolved problems in physics.

The main reason of such set of equations being so complex is the coupling and the presence of the so-called convective terms, which are a source of non-linearity. It has been precisely this impossibility to find analytical general solutions that has

---

<sup>1</sup> Millennium Prize Problems are seven problems in mathematics that were started by the Clay Mathematics Institute that if solved, result in a US \$ 1,000,000 prize.

forced engineers to find solutions by two different ways: by either simplifying the equations as much as possible or obtaining approximate solutions by means of different techniques such as finite difference, finite volume, finite element or spectral methods. These latter techniques define what is known as Computational Fluid Dynamics (CFD). Nowadays, with high speed computers it is relatively easy to obtain approximated solutions within a reasonable amount of time.

Thus, it appears that the knowledge of computational techniques it is fundamental, as they are essential in the resolution and simulation of a wide variety of problems related to very different fields of engineering ranging from the aforementioned fluid dynamics to electromagnetism or structural analysis.

Nevertheless, the importance attached to computational methods in ordinary aerospace engineering syllabus does not seem to fulfil completely this requirement of a solid knowledge of these techniques. Therefore, as stated in the aim, this study will provide an unrivalled opportunity to gain expertise and achieving a good command of this field of engineering.

### 1.3 Scope

- Brief review of the state-of-the-art and evolution of computational methods and techniques regarding fluid dynamics.
- Study of the different numerical techniques and methods used in Computational Fluid Dynamics and Heat Transfer (CFD&HT).
- Study of the effects of these diverse numerical techniques in the results and the convergence of the codes.
- Brief review on the turbulence phenomenon and its numerical treatment.
- Development of codes for the numerical resolution of benchmark problems, such as the Smith-Sutton problem or the Lid Driven Cavity.
- Analysis of the different numerical techniques applied to the aforementioned model problems.
- Validation and verification of the created codes.
- Proposal of a case of study in a specific field of interest. The field targeted in this study is the simulation of external flow, particularly flows over airfoil-shaped bodies.
- Development, validation and verification of the code created to simulate the proposed case.
- Conclusions and future lines of research.

## 1.4 Specifications

- Codes must be written in C or FORTRAN, which can be compiled in Linux environment.
- Use of linear algebra libraries or PDE solvers is not permitted. All the software has to be developed by oneself.
- Codes must be suitable to be executed by a normal computer.
- Codes should be in a single file and compile with no errors.
- Codes must run without any input parameter.

## 1.5 CFD. Finite volume method. Brief review and state of the art

Computational Fluid Dynamics (CFD) is branch of fluid mechanics that is intended to solve and analyze problems involving fluid flows by means of numerical methods and algorithms.

### 1.5.1 Brief History

In 1960 the underlying principles of fluid dynamics and the formulation of the governing equations were well established. The appearance of powerful enough computers that made numerical solutions of these equations possible gave birth to a new branch of fluid dynamics: CFD.

The emergence of CFD since its appearance in the 60's to these days has strongly depended on a combination of advances in computer power and algorithms. Since the birth of the first supercomputers such as CDC6600, computer performance has increased continuously: an affordable current laptop may have a performance of the order of Gigaflops<sup>2</sup> (1,000 times the performance of CDC6600), and clusters of supercomputers reach values of 100 Teraflops [2].

Despite the evolution of computational power, Direct Numerical Simulation (DNS) of the Navier-Stokes equations is very difficult and expensive in terms of computational costs. The computational cost (i.e. the number of total operations needed to reach a solution), assuming a perfect algorithm scaling, grows with the Reynolds number [3]:

$$Cost_{comp} \sim Re^{\frac{11}{4}} \quad (1.4)$$

However, in actual codes the computational cost scales typically with  $Re^3$ . Thus, to solve the flow over an A380 with  $Re \approx 10^8$ , the computational cost would be of the order of  $10^{24}$ , which means that with a Petaflop computer it would take about 30 years.

The impact of CFD on the most important aircraft manufacturers such as Boeing and Airbus is the substantially reduction in wind tunnel testing, as with the current and future improvements in algorithms and hardware is becoming a cheaper alternative concerning flow simulation.

---

<sup>2</sup> In computing, FLOPS is an acronym that stands for Floating-point Operations Per Second and it is a measure of computer performance.[24]

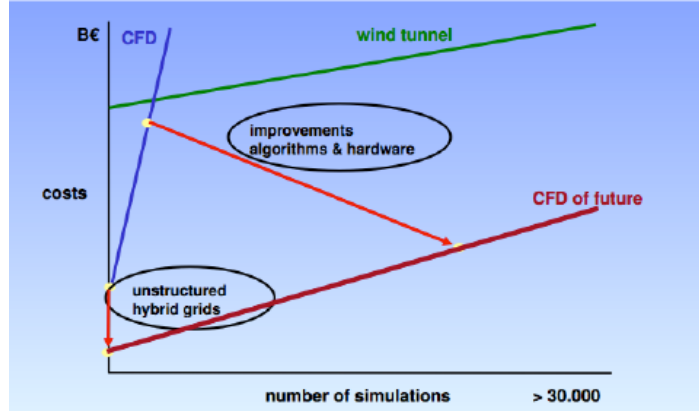


Figure 1: Relation CFD/wind tunnel. Extracted from [2].

Nowadays, worldwide commercial and government codes are based on algorithms that were developed in the '80s and '90s. These codes are able to solve complex geometries but have problems when increasing accuracy. Turbulence and unsteady simulations are very expensive if solved without modelling (i.e. solved by DNS). It is said that CFD has been on a plateau for the past 15 years. The representations of the current state of the art are the F1 cars and complete aircrafts.[2]

### 1.5.2 Finite Volume Method

There exists plenty of different methods in CFD. Some of the most used are:

- Finite Element Method (FEM)
- Finite Difference Method (FDM)
- Finite Volume Method (FVM)
- Spectral Methods

The methodology of CFD, regardless of the method used, consists basically of three parts: pre-processing, simulation and post-processing. In the pre-processing step the geometry of the problem is defined, the volume occupied by the fluid is divided into a finite number of control volumes (the mesh), the problem is modelled by its governing equations which are properly manipulated, usually aiming the obtaining of a set of linear equations, and finally the boundary and initial conditions are defined. Then the simulation is started and the equations are solved iteratively. Finally the post-processing step permits the visualization of the resulting solution.

This paper will focus on the resolution of the Navier-Stokes equations by means of the Finite Volume Method. This method is used in most general purpose CFD codes. One important feature of the FVM schemes is their conservation

properties, for the conservation principles are applied over each small control volume and global conservation is thus ensured.

Taking into account the hypothesis in which this paper will be based:

- Bidimensional model
- Incompressible flow
- Newtonian fluid
- Boussinesq hypothesis
- Negligible viscous dissipation
- Negligible compression or expansion work
- Non-participating medium in radiation
- Mono-component and mono-phase fluid

Equations 1.1a, 1.2a and 1.3a are rewritten as follows

$$\frac{\partial u}{\partial x} + \frac{\partial v}{\partial y} = 0 \quad (1.1b)$$

$$\rho \frac{\partial u}{\partial t} + \rho(\mathbf{v} \cdot \nabla)u = -\frac{\partial p_d}{\partial x} + \mu \nabla^2 u \quad (1.2b-x)$$

$$\rho \frac{\partial v}{\partial t} + \rho(\mathbf{v} \cdot \nabla)v = -\frac{\partial p_d}{\partial y} + \mu \nabla^2 v + \rho g \beta_0 (T - T_0) \quad (1.2b-y)$$

$$\rho \frac{\partial T}{\partial t} + \rho(\mathbf{v} \cdot \nabla)T = \frac{\lambda}{c_p} \nabla^2 T + \frac{\Phi}{c_p} \quad (1.3b)$$

Where  $\beta$  is the coefficient of volumetric thermal expansion,  $c_p$  is the specific heat,  $\lambda$  is the conductivity,  $\Phi$  is the heat source,  $g$  is the acceleration due to gravity,  $\mu$  is the viscosity,  $p_d$  is the dynamic pressure,  $\rho$  is the density,  $t$  is the time,  $T$  is the temperature,  $u$  and  $v$  are the velocity components,  $\mathbf{v}$  is the velocity field vector and  $x$  and  $y$  are the spatial coordinates.

These equations may be summarized in a general scalar convection-diffusion equation:

$$\rho \frac{\partial \phi}{\partial t} + \rho(\mathbf{v} \cdot \nabla)\phi = \Gamma \nabla^2 \phi + S \quad (1.5)$$

Then, by comparison of each of equations 1.1b, 1.2b-x, 1.2b-y and 1.3b with 1.5, the parameters of the convection-diffusion corresponding to each conservation equations are gathered in table 1.

| Equation                            | $\phi$ | $\Gamma$              | $S$   |
|-------------------------------------|--------|-----------------------|---|
| Mass conservation<br>(1.1b)         | 1      | 0                     | 0   |
| Momentum in x direction<br>(1.2b-x) | $u$    | $\mu$                 | $-\frac{\partial p_d}{\partial x}$                            |
| Momentum in y direction<br>(1.2b-y) | $v$    | $\mu$                 | $-\frac{\partial p_d}{\partial y} + \rho g \beta_0 (T - T_0)$ |
| Energy<br>(1.3b)                    | $T$    | $\frac{\lambda}{c_p}$ | $\frac{\Phi}{c_p}$  |

Table 1: Parameters of the convection-diffusion equation.

The discretization process in the FVM is done by integrating each equation over each of the control volumes (see figure 2) in which the whole domain has been divided.

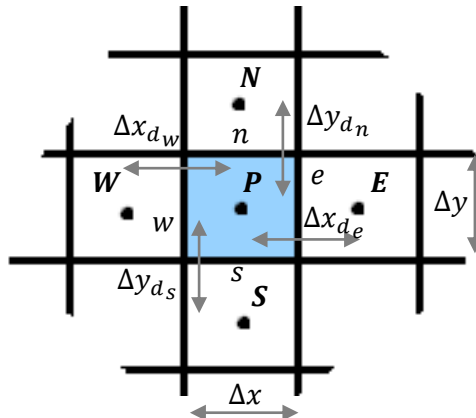


Figure 2: General arrangement of a control volume and its main associated parameters.

As it has been said in previous lines, every conservation equation that will be used can be derived from the general convection-diffusion equation, so the basic steps of the FVM discretization will be shown with this latter expression as an example. Integrating equation 1.5 over a general rectangular control volume:

$$\int_{\Omega} \rho \frac{\partial \phi}{\partial t} d\Omega + \int_{\Omega} \rho (\nabla \cdot \mathbf{v}) \phi d\Omega = \int_{\Omega} \Gamma \nabla^2 \phi d\Omega + \int_{\Omega} S d\Omega$$

One shall develop each of the terms separately for the sake of clarity and comprehension.

*Transient term*

$$\int_{\Omega} \rho \frac{\partial \phi}{\partial t} d\Omega \approx \rho \frac{\partial \phi_P}{\partial t} \Delta x \Delta y \quad (1.6)$$

Where  $\phi_P$  is the value of  $\phi$  at node  $P$  and it is regarded as the mean value of  $\phi$  over the CV. This is a second order approximation, and it can be proved by considering the Taylor series to the first order of the variable  $\phi$  about node  $P$ :

$$\phi(x, y) = \phi_P + \left. \frac{\partial \phi}{\partial x} \right|_P (x - x_P) + \left. \frac{\partial \phi}{\partial y} \right|_P (y - y_P) + \dots \quad (1.7)$$

Integrating such expression over a CV:

$$\begin{aligned} \int_{\Omega} \phi d\Omega &= \int_{\Omega} \left( \phi_P + \left. \frac{\partial \phi}{\partial x} \right|_P (x - x_P) + \left. \frac{\partial \phi}{\partial y} \right|_P (y - y_P) + \dots \right) d\Omega = \\ &= \phi_P \int_{\Omega} d\Omega + \left. \frac{\partial \phi}{\partial x} \right|_P \int_{\Omega} (x - x_P) d\Omega + \left. \frac{\partial \phi}{\partial y} \right|_P \int_{\Omega} (y - y_P) d\Omega + \dots = \\ &= \phi_P \Delta x \Delta y + \left. \frac{\partial \phi}{\partial x} \right|_P \int_{\Omega} (x - x_P) d\Omega + \left. \frac{\partial \phi}{\partial y} \right|_P \int_{\Omega} (y - y_P) d\Omega + \dots = \\ &= \phi_P \Delta x \Delta y + \left. \frac{\partial \phi}{\partial x} \right|_P \left( \frac{\Delta x^2}{2} + (x_w - x_P) \Delta x \right) \Delta y + \left. \frac{\partial \phi}{\partial y} \right|_P \left( \frac{\Delta y^2}{2} + (y_s - y_P) \Delta y \right) \Delta x \\ &\quad + \dots \end{aligned}$$

Which constitutes a second order approximation with respect to direction  $x$  and  $y$  separately, since the differences  $|x_w - x_P| < \Delta x$  and  $|y_s - y_P| < \Delta y$  and therefore their product with  $\Delta x$  and  $\Delta y$  are, respectively, of the order of  $\Delta x^2$  and  $\Delta y^2$ . One may obtain a third order accuracy approximation by imposing  $x_P$  and  $y_P$  to be the CV's centroid coordinates. If so, by definition these two integrals are identically zero:

$$\int_{\Omega} (x - x_P) d\Omega = 0 \quad (1.8)$$

$$\int_{\Omega} (y - y_P) d\Omega = 0 \quad (1.9)$$

Then:

$$\int_{\Omega} \rho \frac{\partial \phi}{\partial t} d\Omega \approx \rho \frac{\partial \phi_P}{\partial t} \Delta x \Delta y + \sigma(\Delta x^3, \Delta y^3) \quad (1.10)$$

*Convective term*

$$\int_{\Omega} \rho(\mathbf{v} \cdot \nabla) \phi \, d\Omega = \int_{\Omega} \rho \nabla \cdot (\mathbf{v} \phi) \, d\Omega = \int_{\Gamma} \rho(\mathbf{v} \phi) \cdot \hat{n} \, dS$$

Where the divergence theorem and the fact that  $\nabla \cdot \mathbf{v} = 0$  have been applied. Integrating over each of the CV faces:

$$\int_{\Gamma} \rho(\mathbf{v} \phi) \cdot \hat{n} \, dS \approx \rho(u_e \phi_e - u_w \phi_w) \Delta y + \rho(v_n \phi_n - v_s \phi_s) \Delta x$$

Where the subscripts indicate that the variables have been evaluated at each of the cell's faces. It may be shown that this is a second order approximation too and may be converted into a third order accuracy approximation if the product  $u\phi$  is evaluated at the centre of the cell faces. Let  $f(x, y)$  be the function to integrate over a certain cell face, for instance east face. Then  $f(x, y)$  is a function of  $y$  uniquely. Its Taylor series to the second order is:

$$f(y) = f(y_P) + \frac{\partial f}{\partial y} \Big|_P (y - y_P) + \frac{\partial^2 f}{\partial y^2} \Big|_P (y - y_P)^2 + \dots \quad (1.11)$$

Its integral over the east face is:

$$\begin{aligned} \int_{\Gamma_e} f \, dy &= \int_{\Gamma_e} f(y_P) \, dy + \int_{\Gamma_e} \frac{\partial f}{\partial y} \Big|_P (y - y_P) \, dy + \int_{\Gamma_e} \frac{\partial^2 f}{\partial y^2} \Big|_P (y - y_P)^2 \, dy + \dots = \\ &= f_e \int_{\Gamma_e} dy + \frac{\partial f}{\partial y} \Big|_P \int_{\Gamma_e} (y - y_P) \, dy + \frac{\partial^2 f}{\partial y^2} \Big|_P \int_{\Gamma_e} (y - y_P)^2 \, dy + \dots = \\ &= f_e \Delta y + \frac{\partial^2 f}{\partial y^2} \Big|_P \int_{\Gamma_e} (y - y_P)^2 \, dy + \dots = f_e \Delta y + \frac{\partial^2 f}{\partial y^2} \Big|_P \frac{\Delta y^3}{12} + \dots \end{aligned}$$

Where it has been considered that  $y_P$  was situated at the centre of the east face. So, the convective term is:

$$\begin{aligned} \int_{\Omega} \rho(\mathbf{v} \cdot \nabla) \phi \, d\Omega &\approx \rho[(u_e \phi_e - u_w \phi_w) \Delta y + (v_n \phi_n - v_s \phi_s) \Delta x] + \\ &\quad + \sigma(\Delta x^3, \Delta y^3) \end{aligned} \quad (1.12)$$

*Diffusive term*

$$\int_{\Omega} \Gamma \nabla^2 \phi \, d\Omega = \int_{\Gamma} \Gamma \nabla \phi \cdot \hat{n} \, dS$$

Where the divergence theorem has been used. As with the development of the convective term, the diffusive term may be discretized using a third order

accuracy approximation too, provided that the node is situated at the CV's centroid. Then:

$$\int_{\Omega} \Gamma \nabla^2 \phi \, d\Omega = \Gamma \left[ \left( \frac{\partial \phi}{\partial x} \Big|_e - \frac{\partial \phi}{\partial x} \Big|_w \right) \Delta y + \left( \frac{\partial \phi}{\partial y} \Big|_n - \frac{\partial \phi}{\partial y} \Big|_s \right) \Delta x \right] + \sigma(\Delta x^3, \Delta y^3) \quad (1.13)$$

#### *Source term*

The source term is approximated as follows:

$$\int_{\Omega} S \, d\Omega \approx S_p \Delta x \Delta y + \sigma(\Delta x^3, \Delta y^3) \quad (1.14)$$

Finally, the discretized convection-diffusion equation reads:

$$\begin{aligned} \rho \frac{\partial \phi_p}{\partial t} \Delta x \Delta y + \rho [(u_e \phi_e - u_w \phi_w) \Delta y + (v_n \phi_n - v_s \phi_s) \Delta x] &= \\ &= \Gamma \left[ \left( \frac{\partial \phi}{\partial x} \Big|_e - \frac{\partial \phi}{\partial x} \Big|_w \right) \Delta y + \left( \frac{\partial \phi}{\partial y} \Big|_n - \frac{\partial \phi}{\partial y} \Big|_s \right) \Delta x \right] + S_p \Delta x \Delta y \end{aligned} \quad (1.15)$$

The next step would be the temporal discretization. However, this process is not inherent to FVM, and may be different (explicit, implicit) depending on the case. Therefore, time discretization will be detailed in each of the considered cases. Another pending aspect is how one approximates the variables that are evaluated at the cell's wall, present in convective terms, or the first derivatives that appear in the diffusive terms. Then, one should find a way of constructing approximations of a desired order of accuracy.

#### 1.5.3 Approximation process

As seen in previous lines, Taylor series expansions play a crucial role concerning the construction of approximations, as they permit to control the accuracy order. Two examples of this process will be exposed: the evaluation of the variables at the cell's face and the first derivative at the cell's face, which are the two terms that appear in the integrated convection-diffusion equation and it is necessary to know how to approximate them.

##### Variable evaluation at cell's face

Amongst the many schemes that are used to evaluate a variable at a cell's face, this paper uses only two: the upwind scheme and the Central Difference Scheme (CDS), being of first and second order of accuracy respectively. More information regarding other higher accuracy schemes for evaluating terms at a volume's face may be found in [4].

### *Upwind*

The upwind scheme is a first order accuracy approximation and it consists of assuming the variable at a face equal to the value at one of its closer neighbours depending on the direction of the flow. For instance, if one considers the east wall:

$$\begin{aligned}\phi_e &\approx \phi_P \text{ if } u_e \geq 0 \\ \phi_e &\approx \phi_E \text{ if } u_e < 0\end{aligned}\quad (1.16)$$

In order to show it is a first order scheme one may consider the Taylor expansion of  $\phi$  with respect to  $x$  coordinate about the nodes E and P:

$$\phi_e = \phi_P + \frac{\partial \phi}{\partial x} \Big|_P \left( \frac{\Delta x_{de}}{2} \right) + \frac{1}{2!} \frac{\partial^2 \phi}{\partial x^2} \Big|_P \left( \frac{\Delta x_{de}}{2} \right)^2 + \dots = \phi_P + o\left(\frac{\Delta x_{de}}{2}\right) \quad (1.17)$$

$$\phi_e = \phi_E - \frac{\partial \phi}{\partial x} \Big|_E \left( \frac{\Delta x_{de}}{2} \right) + \frac{1}{2!} \frac{\partial^2 \phi}{\partial x^2} \Big|_E \left( \frac{\Delta x_{de}}{2} \right)^2 + \dots = \phi_E + o\left(\frac{\Delta x_{de}}{2}\right) \quad (1.18)$$

Then, one clearly sees that by approaching the variable at the cell's wall as 1.16 indicates, the error is of first order.

### *Central Difference Scheme (CDS)*

Central Difference Scheme evaluates the variable's value at the wall as the arithmetic mean of the values of the variable at the closest neighbours' nodes. Again, the value of  $\phi$  at the east wall is:

$$\phi_e \approx \frac{\phi_P + \phi_E}{2} \quad (1.19)$$

The Taylor series around the east face are:

$$\phi_P = \phi_e - \frac{\partial \phi}{\partial x} \Big|_e \left( \frac{\Delta x_{de}}{2} \right) + \frac{1}{2!} \frac{\partial^2 \phi}{\partial x^2} \Big|_e \left( \frac{\Delta x_{de}}{2} \right)^2 + \dots \quad (1.20)$$

$$\phi_E = \phi_e + \frac{\partial \phi}{\partial x} \Big|_e \left( \frac{\Delta x_{de}}{2} \right) + \frac{1}{2!} \frac{\partial^2 \phi}{\partial x^2} \Big|_e \left( \frac{\Delta x_{de}}{2} \right)^2 + \dots \quad (1.21)$$

If one sums up equations 1.20 and 1.21 and divides by two:

$$\frac{\phi_P + \phi_E}{2} = \phi_e + \frac{1}{2!} \frac{\partial^2 \phi}{\partial x^2} \Big|_e \left( \frac{\Delta x_{de}}{2} \right)^2 + \dots = \phi_e + o\left(\left(\frac{\Delta x_{de}}{2}\right)^2\right) \quad (1.22)$$

In this case it is clear that appears a second order error.

#### First derivative at cell's face

One may want to find an approximation of the first derivative which depended linearly on the variable at the neighbours' nodes. Again, considering the east face:

$$\left. \frac{\partial \phi}{\partial x} \right|_e \approx a_P \phi_P + a_E \phi_E \quad (1.23a)$$

The Taylor expansions about the east face evaluated at nodes  $P$  and  $E$  are:

$$\phi_P = \phi_e - \left. \frac{\partial \phi}{\partial x} \right|_e \left( \frac{\Delta x_{de}}{2} \right) + \frac{1}{2!} \left. \frac{\partial^2 \phi}{\partial x^2} \right|_e \left( \frac{\Delta x_{de}}{2} \right)^2 - \frac{1}{3!} \left. \frac{\partial^3 \phi}{\partial x^3} \right|_e \left( \frac{\Delta x_{de}}{2} \right)^3 + \dots \quad (1.24)$$

$$\phi_E = \phi_e + \left. \frac{\partial \phi}{\partial x} \right|_e \left( \frac{\Delta x_{de}}{2} \right) + \frac{1}{2!} \left. \frac{\partial^2 \phi}{\partial x^2} \right|_e \left( \frac{\Delta x_{de}}{2} \right)^2 + \frac{1}{3!} \left. \frac{\partial^3 \phi}{\partial x^3} \right|_e \left( \frac{\Delta x_{de}}{2} \right)^3 + \dots \quad (1.25)$$

By substituting 1.24 and 1.25 into 1.23a one obtains:

$$\begin{aligned} \left. \frac{\partial \phi}{\partial x} \right|_e &= \phi_e (a_P + a_E) + \left. \frac{\partial \phi}{\partial x} \right|_e (a_E - a_P) \frac{\Delta x_{de}}{2} + \\ &+ \frac{1}{2!} \left. \frac{\partial^2 \phi}{\partial x^2} \right|_e (a_E + a_P) \left( \frac{\Delta x_{de}}{2} \right)^2 + \frac{1}{3!} \left. \frac{\partial^3 \phi}{\partial x^3} \right|_e (a_E - a_P) \left( \frac{\Delta x_{de}}{2} \right)^3 + \dots \end{aligned} \quad (1.26)$$

Imposing:

$$\begin{cases} a_P + a_E = 0 \\ (a_E - a_P) \frac{\Delta x_{de}}{2} = 1 \end{cases} \quad (1.27)$$

As it is not desired that the approximation depended on  $\phi_e$ . Solving the resulting system of equations one obtains:

$$\begin{cases} a_P = -\frac{1}{\Delta x_{de}} \\ a_E = \frac{1}{\Delta x_{de}} \end{cases} \quad (1.28)$$

Then 1.23a may be rewritten:

$$\left. \frac{\partial \phi}{\partial x} \right|_e = \frac{\phi_E - \phi_P}{\Delta x_{de}} + \sigma \left( \left( \frac{\Delta x_{de}}{2} \right)^2 \right) \quad (1.23b)$$

If one desires to construct approximations with a higher order of accuracy, more nodes are to be selected for the approximation.

Applying both the CDS scheme, a second order approximation for the first derivative and assuming steady state, equation 1.15 may be approximated as follows:

$$\begin{aligned} \rho \left[ \left( u_e \frac{\phi_E + \phi_P}{2} - u_w \frac{\phi_W + \phi_P}{2} \right) \Delta y + \left( v_n \frac{\phi_N + \phi_P}{2} - v_s \frac{\phi_S + \phi_P}{2} \right) \Delta x \right] = \\ = \Gamma \left[ \left( \frac{\phi_E - \phi_P}{\Delta x_{d_e}} - \frac{\phi_P - \phi_W}{\Delta x_{d_w}} \right) \Delta y + \left( \frac{\phi_N - \phi_P}{\Delta y_{d_n}} - \frac{\phi_P - \phi_S}{\Delta y_{d_s}} \right) \Delta x \right] + S_P \Delta x \Delta y \end{aligned} \quad (1.29)$$

Expression 1.29 shows how a linear equation has been obtained:

$$a_P \phi_P + a_N \phi_N + a_S \phi_S + a_E \phi_E + a_W \phi_W = b_P \quad (1.30)$$

As a matter of fact, this equation couples the considered node with its neighbours. It is precisely the values of  $\phi$  at these nodes what one seeks to obtain: they are the unknowns of the problem. Let  $N$  be the total number of control volumes in which the domain has been divided. Then, one expects to obtain a system of  $N$  equations (one equation like 1.30 for each CV) and  $N$  variables (each of the values of  $\phi$  at each of the nodes), which together with the boundary conditions would completely define the approximated problem.

$$\begin{pmatrix} a_{P_1} & a_{E_1} & \cdots & a_{N_1} & 0 & & \cdots & & 0 \\ 0 & & & & & & & & \\ \vdots & a_{S_{i-1}} & \cdots & a_{W_{i-1}} & a_{P_{i-1}} & a_{E_{i-1}} & \cdots & a_{N_{i-1}} & 0 & 0 \\ & 0 & a_{S_i} & \cdots & a_{W_i} & a_{P_i} & a_{E_i} & \cdots & a_{N_i} & 0 \\ & 0 & 0 & a_{S_{i+1}} & \cdots & a_{W_{i+1}} & a_{P_{i+1}} & a_{E_{i+1}} & \cdots & a_{N_{i+1}} \\ 0 & & & \cdots & & & & & 0 & \\ & & & & & & & & & \\ 0 & & & & & & & & & \end{pmatrix} \begin{pmatrix} \phi_1 \\ \vdots \\ \phi_{i-1} \\ \phi_i \\ \phi_{i+1} \\ \vdots \\ \phi_N \end{pmatrix} = \begin{pmatrix} b_1 \\ \vdots \\ b_{i-1} \\ b_i \\ b_{i+1} \\ \vdots \\ b_N \end{pmatrix} \quad (1.31)$$

This is the general form of the coefficient matrix involved in the problem. Its general layout depends on the numeration of the nodes. It is clear it is a sparse matrix with many empty coefficients. This system has to be solved in order to obtain the approximated solution. There exist plenty of different solvers which aim to solve linear systems like 1.31. The most used are:

- Jacobi Method [5]
- Gauss-Seidel Method [6]
- TDMA (limited to tri-diagonal matrixes)[7]
- Conjugate Gradient Method [8]

The use of combinations of different methods is also widely extended such as the Gauss-Seidel with TDMA or variants such as the Biconjugate Gradient Method [9]. The above listed solvers are aimed to solve systems of equations whose matrix is symmetric or diagonally dominant<sup>3</sup>, which is typically the case of every problem in this paper. If not, numerical instabilities may arise. A solver which performs well with non-symmetric matrix is the Biconjugate Gradient Method but it is rather unstable. It exists, though, an enhanced variant of this latter which is known as Biconjugate Gradient Stabilized Method [10].

---

<sup>3</sup> In mathematics, a matrix is said to be diagonally dominant if for every row the magnitude of the diagonal coefficient is larger than or equal to the sum of the magnitudes of all the other (non-diagonal) coefficients in that row. [25]

## 2 2D Transient Conduction Problem

### 2.1 Definition of the problem

#### 2.1.1 General description

This problem focuses on the resolution of a transient conduction case. It consists of a rod, long enough to neglect the effects of its extremes and thus enabling to solve it as a two-dimensional problem. The rod is composed by four different materials (figure 3).

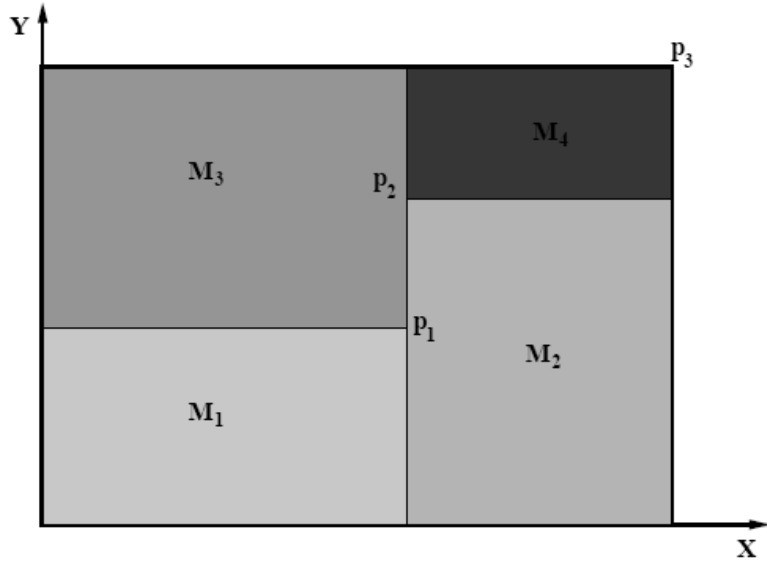


Figure 3: General scheme of the problem. Extracted from [11].

The properties of each material are shown in the table below.

|    | $\rho [kg/m^3]$ | $c_p [J/kgK]$ | $\lambda [W/mK]$ |
|----|-----------------|---------------|------------------|
| M1 | 1500.00         | 750.00        | 170.00           |
| M2 | 1600.00         | 770.00        | 140.00           |
| M3 | 1900.00         | 810.00        | 200.00           |
| M4 | 2500.00         | 930.00        | 140.00           |

Table 2: Properties of each material. Extracted from [11].

The coordinates of the most relevant points of the geometry are gathered in the next table:

|    | $x[m]$ | $y[m]$ |
|----|--------|--------|
| p1 | 0.50   | 0.40   |
| p2 | 0.50   | 0.70   |
| p3 | 1.10   | 0.80   |

Table 3: Coordinates of the problem. Extracted from [11].

The boundary conditions are different for each side of the rod. The bottom remains at a constant temperature of 23.00 °C. The top side receives a uniform heat flow of 60.00 W/m. The left side is in contact with a fluid at 33.00 °C and a heat transfer coefficient of 9.00 W/m<sup>2</sup>K. Finally, the right side of the rod is at a uniform temperature which evolves with time following the expression  $T_{right} = 8.00 + 0.005t$  °C (where  $t$  is the time in seconds). Attending to the initial conditions, the initial temperature field is 8.00 °C.

### 2.1.2 Nomenclature

| Problem data  | Numerical data  |
|---|---|
| $\rho$ : density of the material                                      | $N$ : number of control volumes   |
| $c_p$ : specific heat capacity  | $N_x$ : number of CV in x-direction   |
| $\lambda$ : thermal conductivity                                      | $N_y$ : number of CV in y-direction   |
| $\alpha$ : convection coefficient                                     | $\Delta t$ : time step  |
| $q_{top}$ : heat flux at rod's top                                    | $\Delta x$ : mesh horizontal size   |
| $T_{bottom}$ : temperature of rod's bottom                            | $\Delta y$ : mesh vertical size   |
| $T_{right}$ : temperature of rod's right side                         | $\gamma$ : mesh concentration factor  |
| $T_g$ : bulk temperature of the fluid in contact with rod's left side | $\Delta x_d$ : horizontal nodal distance  |
| $p_1, p_2, p_3$ : key points coordinates                              | $\Delta y_d$ : vertical nodal distance  |
| <br>  | <br>  |
| Problem variables   | Subscripts  |
| $T$ : temperature   | $\phi_n, \phi_s, \phi_e, \phi_w$ refer to the wall of the volume at which variables are evaluated |
| $x$ : horizontal coordinate   | $\phi_N, \phi_S, \phi_E, \phi_W, \phi_P$ refer to the node at which variables are evaluated       |
| $y$ : vertical coordinate   |   |
| $t$ : time  |   |
| <br>  | <br>  |
|   | Superscripts  |
|   | $\phi^{n+1}$ : current instant  |
|   | $\phi^n$ : previous instant   |

### 2.1.3 Governing equations

This is a case of pure conduction (i.e. convection phenomenon does not occur, it is a solid) and constant physical properties. Therefore, the energy equation is the only equation which will be used in order to obtain the temperature field. It reads:

$$\frac{\partial T}{\partial t} = \frac{\lambda}{\rho c_p} \nabla^2 T \quad (2.1)$$

## 2.2 Numerical methods

### 2.2.1 Time-integration

For this problem a fully implicit method will be used. Integrating expression 2.1 with respect to time between a generic instant  $t^n$  and the immediate following instant  $t^{n+1} = t^n + \Delta t$ :

$$\int_{t^n}^{t^{n+1}} \frac{\partial T}{\partial t} dt = T^{n+1} - T^n = \int_{t^n}^{t^{n+1}} \frac{\lambda}{\rho c_p} \nabla^2 T dt \approx \frac{\lambda}{\rho c_p} \nabla^2 T^{n+1} \Delta t$$

Then, the resulting time integrated equation reads:

$$\frac{T^{n+1} - T^n}{\Delta t} = \frac{\lambda}{\rho c_p} \nabla^2 T^{n+1} \quad (2.2)$$

Where  $\Delta t$  is the time step of the numerical time integration.

### 2.2.2 Spatial integration

In order to obtain the temperature field for each time step, the equation has to be integrated over the whole domain. Integrating equation 2.2 over a generic control volume, one would obtain a linear equation. The integration is done term by term in the following lines.

*Transient term*

$$\int_{\Omega} \frac{T^{n+1} - T^n}{\Delta t} d\Omega \approx \frac{T_P^{n+1} - T_P^n}{\Delta t} \Delta x \Delta y \quad (2.3)$$

*Diffusive term*

$$\begin{aligned} \int_{\Omega} \nabla^2 T^{n+1} d\Omega &= \int_{\Omega} \nabla \cdot (\nabla T^{n+1}) d\Omega = \int_{\partial\Omega} \nabla T^{n+1} \cdot \hat{\mathbf{n}} dS = \\ &\approx \left( \frac{\partial T^{n+1}}{\partial x} \Big|_e - \frac{\partial T^{n+1}}{\partial x} \Big|_w \right) \Delta y + \left( \frac{\partial T^{n+1}}{\partial y} \Big|_n - \frac{\partial T^{n+1}}{\partial y} \Big|_s \right) \Delta x \approx \\ &\approx \left( \frac{T_E^{n+1} - T_P^{n+1}}{\Delta x_{d_e}} - \frac{T_P^{n+1} - T_W^{n+1}}{\Delta x_{d_w}} \right) \Delta y \\ &\quad + \left( \frac{T_N^{n+1} - T_P^{n+1}}{\Delta y_{d_n}} - \frac{T_P^{n+1} - T_S^{n+1}}{\Delta y_{d_s}} \right) \Delta x \end{aligned} \quad (2.4)$$

Where a structured uniform Cartesian mesh and a second order approximation scheme has been used. One obtains, then, an equation of the form:

$$a_P T_P^{n+1} + a_N T_N^{n+1} + a_S T_S^{n+1} + a_E T_E^{n+1} + a_W T_W^{n+1} = b_P \quad (2.5)$$

For a generic control volume, each of the coefficients are detailed in the following lines:

$$a_P = \frac{\Delta x \Delta y}{\Delta t} + \frac{1}{\rho c_p} \left( \frac{\lambda_e \Delta y}{\Delta x_{d_e}} + \frac{\lambda_n \Delta x}{\Delta y_{d_n}} + \frac{\lambda_w \Delta y}{\Delta x_{d_w}} + \frac{\lambda_s \Delta x}{\Delta y_{d_s}} \right) \quad (2.6)$$

$$a_N = - \frac{\lambda_n}{\rho c_p} \frac{\Delta x}{\Delta y_{d_n}} \quad (2.7)$$

$$a_S = - \frac{\lambda_s}{\rho c_p} \frac{\Delta x}{\Delta y_{d_s}} \quad (2.8)$$

$$a_E = - \frac{\lambda_e}{\rho c_p} \frac{\Delta y}{\Delta x_{d_e}} \quad (2.9)$$

$$a_W = - \frac{\lambda_w}{\rho c_p} \frac{\Delta y}{\Delta x_{d_w}} \quad (2.10)$$

$$b_P = T_P^n \frac{\Delta x \Delta y}{\Delta t} \quad (2.11)$$

The volumes in contact with the walls of the rod must change slightly some coefficients, depending on the side of the volume in contact with the boundary and on the boundary condition.

$$a'_P = a_P + a_N ; \quad a'_N = 0 ; \quad b'_P = b_P - a_N \frac{q_{top} \Delta y_{d_n}}{\lambda_n} \quad (north) \quad (2.12)$$

$$a'_S = 0 ; \quad b'_P = b_P - a_S T_{bottom} \quad (south) \quad (2.13)$$

$$a'_E = 0 ; \quad b'_P = b_P - a_E T_{right} \quad (east) \quad (2.14)$$

$$\begin{aligned} a'_P &= a_P + \frac{a_W \lambda_w}{\alpha \Delta x_{d_w} + \lambda_w} ; \quad a'_W = 0 ; \\ b'_P &= b_P - \frac{a_W \alpha \Delta x T_g}{\alpha \Delta x_{d_w} + \lambda_w} \end{aligned} \quad (west) \quad (2.15)$$

In volumes where an edge is in contact with different materials, as for example those which have points p1 or p2 as vertexes, the development of the diffusive term is not accurate, as  $\lambda$  was regarded as a constant (i.e. with the same value at every side of the volume). For these special volumes, the evaluation of this physical property at the sides shared by two different materials may be done by means of an harmonic mean value. Being the two materials in contact A, and B, and its respective thermal conductivities being  $\lambda_A$  and  $\lambda_B$ :

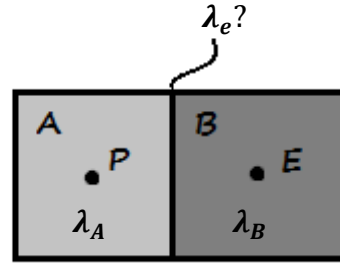


Figure 4: Sketch of a side in contact with two different materials.

$$\lambda_e = \frac{\frac{\Delta x_P + \Delta x_E}{\Delta x_P} \cdot \frac{\Delta x_E}{\Delta x_E}}{\frac{1}{\lambda_A} + \frac{1}{\lambda_B}} \quad (2.16)$$

### 2.3 Results and discussion

The numerical data used in the simulation are gathered in table 4.

| $N_x$ | $\gamma_x$       | $N_y$ | $\gamma_y$       | $N$  | $\Delta t$ [s] |
|-------|------------------|-------|------------------|------|----------------|
| 110   | 0.0<br>(uniform) | 80    | 0.0<br>(uniform) | 8.8K | 1              |

Table 4: Conduction case simulation parameters.

In [11] the temperature field contour plot at instant  $t = 5,000$  s is given, so in the next figure both results are compared.

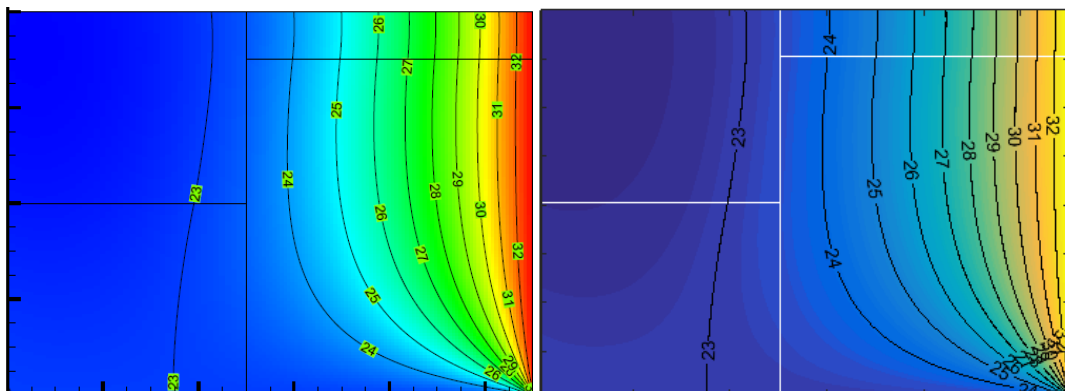
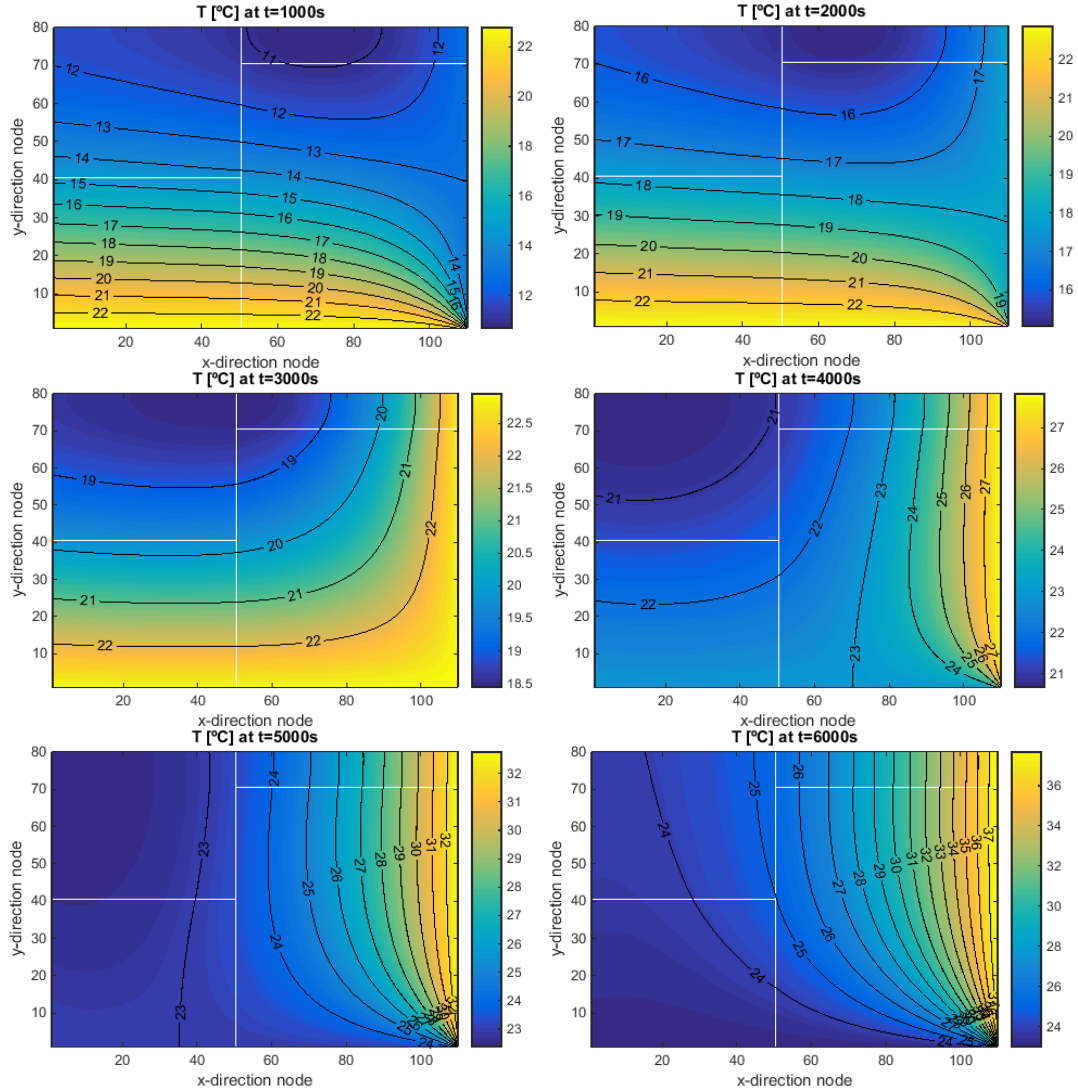


Figure 5: Comparison with benchmark results (left). Extracted from [11]

It is shown how both solutions are almost identical. However, it seems to be a faint variation concerning the isotherms of  $31^{\circ}\text{C}$  and  $32^{\circ}\text{C}$ , which appear to be closer to the wall in the right plot. This could be improved by implementing a non-uniform mesh, which would provide more resolution and accuracy at the wall's vicinity. Another possibility would be that the benchmark solution plot included the values at the boundary, which would enlarge the plot therefore giving the impression that the isotherms are moved inwards with respect the obtained solution plot, in which only nodes inside the domain are represented (those which are the actual unknowns of the problem).

Below, a series of contour plots showing the temporal evolution of the rod during 10,000 seconds are presented. The simulation has been stopped at such time because of the instructions given at [11] and the fact that a steady solution would not be reached as the boundary conditions are time-dependent.



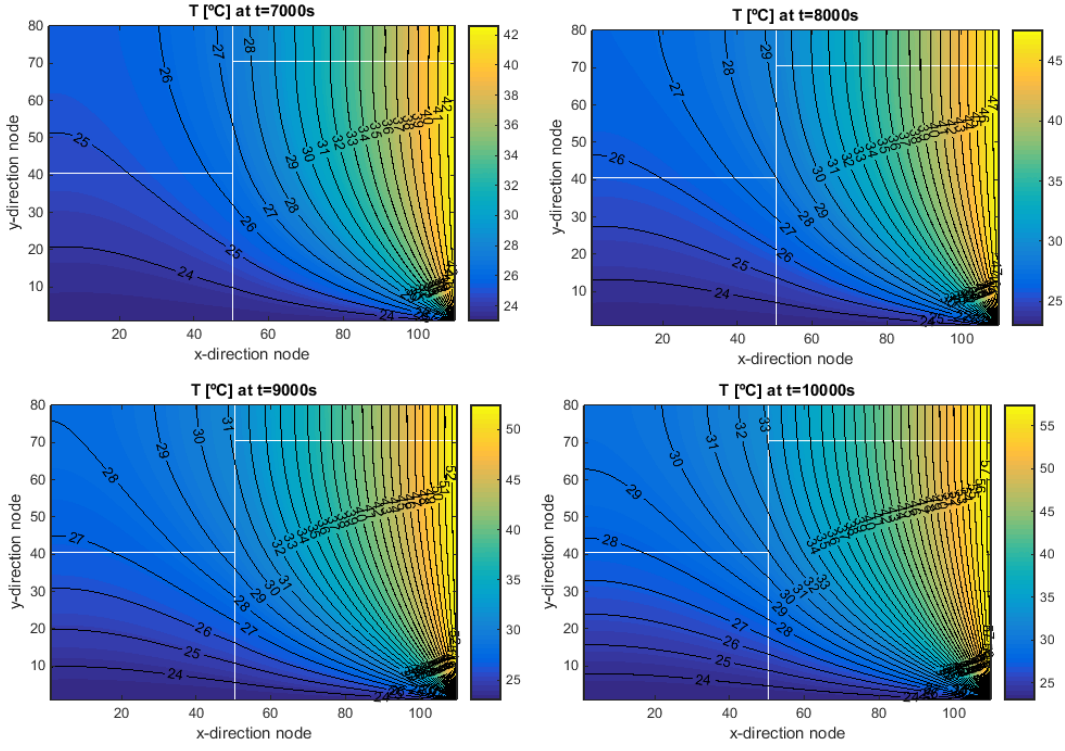


Figure 6: Temperature contour plots at different simulation times.

The temperature time-evolution of two specific points in the rod is plotted. Both points start at the initial temperature of  $8^{\circ}\text{C}$  and the point closer to the centre (blue line) increases its temperature faster than the other point, which is closer to the right wall, mainly because of the bottom wall being at higher temperature. Since the right wall increases its temperature continuously with time, there is a moment in which the tendency is inverted and the point closer to the right side (red line) is the one in which temperature grows more rapidly.

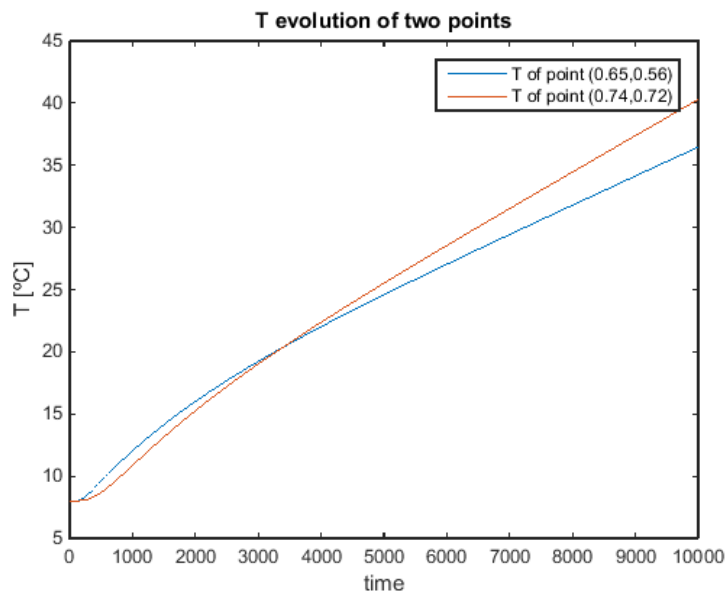


Figure 7: Temperature temporal evolution of two points.

### 3 Smith Hutton Problem

#### 3.1 Definition of the problem

##### 3.1.1 General description

This problem was proposed by R.M. Smith and A.G. Hutton in 1982. It is a test problem which permits the evaluation of different numerical models concerning the convection-diffusive problems such as streamline curvature and steep variations in the transported variable.

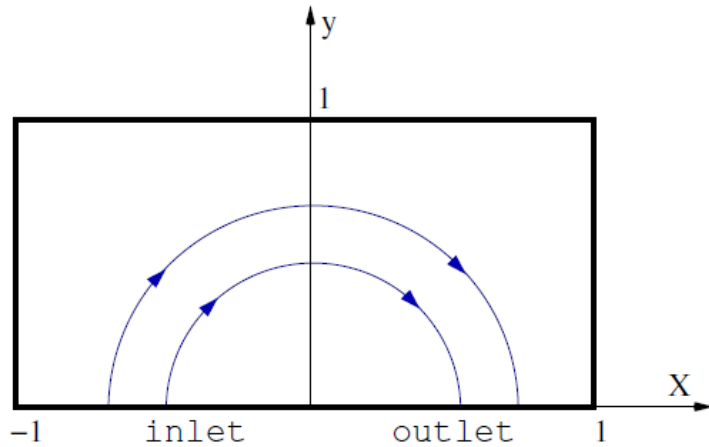


Figure 8: General scheme of the problem. Extracted from [12].

It consists of a rectangular cavity, with one inlet and one outlet. The velocity field of the fluid is known, and it enters the cavity with a prescribed value of the variable of study (figure 9). By evaluating the value of this variable at the outlet one may see the dominance of the convective terms over the diffusive, or vice versa.

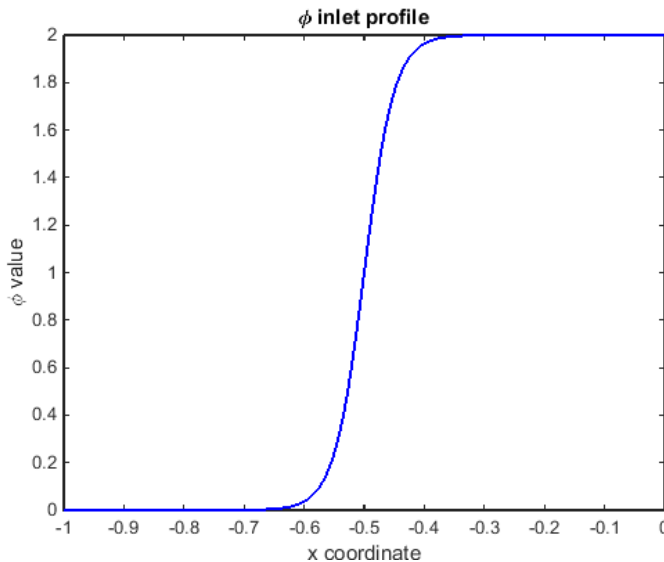


Figure 9: Variable's profile at the cavity inlet.

### 3.1.2 Nomenclature

|   |   |
|---|---|
| <b>Problem data</b>   | $N_y$ : number of CV in y-direction   |
| $\rho$ : density of the fluid                                 | $\Delta t$ : time step  |
| $\Gamma$ : diffusion coefficient                              | $\Delta x$ : mesh horizontal size   |
| $\alpha$ : problem parameter                                  | $\Delta y$ : mesh vertical size   |
| $\phi_i$ : variable of study at inlet                         | $\gamma$ : mesh concentration factor  |
| $\phi_{wall}$ : variable of study at the rest of the boundary | $\Delta x_d$ : horizontal nodal distance  |
|   | $\Delta y_d$ : vertical nodal distance  |
|   | $F$ : volumetric flux (i.e. $\int_{\partial\Omega}  \mathbf{v} \cdot d\mathbf{S} $ )              |
| <b>Problem variables</b>                                      | <b>Subscripts</b>   |
| $\phi$ : variable of study                                    | $\phi_n, \phi_s, \phi_e, \phi_w$ refer to the wall of the volume at which variables are evaluated |
| $x$ : horizontal coordinate                                   | $\phi_N, \phi_S, \phi_E, \phi_W, \phi_P$ refer to the node at which variables are evaluated       |
| $y$ : vertical coordinate                                     |   |
| $u$ : horizontal velocity                                     |   |
| $v$ : vertical velocity                                       |   |
| $\mathbf{v}$ : velocity field (vector)                        |   |
| $t$ : time  |   |
| <b>Numerical data</b>   | <b>Superscripts</b>   |
| $N$ : number of control volumes                               | $\phi^{n+1}$ : current instant  |
| $N_x$ : number of CV in x-direction                           | $\phi^n$ : previous instant   |

### 3.1.3 Governing equations

The equation related to this problem is the two-dimensional convection-diffusion equation.

$$\frac{\partial(\rho\phi)}{\partial t} + \nabla \cdot (\rho\mathbf{v}\phi) = \nabla \cdot (\Gamma\nabla\phi) + S \quad (3.1)$$

The variable of study is  $\phi$ . In the Smith Hutton problem there are no source terms. Besides, applying the conservation of mass and supposing constant physical properties ( $\Gamma$ ), one may rewrite this equation as follows:

$$\frac{\partial\phi}{\partial t} + \mathbf{v} \cdot \nabla\phi = \frac{\Gamma}{\rho}\nabla^2\phi \quad (3.2)$$

The main parameter of study is the ratio  $\Gamma/\rho$  which will determine the predominance of the diffusive terms in front of the convective.

The velocity field, as it has been said in previous lines, is prescribed and given by

$$u(x, y) = 2y(1 - x^2) \quad (3.3)$$

$$v(x, y) = -2x(1 - y^2) \quad (3.4)$$

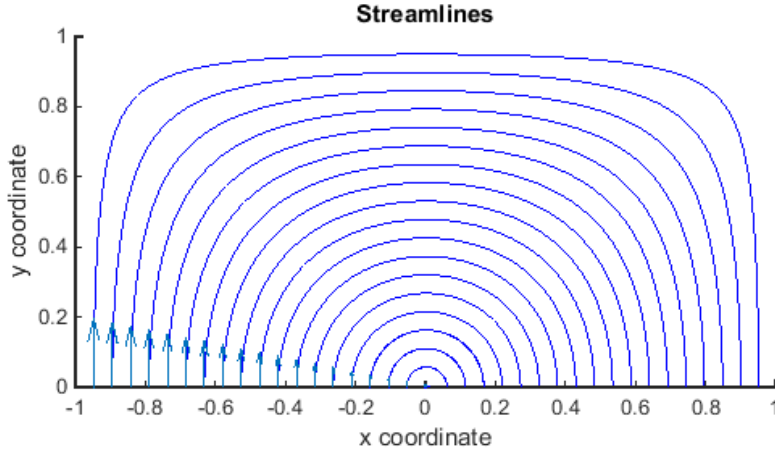


**Figure 10: Streamlines of the prescribed velocity field.**

It is direct to show that this flow is incompressible

$$\nabla \cdot \mathbf{v} = \frac{\partial u}{\partial x} + \frac{\partial v}{\partial y} = \frac{\partial(2y(1-x^2))}{\partial x} - \frac{\partial(2x(1-y^2))}{\partial y} = -4xy + 4xy = 0$$

The boundary conditions are

$$\phi_i = 1 + \tanh(\alpha(2x + 1)) \quad y = 0; x \in (-1, 0) \quad (\text{inlet}) \quad (3.5)$$

$$\frac{\partial \phi}{\partial y} = 0 \quad y = 0; x \in (0, 1) \quad (\text{outlet}) \quad (3.6)$$

$$\phi_{wall} = 1 - \tanh(\alpha) \quad (\text{elsewhere}) \quad (3.7)$$

### 3.2 Numerical methods

#### 3.2.1 Time-integration

To avoid numerical instabilities due to an explicit time scheme, it is preferable to use a fully implicit method. Integrating equation 3.2 over a certain time step

$$\int_{t^n}^{t^{n+1}} \frac{\partial \phi}{\partial t} dt = \int_{t^n}^{t^{n+1}} \left[ -\mathbf{v} \cdot \nabla \phi + \frac{\Gamma}{\rho} \nabla^2 \phi \right] dt$$

Leading to

$$\frac{\phi^{n+1} - \phi^n}{\Delta t} = -\mathbf{v} \cdot \nabla \phi^{n+1} + \frac{\Gamma}{\rho} \nabla^2 \phi^{n+1} \quad (3.8)$$

### 3.2.2 Spatial-integration

Equation 3.8 needs to be integrated over every control volume in order to obtain a set of linear equations.

$$\int_{\Omega} \frac{\phi^{n+1} - \phi^n}{\Delta t} d\Omega = \int_{\Omega} \left[ -\mathbf{v} \cdot \nabla \phi^{n+1} + \frac{\Gamma}{\rho} \nabla^2 \phi^{n+1} \right] d\Omega$$

*Transient term*

$$\int_{\Omega} \frac{\phi^{n+1} - \phi^n}{\Delta t} d\Omega \approx \frac{\phi_p^{n+1} - \phi_p^n}{\Delta t} \Delta x \Delta y \quad (3.9)$$

*Convective term*

$$\begin{aligned} \int_{\Omega} \mathbf{v} \cdot \nabla \phi^{n+1} d\Omega &= \int_{\Omega} \nabla \cdot (\mathbf{v} \phi^{n+1}) d\Omega = \oint_{\partial\Omega} \mathbf{v} \phi^{n+1} \cdot \hat{\mathbf{n}} dS \approx \\ &\approx F_e \phi_e^{n+1} + F_n \phi_n^{n+1} - F_w \phi_w^{n+1} - F_s \phi_s^{n+1} \end{aligned} \quad (3.10)$$

*Diffusive term*

$$\begin{aligned} \int_{\Omega} \nabla^2 \phi^{n+1} d\Omega &= \oint_{\partial\Omega} \nabla \phi^{n+1} \cdot \hat{\mathbf{n}} dS \approx \\ &\left( \frac{\partial \phi^{n+1}}{\partial x} \Big|_e - \frac{\partial \phi^{n+1}}{\partial x} \Big|_w \right) \Delta y + \left( \frac{\partial \phi^{n+1}}{\partial y} \Big|_n - \frac{\partial \phi^{n+1}}{\partial y} \Big|_s \right) \Delta x \approx \\ &\approx \left( \frac{\phi_E^{n+1} - \phi_P^{n+1}}{\Delta x_{d_e}} - \frac{\phi_P^{n+1} - \phi_W^{n+1}}{\Delta x_{d_w}} \right) \Delta y \\ &\quad + \left( \frac{\phi_N^{n+1} - \phi_P^{n+1}}{\Delta y_{d_n}} - \frac{\phi_P^{n+1} - \phi_S^{n+1}}{\Delta y_{d_s}} \right) \Delta x \end{aligned} \quad (3.11)$$

These approximations lead to a linear equation with respect to  $\phi$ , which is the same in all the volumes except the ones in contact with the boundary if a CDS scheme to evaluate the variable's value at the walls of every cell is used.

$$a_P \phi_P^{n+1} + a_N \phi_N^{n+1} + a_S \phi_S^{n+1} + a_E \phi_E^{n+1} + a_W \phi_W^{n+1} = b_P \quad (3.12)$$

The coefficients that appear in this equation are listed below.

$$a_P = \frac{\Delta x \Delta y}{\Delta t} + \frac{\Gamma}{\rho} \left( \frac{\Delta y}{\Delta x_{d_e}} + \frac{\Delta x}{\Delta y_{d_n}} + \frac{\Delta y}{\Delta x_{d_w}} + \frac{\Delta x}{\Delta y_{d_s}} \right) + \frac{F_e^{n+1}}{2} + \frac{F_n^{n+1}}{2} - \frac{F_w^{n+1}}{2} - \frac{F_s^{n+1}}{2} \quad (3.13)$$

$$a_N = -\frac{\Gamma}{\rho} \frac{\Delta x}{\Delta y_{d_n}} + \frac{F_n^{n+1}}{2} \quad (3.14)$$

$$a_S = -\frac{\Gamma}{\rho} \frac{\Delta x}{\Delta y_{d_s}} - \frac{F_s^{n+1}}{2} \quad (3.15)$$

$$a_E = -\frac{\Gamma}{\rho} \frac{\Delta y}{\Delta x_{d_e}} + \frac{F_e^{n+1}}{2} \quad (3.16)$$

$$a_W = -\frac{\Gamma}{\rho} \frac{\Delta y}{\Delta x_{d_w}} - \frac{F_w^{n+1}}{2} \quad (3.17)$$

$$b_P = \frac{\phi_P^n \Delta x \Delta y}{\Delta t} \quad (3.18)$$

This coefficients are different at the volumes in contact with the boundary of the domain.

$$b'_P = b_P - a_N \phi_{wall} , \quad a'_N = 0 \quad (\text{if north side}) \quad (3.19)$$

$$b'_P = b_P - a_E \phi_{wall} , \quad a'_E = 0 \quad (\text{if east side}) \quad (3.20)$$

$$b'_P = b_P - a_W \phi_{wall} , \quad a'_W = 0 \quad (\text{if west side}) \quad (3.21)$$

$$b'_P = b_P - a_S \phi_i , \quad a'_S = 0 \quad (\text{if inlet}) \quad (3.22)$$

$$a'_P = a_P + a_S , \quad a'_S = 0 \quad (\text{if inlet}) \quad (3.23)$$

An upwind scheme will also be used in order to compare the results of each scheme. When using such scheme, the coefficients for each volume are not necessarily equal. They depend on the direction of the flow in each wall of the

volume. The coefficients are not to be listed again. Instead an example of the coefficient  $a_N$  and the contribution of this cell's wall to the nodal coefficient  $a_P$  ( $a_P|_N$ ) are shown.

$$\begin{aligned} a_P|_N &= \frac{\Gamma}{\rho} \frac{\Delta x}{\Delta y_{d_n}} + F_n^{n+1} ; \quad a_N = -\frac{\Gamma}{\rho} \frac{\Delta x}{\Delta y_{d_n}} \quad (v_n > 0) \\ a_P|_N &= \frac{\Gamma}{\rho} \frac{\Delta x}{\Delta y_{d_n}} ; \quad a_N = -\frac{\Gamma}{\rho} \frac{\Delta x}{\Delta y_{d_n}} + F_n^{n+1} \quad (v_n < 0) \end{aligned} \quad (3.24)$$

### 3.3 Results and discussion

This problem has been solved by using a second order approximation (CDS) in the first case, and a first order scheme (Upwind) in the second. The numerical simulation parameters of each case are shown in the following table.

| Case          | $N_x$ | $\gamma_x$       | $N_y$ | $\gamma_y$       | $N$ | $\Delta t$ | order           |
|---------------|-------|------------------|-------|------------------|-----|------------|-----------------|
| A<br>(CDS)    | 400   | 0.0<br>(uniform) | 200   | 0.0<br>(uniform) | 80K | 0.001      | 2 <sup>nd</sup> |
| B<br>(Upwind) | 400   | 0.0<br>(uniform) | 200   | 0.0<br>(uniform) | 80K | 0.001      | 1 <sup>st</sup> |

Table 5: Simulation parameters of each case.

#### 3.3.1 Case A (CDS)

In the following plots the prevalence of the convective term over the diffusive may be clearly seen. Beginning from a ratio of  $\rho/\Gamma = 10$ , corresponding to the first picture in figure 11, one sees as the diffusion phenomenon plays an important role.  $\phi$  values seem to fade away in their journey from the inlet to the outlet. As the  $\rho/\Gamma$  ratio increases diffusion becomes every time less and less effective in comparison with convective transport, up to a point where the values at the outlet of the cavity are very close to the inlet profile. In this last case, the property is transported from the inlet to the outlet of the cavity following its corresponding streamline almost without fading away. This is why one obtains such a clearly defined plot.

The tendency shown by these images may be seen with more clarity in figure 12. One may observe that the outlet profile for the highest  $\rho/\Gamma$  ratio is almost coincident with the symmetric inlet profile, whereas the outlet values for the lowest ratio are completely different, being the outlet profile much more smooth because of the diffusive preponderance.

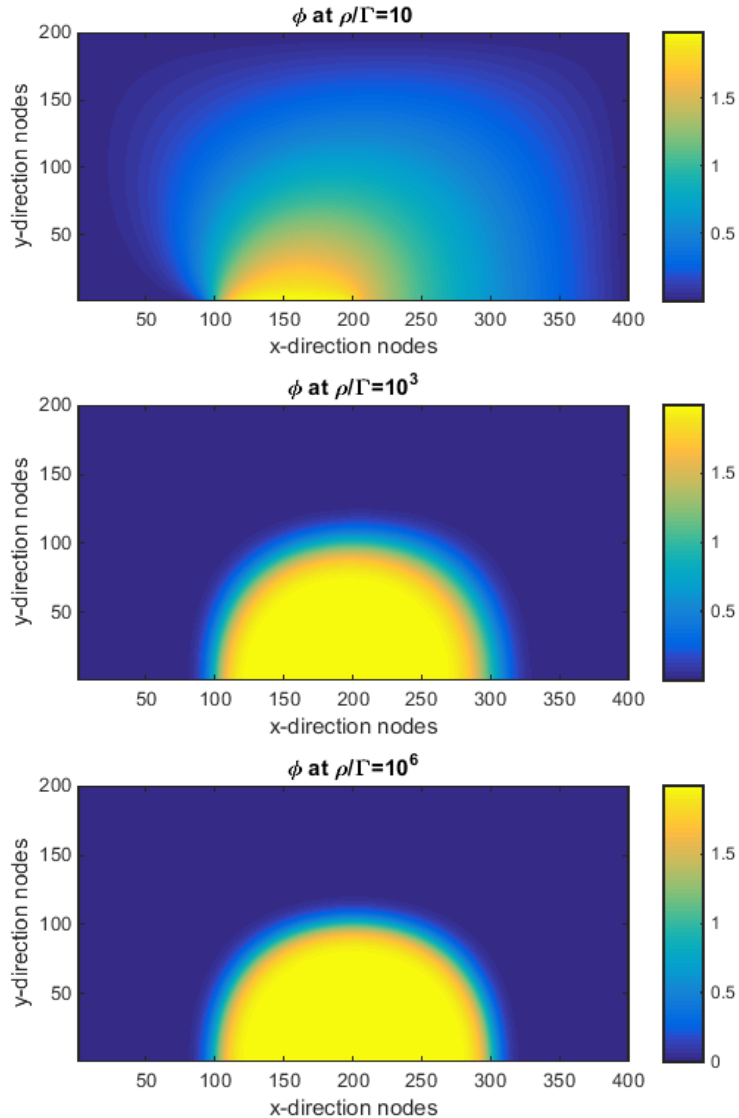


Figure 11:  $\phi$  contour plots for different  $\rho/\Gamma$  ratios. Results obtained with a CDS scheme.

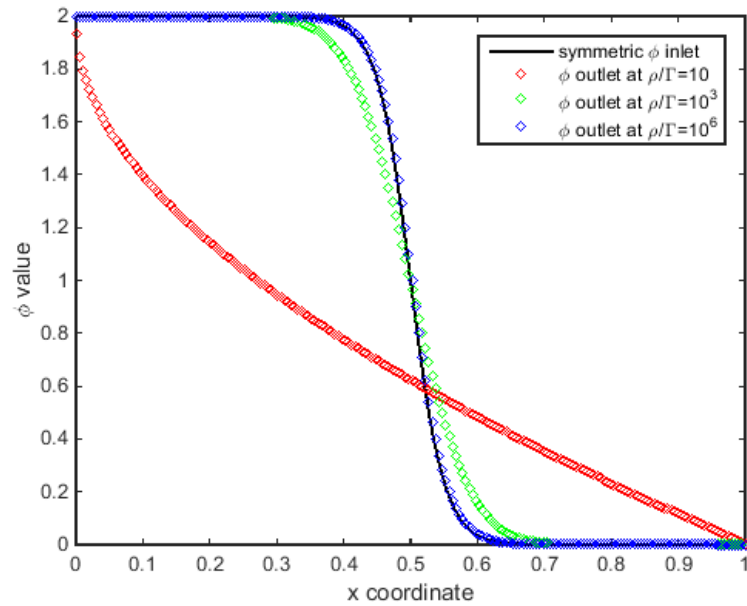


Figure 12: Comparison of the outlet the inlet profile. Results obtained with a CDS scheme.

### 3.3.2 Case B (Upwind)

Results obtained with an upwind scheme are less accurate, for being this scheme of lower order compared to CDS. Besides, this error introduces extra diffusion, as the error is proportional to the first derivative at the walls (the diffusive term, when integrated over a control volume forces the appearance of the first order derivatives at the cell's walls). For instance, considering a generic control volume and assuming positive horizontal velocity, the variable at east wall is, by means of an upwind scheme:

$$\phi_e \approx \phi_P \quad (3.20)$$

If one considers the first order Taylor series in x-direction about east face:

$$\phi_P = \phi_e - \frac{\partial \phi}{\partial x} \Big|_e \frac{\Delta x}{2} + \sigma \left( \left( \frac{\Delta x}{2} \right)^2 \right) \quad (3.21)$$

Then, one is introducing an error which is

$$error = - \frac{\partial \phi}{\partial x} \Big|_e \frac{\Delta x}{2} + \sigma \left( \left( \frac{\Delta x}{2} \right)^2 \right) \quad (3.22)$$

This error is introduced in the convective term, and it is multiplied by  $u_e$ , which is positive. Then, this term, if passed to the other side of the equation, has the same sign than the derivative resulting from the diffusive term. Therefore, this error is artificially increasing diffusion. This effect could be equally shown independently of the direction of the velocity and the wall one considers: the global effect of the upwind scheme is to add extra diffusion, which despite of being beneficial to convergence as it is more stable than CDS schemes it noticeably distorts the results.

The effect of this inherent property of the upwind scheme is seen in the plots below, especially in the last plot in figure 13, which appears to be less clear defined than its analogous for CDS. This effect is more obvious in figure 14, where even the outlet profile of the highest  $\rho/\Gamma$  ratio differs noticeably from the inlet values.

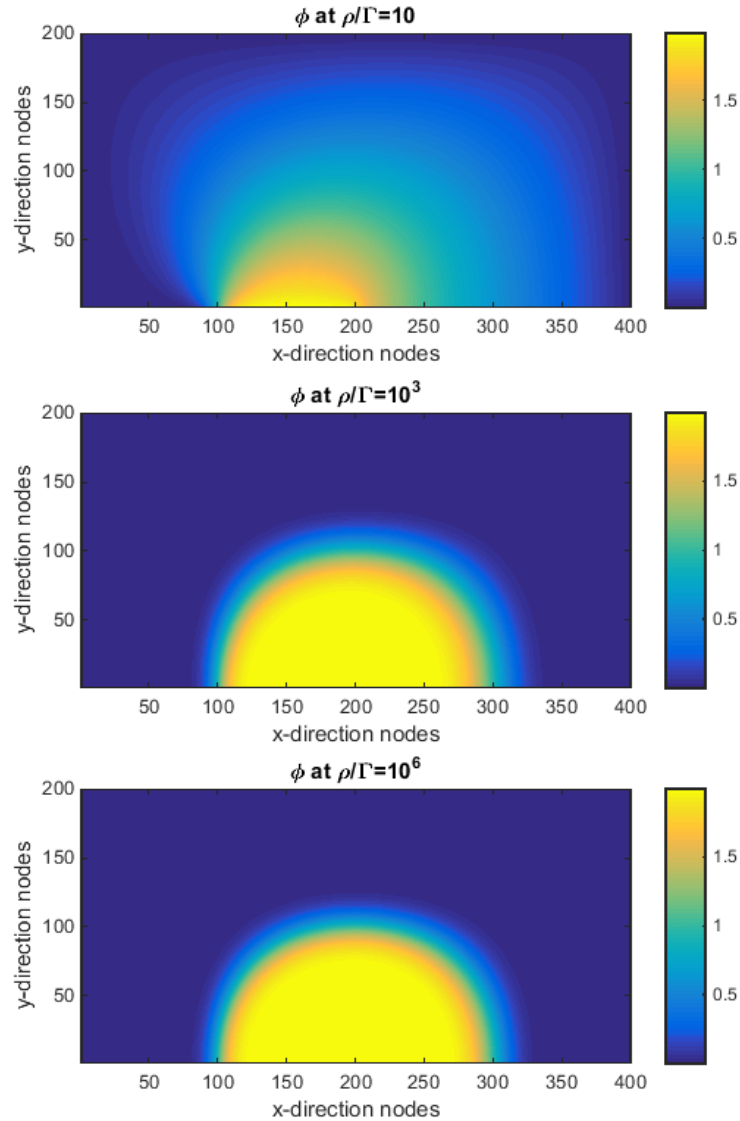


Figure 13:  $\phi$  contour plots for different  $\rho/\Gamma$  ratios. Results obtained with an upwind scheme.

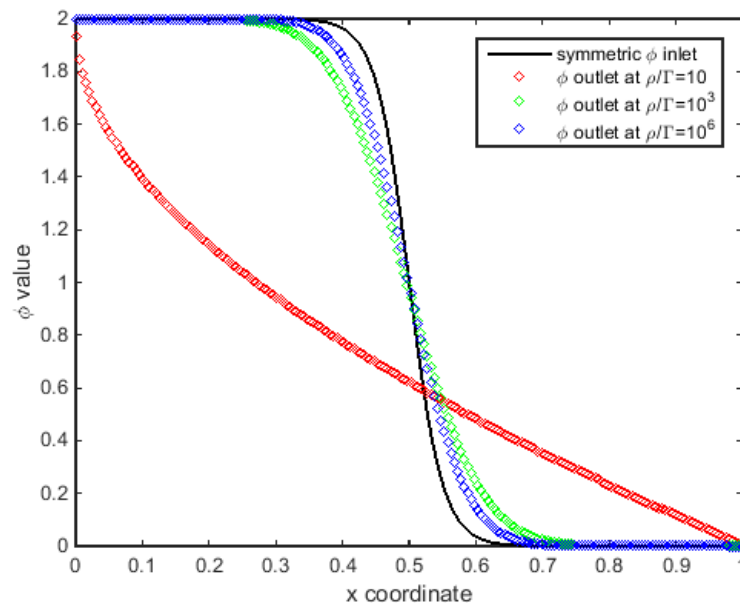


Figure 14: Comparison of the outlet and the inlet profile. Results obtained with an upwind scheme.

### 3.3.3 Code verification

Initially, the obtained results were not accurate enough to match the benchmark solution provided in [12]. The discrepancies were more noticeable for higher  $\rho/\Gamma$  ratios, so it was presumable that the source of error may concern the convective term. Therefore, the problem was analysed assuming no convective terms (i.e.  $\nu = 0$ ) and applying the Method of the Manufactured Solutions [13]. It basically consists in inventing a solution of the problem, substituting it in the original equation (3.2) and find a source term which satisfies the equation. Then, the source term is added to the discretized equations and the problem is solved. The error between the invented solution and the discretized solution is plotted for different mesh resolutions. The error should have the slope predicted by the lower order of accuracy of all the approximations used. In this case, the approximations used were of second order of accuracy and the plot obtained had a slope closer to a first order. Then, it was clear that the convective term presented an error. Thus, this was a useful way to detect where the error was.

Figure 15 shows the corresponding plot of the error once the problem in the code was mended. It can be seen how the error diminishes in two order of magnitude when the mesh is 10 times finer.

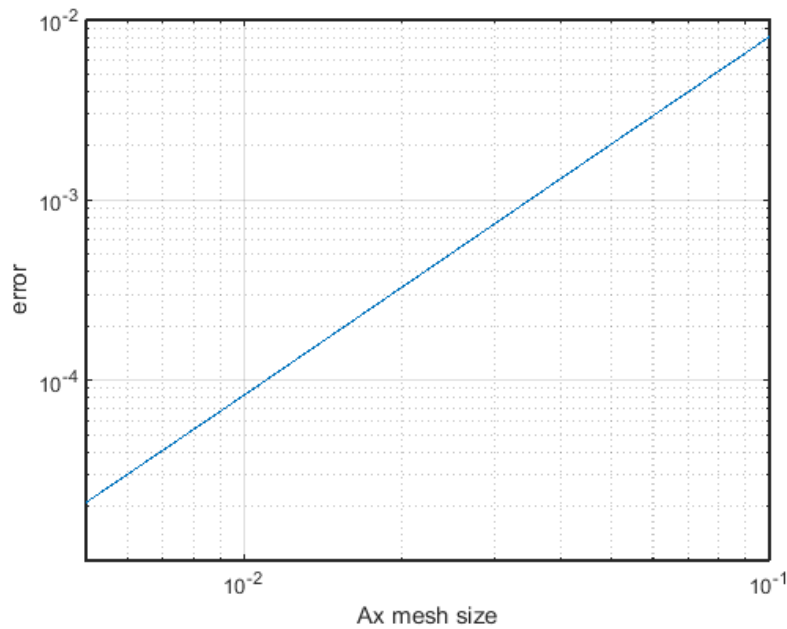


Figure 15: error vs mesh size corresponding to second order approximations.

## 4 Lid Driven Cavity

### 4.1 Definition of the problem

#### 4.1.1 General description

The Lid Driven Cavity is a classical problem in which the laminar incompressible flow in a squared cavity whose top wall moves with uniform velocity in its own plane is studied. It is commonly used as a model problem in order to test and evaluate numerical methods and techniques.

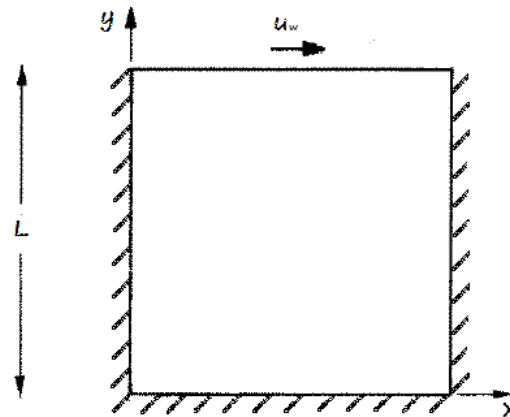


Figure 16: Sketch of the Lid Driven Cavity problem.

#### 4.1.2 Nomenclature

| Problem data   | Numerical data  |
|--|---|
| $L$ : square side dimension                                      | $N$ : number of control volumes   |
| $\rho$ : density of the fluid                                    | $N_x$ : number of CV in x-direction   |
| $\mu$ : dynamic viscosity  | $N_y$ : number of CV in y-direction   |
| $u_w$ : speed of the upper wall                                  | $\Delta t$ : time step  |
| $Re$ : Reynolds number   | $\Delta x$ : mesh horizontal size   |
| <br>   | $\Delta y$ : mesh vertical size   |
| <b>Problem variables</b>   | $\Delta x_d$ : horizontal nodal distance  |
| $x$ : horizontal coordinate                                      | $\Delta y_d$ : vertical nodal distance  |
| $y$ : vertical coordinate  | $F$ : volumetric flux (i.e. $\int_{\partial\Omega} \mathbf{v} \cdot d\mathbf{S}$ )                |
| $\mathbf{r}$ : coordinates (vector)                              | <br>  |
| $u$ : horizontal velocity  | <b>Subscripts</b>   |
| $v$ : vertical velocity  | $\phi_n, \phi_s, \phi_e, \phi_w$ refer to the wall of the volume at which variables are evaluated |
| $\mathbf{v}$ : velocity field (vector)                           | $\phi_N, \phi_S, \phi_E, \phi_W, \phi_P$ refer to the node at which variables are evaluated       |
| $\mathbf{R}(\mathbf{v})$ : convective + diffusive + source terms | <br>  |
| $p$ : pressure   | <b>Superscripts</b>   |
| $\psi$ : stream function   | $\phi^{n+1}$ : current instant  |
| $t$ : time   | $\phi^n$ : previous instant   |
|  | $\phi^{n-1}$ : previous to previous instant   |

### 4.1.3 Governing equations

The fluid motion is governed by the Navier-Stokes equations. Assuming incompressible flow and 2-D movement (hence the gravity term does not contribute), the equations read:

$$\nabla \cdot \mathbf{v} = 0 \quad (4.1a)$$

$$\rho \left( \frac{\partial \mathbf{v}}{\partial t} + (\mathbf{v} \cdot \nabla) \mathbf{v} \right) = -\nabla p + \mu \nabla^2 \mathbf{v} \quad (4.2a)$$

### Non-dimensional equations

One may convert these equations into dimensionless expressions, in order to force the appearance of the Reynolds number, which will be the main parameter of the study. For this purpose, the following dimensionless variables are defined using the problem's parameters.

$$\tilde{\mathbf{r}} = \frac{\mathbf{r}}{L} \quad (4.3)$$

$$\tilde{\mathbf{v}} = \frac{\mathbf{v}}{u_w} \quad (4.4)$$

$$\tilde{t} = \frac{t}{L/u_w} \quad (4.5)$$

$$\tilde{p} = \frac{p}{\rho u_w^2} \quad (4.6)$$

Rewriting momentum equation (4.2a) by substituting the expressions above leads to:

$$\begin{aligned} \rho \frac{\partial(\tilde{\mathbf{v}} u_w)}{\partial(\tilde{t} L/u_w)} + \rho \left( \tilde{\mathbf{v}} u_w \cdot \frac{1}{L} \tilde{\nabla} \right) \tilde{\mathbf{v}} u_w &= -\frac{1}{L} \tilde{\nabla}(\tilde{p} \rho u_w^2) + \mu \frac{1}{L^2} \tilde{\Delta}(\tilde{\mathbf{v}} u_w) \\ \frac{\rho u_w^2}{L} \frac{\partial \tilde{\mathbf{v}}}{\partial \tilde{t}} + \frac{\rho u_w^2}{L} (\tilde{\mathbf{v}} \cdot \tilde{\nabla}) \tilde{\mathbf{v}} &= -\frac{\rho u_w^2}{L} \tilde{\nabla} \tilde{p} + \frac{\mu u_w}{L^2} \tilde{\Delta} \tilde{\mathbf{v}} \end{aligned}$$

And dividing all the equation by the factor  $\rho u_w^2 / L$  one obtains:

$$\frac{\partial \tilde{\mathbf{v}}}{\partial \tilde{t}} + (\tilde{\mathbf{v}} \cdot \tilde{\nabla}) \tilde{\mathbf{v}} = -\tilde{\nabla} \tilde{p} + \frac{\mu}{\rho u_w L} \tilde{\Delta} \tilde{\mathbf{v}}$$

Introducing the non-dimensional *Re* number of this problem:

$$Re = \frac{\rho u_w L}{\mu} \quad (4.7)$$

One finally gets the non-dimensional momentum equation. From this point on, for the sake of simplicity, the superscript  $(\tilde{\phi})$  denoting the dimensionless variables is suppressed, understanding that all the variables are dimensionless.

$$\frac{\partial \mathbf{v}}{\partial t} + (\mathbf{v} \cdot \nabla) \mathbf{v} = -\nabla p + \frac{1}{Re} \nabla^2 \mathbf{v} \quad (4.2b)$$

Similarly, for 1.1a one easily gets the non-dimensional equation of mass conservation:

$$\nabla \cdot \mathbf{v} = 0 \quad (4.1b)$$

## 4.2 Numerical methods

### 4.2.1 Time-integration

For this problem the Fractional Step Method was used, thus requiring an explicit time scheme. For this reason a second order Adams-Bashforth approximation was used. This method permits solving both the coupled equations of momentum and mass conservation at the same time.

In order to make the expressions more compact the next quantity is defined:

$$\mathbf{R}(\mathbf{v}) = -(\mathbf{v} \cdot \nabla) \mathbf{v} + \frac{1}{Re} \nabla^2 \mathbf{v} \quad (4.8)$$

Then

$$\frac{\partial \mathbf{v}}{\partial t} = \mathbf{R}(\mathbf{v}) - \nabla p \quad (4.2c)$$

Integrating equation 4.2c between the instant  $t^n$  and the following instant  $t^{n+1}$ :

$$\int_{t^n}^{t^{n+1}} \frac{\partial \mathbf{v}}{\partial t} dt = \mathbf{v}^{n+1} - \mathbf{v}^n = \int_{t^n}^{t^{n+1}} (\mathbf{R}(\mathbf{v}) - \nabla p) dt$$

The term  $\mathbf{R}(\mathbf{v})$ , as previously said, was evaluated explicitly using a second order Adams-Bashforth approximation, while the pressure gradient was integrated with respect time by using an implicit scheme. This is, in each time step pressure is unknown, while the convective, diffusive and source terms are computed with previous values.

$$\mathbf{v}^{n+1} = \mathbf{v}^n + (1.5\mathbf{R}(\mathbf{v}^n) - 0.5\mathbf{R}(\mathbf{v}^{n-1}) - \nabla p^{n+1})\Delta t \quad (4.9)$$

Following the Fractional Step Method, equations of mass and momentum conservation are solved by completing these three steps:

- Computing a predicted velocity field:

$$\mathbf{v}_{pred}^{n+1} = \mathbf{v}^n + (1.5\mathbf{R}(\mathbf{v}^n) - 0.5\mathbf{R}(\mathbf{v}^{n-1}))\Delta t \quad (4.10)$$

- Solving the Poisson equation for pressure:

$$\nabla^2 p^{n+1} \Delta t = \nabla \cdot \mathbf{v}_{pred}^{n+1} \quad (4.11)$$

- Correction of the predicted velocity with the pressure field obtained in the previous step:

$$\mathbf{v}^{n+1} = \mathbf{v}_{pred}^{n+1} - \nabla p^{n+1} \Delta t \quad (4.12)$$

Due to numerical stability reasons the explicit time-integration scheme requires severe restrictions on the time step. For this reason, the time step has to satisfy the next two conditions below (CFL condition [14]):

$$\Delta t \leq \frac{C_{conv}}{\left( \frac{|u_i|}{\Delta x_i} \right)_{max}} \quad (4.13)$$

$$\Delta t \leq Re \frac{C_{visc}}{\left( \frac{1}{\Delta x_i^2} \right)_{max}} \quad (4.14)$$

Where  $C_{conv}$  and  $C_{visc}$  are constants that must be smaller than unity. It is recommended that these values were 0.35 and 0.2 respectively.

#### 4.2.2 Spatial-integration

In this section the process through which the spatial continuous equations are turned into a discrete set of equations is exposed.

As said before, a fractional step method was used in order to obtain the velocity and pressure fields. Through this method one has to solve three different equations (4.10, 4.11 and 4.12) instead of the two original equations of mass (4.1b) and momentum (4.2b) conservation. The spatial integration of each step in the FSM is described in the following lines.

- Predicted velocity field

$$\int_{\Omega} \mathbf{v}_{pred}^{n+1} d\Omega = \int_{\Omega} [\mathbf{v}^n + (1.5\mathbf{R}(\mathbf{v}^n) - 0.5\mathbf{R}(\mathbf{v}^{n-1}))\Delta t] d\Omega$$

$$\boldsymbol{v}_{pred}^{n+1} \Delta x \Delta y = \boldsymbol{v}_P^n \Delta x \Delta y + \int_{\Omega} (1.5 \boldsymbol{R}(\boldsymbol{v}^n) - 0.5 \boldsymbol{R}(\boldsymbol{v}^{n-1})) \Delta t d\Omega \quad (4.15)$$

Integration of the  $\boldsymbol{R}(\boldsymbol{v})$  term requires special attention. Getting back to the definition of this term (4.8), the following contributions are addressed separately.

*Convective term*

$$\begin{aligned} \int_{\Omega} (\boldsymbol{v} \cdot \nabla) \boldsymbol{v} d\Omega &= \int_{\Omega} \nabla \cdot (\boldsymbol{v} \boldsymbol{v}) d\Omega = \oint_{\partial\Omega} \boldsymbol{v} \boldsymbol{v} \cdot \hat{\mathbf{n}} dS \approx \\ &\approx \boldsymbol{v}_e F_e + \boldsymbol{v}_n F_n - \boldsymbol{v}_w F_w - \boldsymbol{v}_s F_s = \left( \begin{array}{l} u_e F_e + u_n F_n - u_w F_w - u_s F_s \\ v_e F_e + v_n F_n - v_w F_w - v_s F_s \end{array} \right) \end{aligned} \quad (4.16)$$

*Diffusive term*

$$\begin{aligned} \int_{\Omega} \nabla^2 \boldsymbol{v} d\Omega &= \int_{\Omega} \nabla \cdot (\nabla \boldsymbol{v}) d\Omega = \oint_{\partial\Omega} \nabla \boldsymbol{v} \cdot \hat{\mathbf{n}} dS \approx \\ &\approx \frac{\partial \boldsymbol{v}}{\partial x} \Big|_e \Delta y + \frac{\partial \boldsymbol{v}}{\partial y} \Big|_n \Delta x - \frac{\partial \boldsymbol{v}}{\partial x} \Big|_w \Delta y - \frac{\partial \boldsymbol{v}}{\partial y} \Big|_s \Delta x \approx \\ &\approx \frac{\boldsymbol{v}_E - \boldsymbol{v}_P}{\Delta x_{d_e}} \Delta y + \frac{\boldsymbol{v}_N - \boldsymbol{v}_P}{\Delta y_{d_n}} \Delta x - \frac{\boldsymbol{v}_P - \boldsymbol{v}_W}{\Delta x_{d_w}} \Delta y - \frac{\boldsymbol{v}_P - \boldsymbol{v}_S}{\Delta y_{d_s}} \Delta x = \\ &= \left( \begin{array}{l} \frac{u_E - u_P}{\Delta x_{d_e}} \Delta y + \frac{u_N - u_P}{\Delta y_{d_n}} \Delta x - \frac{u_P - u_W}{\Delta x_{d_w}} \Delta y - \frac{u_P - u_S}{\Delta y_{d_s}} \Delta x \\ \frac{v_E - v_P}{\Delta x_{d_e}} \Delta y + \frac{v_N - v_P}{\Delta y_{d_n}} \Delta x - \frac{v_P - v_W}{\Delta x_{d_w}} \Delta y - \frac{v_P - v_S}{\Delta y_{d_s}} \Delta x \end{array} \right) \end{aligned} \quad (4.17)$$

– Pressure Poisson equation

$$\begin{aligned} \int_{\Omega} \nabla^2 p^{n+1} \Delta t d\Omega &= \int_{\Omega} \nabla \cdot (\nabla p^{n+1}) \Delta t d\Omega = \int_{\Omega} \nabla \cdot \boldsymbol{v}_{pred}^{n+1} d\Omega \\ &\Delta t \oint_{\partial\Omega} \nabla p^{n+1} \cdot \hat{\mathbf{n}} dS = \oint_{\partial\Omega} \boldsymbol{v}_{pred}^{n+1} \cdot \hat{\mathbf{n}} dS \end{aligned}$$

$$\begin{aligned} \Delta t \left( \frac{p_E - p_P}{\Delta x_{d_e}} \Delta y + \frac{p_N - p_P}{\Delta y_{d_n}} \Delta x - \frac{p_P - p_W}{\Delta x_{d_w}} \Delta y - \frac{p_P - p_S}{\Delta y_{d_s}} \Delta x \right)^{n+1} = \\ = (u_{pred_e}^{n+1} - u_{pred_w}^{n+1}) \Delta y + (v_{pred_n}^{n+1} - v_{pred_s}^{n+1}) \Delta x \end{aligned} \quad (4.18)$$

As this is the pressure at the current instant, and hence not known, this leads to a linear equation with respect to pressure, of the form:

$$a_P p_P^{n+1} + a_N p_N^{n+1} + a_S p_S^{n+1} + a_E p_E^{n+1} + a_W p_W^{n+1} = b_P \quad (4.19)$$

Where each of the coefficients is computed as follows:

$$a_P = \frac{\Delta y}{\Delta x_{d_e}} + \frac{\Delta x}{\Delta y_{d_n}} + \frac{\Delta y}{\Delta x_{d_w}} + \frac{\Delta x}{\Delta y_{d_s}} \quad (4.20)$$

$$a_N = -\frac{\Delta x}{\Delta y_{d_n}} \quad (4.21)$$

$$a_S = -\frac{\Delta x}{\Delta y_{d_s}} \quad (4.22)$$

$$a_E = -\frac{\Delta y}{\Delta x_{d_e}} \quad (4.23)$$

$$a_W = -\frac{\Delta y}{\Delta x_{d_w}} \quad (4.24)$$

$$b_P = -\frac{1}{\Delta t} [(u_{pred_e}^{n+1} - u_{pred_w}^{n+1}) \Delta y + (v_{pred_n}^{n+1} - v_{pred_s}^{n+1}) \Delta x] \quad (4.25)$$

The boundary conditions are clear. At the walls of the cavity pressure must accomplish:

$$\frac{\partial p}{\partial n} = 0 \quad (4.26)$$

Depending on the side of the volume in contact with the boundary, this condition is translated into the following modifications:

$$a'_P = a_P + a_N , \quad a_N' = 0 \text{ (if north side)} \quad (4.27)$$

$$a'_P = a_P + a_S , \quad a_S' = 0 \text{ (if south side)} \quad (4.28)$$

$$a'_P = a_P + a_E , \quad a_E' = 0 \text{ (if east side)} \quad (4.29)$$

$$a'_P = a_P + a_W , \quad a_W' = 0 \text{ (if west side)} \quad (4.30)$$

Obviously, for the volumes at the corners two of the sides will be part of the boundary, so the coefficients will be the result of the combination of both modifications.

- Velocity correction

$$\begin{aligned} \int_{\Omega} \mathbf{v}^{n+1} d\Omega &= \int_{\Omega} (\mathbf{v}_{pred}^{n+1} - \nabla p^{n+1} \Delta t) d\Omega \\ \mathbf{v}_P^{n+1} \Delta x \Delta y &= \mathbf{v}_{pred_P}^{n+1} \Delta x \Delta y - \Delta t \oint_{\partial\Omega} p^{n+1} \cdot \hat{\mathbf{n}} dS \\ \mathbf{v}_P^{n+1} \Delta x \Delta y &= \mathbf{v}_{pred_P}^{n+1} \Delta x \Delta y - \Delta t \left( \frac{(p_e^{n+1} - p_w^{n+1}) \Delta y}{(p_n^{n+1} - p_s^{n+1}) \Delta x} \right) \end{aligned} \quad (4.31)$$

For the resolution of the majority of cases a non-uniform mesh was used, for it is necessary to increase the density of the mesh at the areas which are more demanded. Thus, one obtains more accurate solutions without increasing the total number of nodes, which may help to reduce computational costs. Then an hyperbolic tangent distribution was used. The mesh size in x-direction of the  $i^{th}$  node reads:

$$\Delta x_i = \frac{\tanh\left(\gamma_x \left(\frac{2i}{N_x} - 1\right)\right) - \tanh\left(\gamma_x \left(\frac{2(i-1)}{N_x} - 1\right)\right)}{2\tanh \gamma_x} \quad (4.32)$$

Mesh sizes in y-direction are computed analogously. With a mesh concentration factor of 1.5 for both directions one obtains the following mesh distribution.

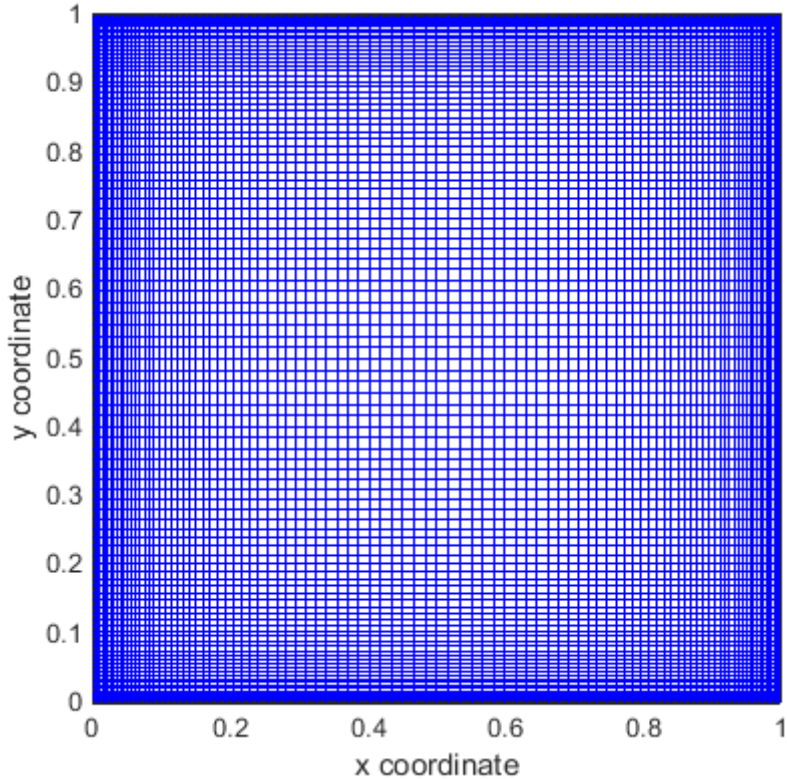


**Figure 17: Mesh distribution for a mesh concentration factor of  $\gamma = 1.5$ .**

Another significant issue concerning spatial discretization is the use of staggered meshes to solve momentum equation. Therefore, the first and third steps of the FSM are solved by means of staggered meshes while the second one (Poisson equation for pressure field) are solved in a normal (collocated) mesh. This procedure makes sure that the coupling between pressure and velocity fields is correct, preventing the appearance of the checkerboard problem [15], so called because converged velocity fields are obtained although the pressure field might present unrealistic distributions: pressure changes alternatively from 0 to a certain value from one node to another.

Staggered meshes depend on the direction to be solved. They are obtained by creating a control volume centred in the separation wall of two control volumes of the collocated mesh. Thus x-direction staggered meshes have one less column of control volumes and y-direction staggered meshes one less row. In the following figure both types of mesh are displayed. Notice that the meshes are non-uniform too.

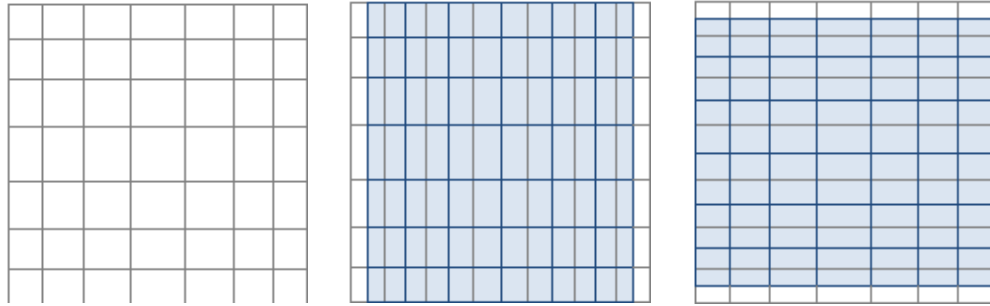


**Figure 18: Collocated mesh (left), x-direction (middle) and y-direction (right) staggered meshes**

From this point on, this type of meshes (staggered) are used to solve the momentum conservation equation together with the FSM. Other variables such as temperature or pressure are solved with collocated meshes.

#### 4.3 Results and discussion

In the following pages contour plots of horizontal and vertical components of the velocity field and streamlines are shown. The same variables will be displayed together in order to better-visualize the Reynolds effect. Six values of  $Re$  were simulated, from 100 to 7,500, since for  $Re$  higher than 7,500 solutions do not reach steady state any more.

| $Re$  | $N_x$ | $\gamma_x$       | $N_y$ | $\gamma_y$       | $N$ | order    |
|-------|-------|------------------|-------|------------------|-----|----------|
| 100   | 100   | 0.0<br>(uniform) | 100   | 0.0<br>(uniform) | 10K | $2^{nd}$ |
| 400   | 100   | 1.5              | 100   | 1.5              | 10K | $2^{nd}$ |
| 1,000 | 100   | 1.5              | 100   | 1.5              | 10K | $2^{nd}$ |
| 3,200 | 100   | 1.5              | 100   | 1.5              | 10K | $2^{nd}$ |
| 5,000 | 100   | 1.5              | 100   | 1.5              | 10K | $2^{nd}$ |
| 7,500 | 100   | 1.5              | 100   | 1.5              | 10K | $2^{nd}$ |

**Table 6: Lid Driven Cavity problem simulation parameters.**

#### 4.3.1 Contour plots

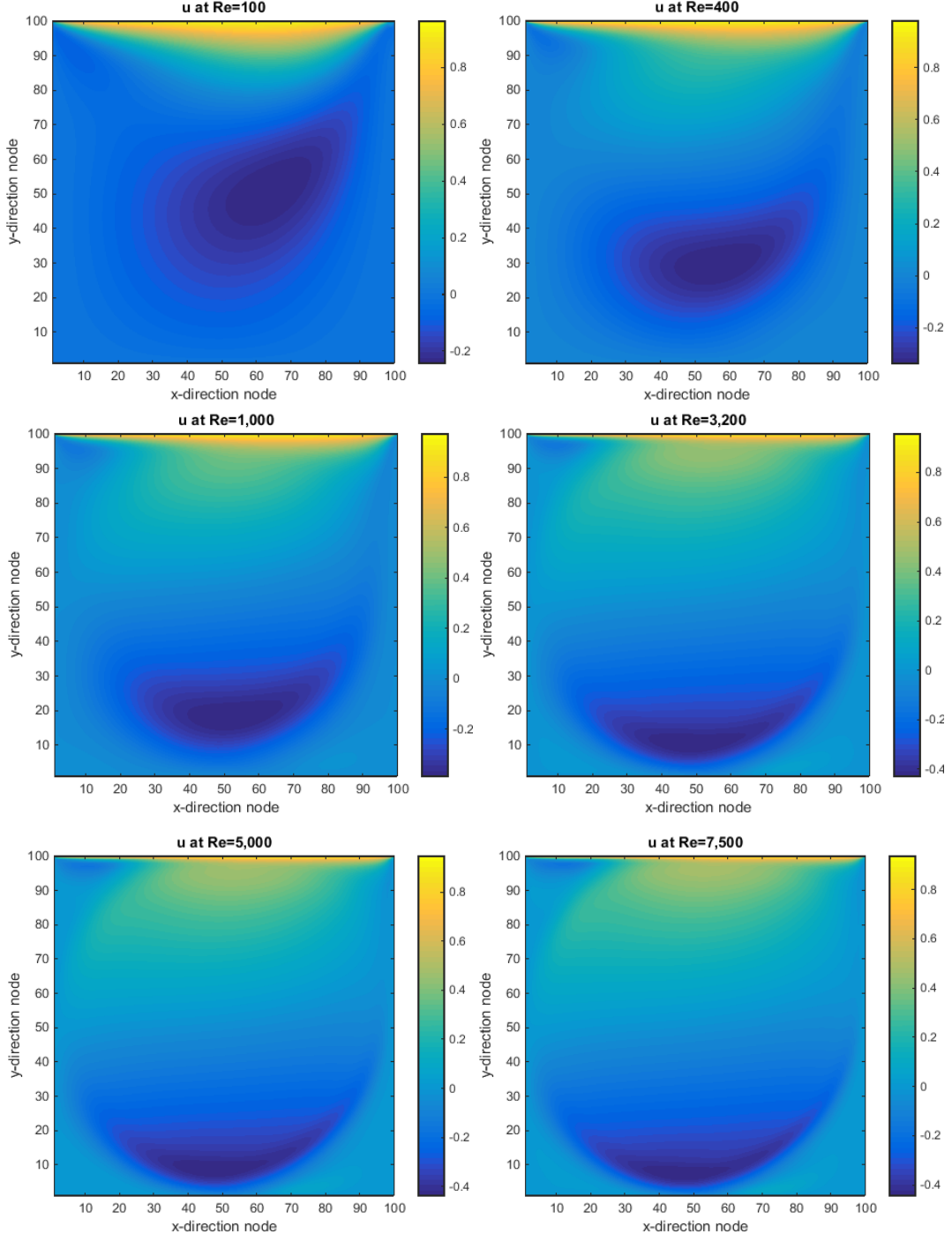
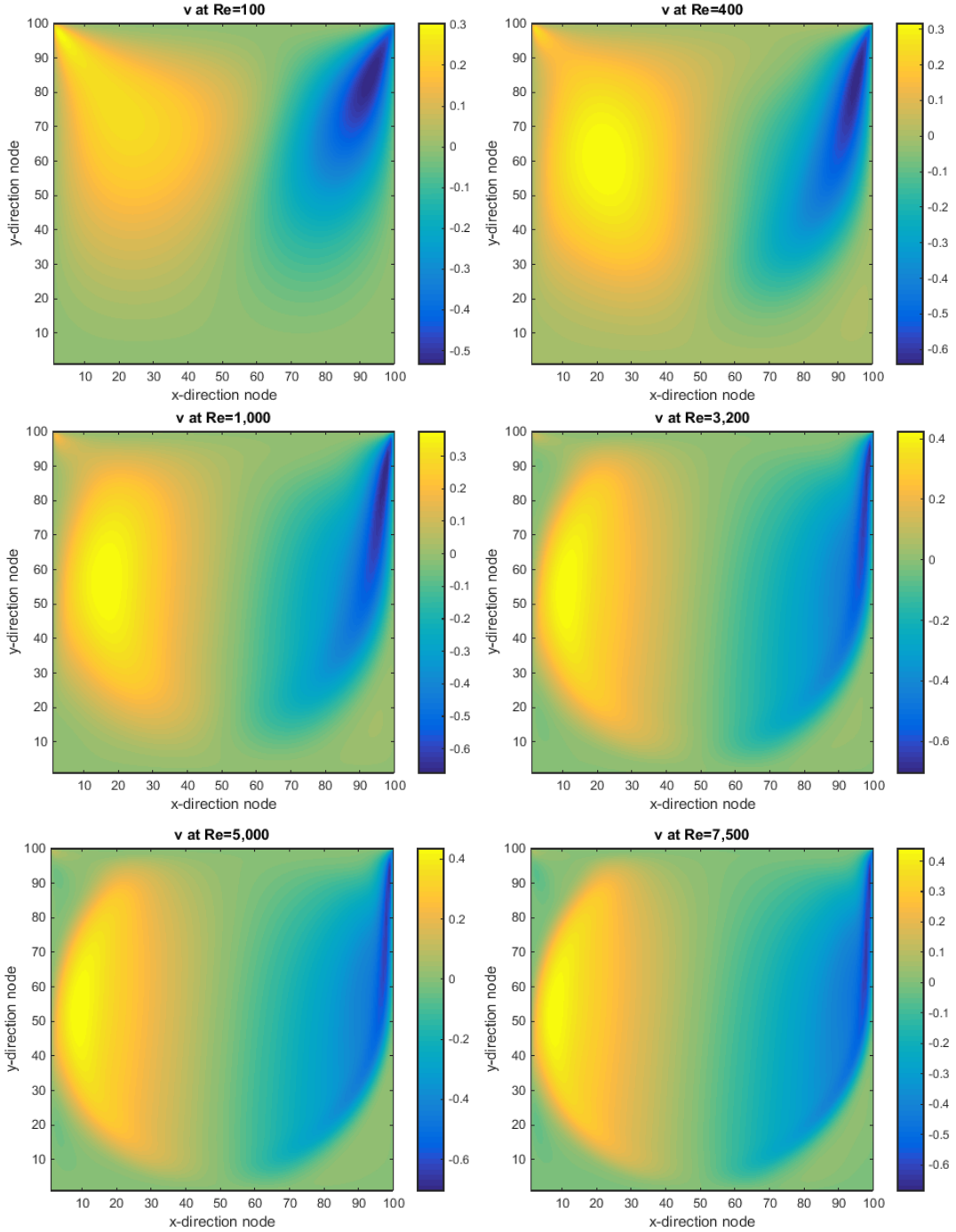


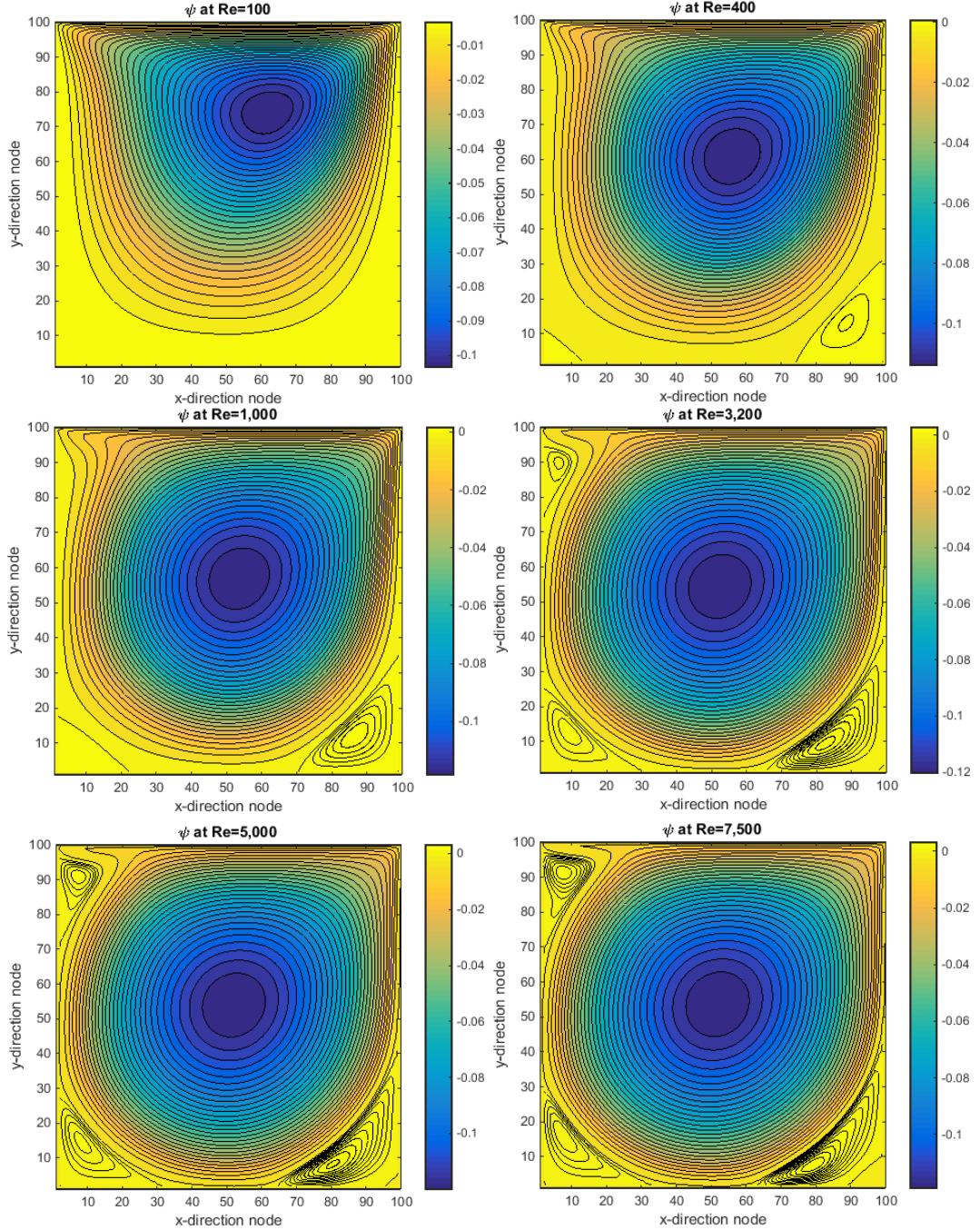
Figure 19: Velocity horizontal component  $u$  contour plots for different  $Re$ .

Figure 19 displays the contour plots of the horizontal component of velocity. The main remarkable aspect is the fact that the areas of positive (yellow) and negative velocity (dark blue) elongate with increasing  $Re$ , mainly because of the diffusive term being every time less predominant. These areas, in addition to stretching themselves, tend to move towards the walls.



**Figure 20: Velocity vertical component  $v$  contour plots for different  $Re$ .**

In the vertical component of velocity the same phenomenon is observed: due to the loss in significance of the convective term, the areas become more sharp and elongated, extending all along the streamlines. By observing both figures 19 and 20 one clearly sees the clockwise motion of the fluid inside the cavity.



**Figure 21: Stream function contour plots for different  $Re$ .**

Stream function is a scalar function which, by definition, accomplishes the following two expressions:

$$u = \frac{\partial \psi}{\partial y} \quad (4.33)$$

$$v = - \frac{\partial \psi}{\partial x} \quad (4.34)$$

Streamlines are the lines which are tangent to the velocity vector at each point of the domain:

$$\frac{u}{v} = \frac{dx}{dy} \quad (4.35)$$

Combining this last expression with 4.34 and 4.33 leads to:

$$\frac{\partial \psi}{\partial x} dx + \frac{\partial \psi}{\partial y} dy = 0 \quad (4.36)$$

Then, the current function is constant along a streamline, for its total derivative (4.36) is null. Then, by means of 4.33 and 4.34 the stream function is completely defined except for an integration constant, which may be set null at the coordinates origin. Then:

$$\psi(x, y) = \int_0^y u \partial y - \int_0^x v \partial x - \int_0^x \left( \int_0^y \frac{\partial u}{\partial x} \partial y \right) \partial x \quad (4.37)$$

By observing the series of plots one sees as the streamlines for lower Reynolds show a smoother flow, especially for  $Re = 100$ , where no strong eddies at the corners are detected. As Reynolds is increased, the centre of rotation moves towards the centre of the cavity and three eddies gain in strength. The first eddy makes its appearance at the lower-right corner of the cavity, followed by another at the lower-left corner while the last one appears at the upper-left corner.

#### 4.3.2 Comparison with benchmark solution

Next two figures show the comparison between the obtained results and a benchmark solution given in [16]. In these graphs, the values of horizontal velocity along a vertical line passing the cavity centre and the values of vertical velocity along a horizontal line through the cavity centre are compared.

All in all, the obtained results seem to agree completely with the benchmark values. In these plots the phenomenon which has been commented in previous lines is visible: the flow tends to concentrate at the wall proximities, thus increasing the gradients. Besides, the points at which velocity turns null move towards the cavity centre.

Of course, the results are not exactly coincident but they show the same trend and the same flow behaviour. Nevertheless, in figure 23 for  $Re = 400$  there is a point of the benchmark solution which diverts significantly from the obtained results. This is highly presumable to be a typographical error in the benchmark solution, for this value does not even agree with the tendency of the other points.

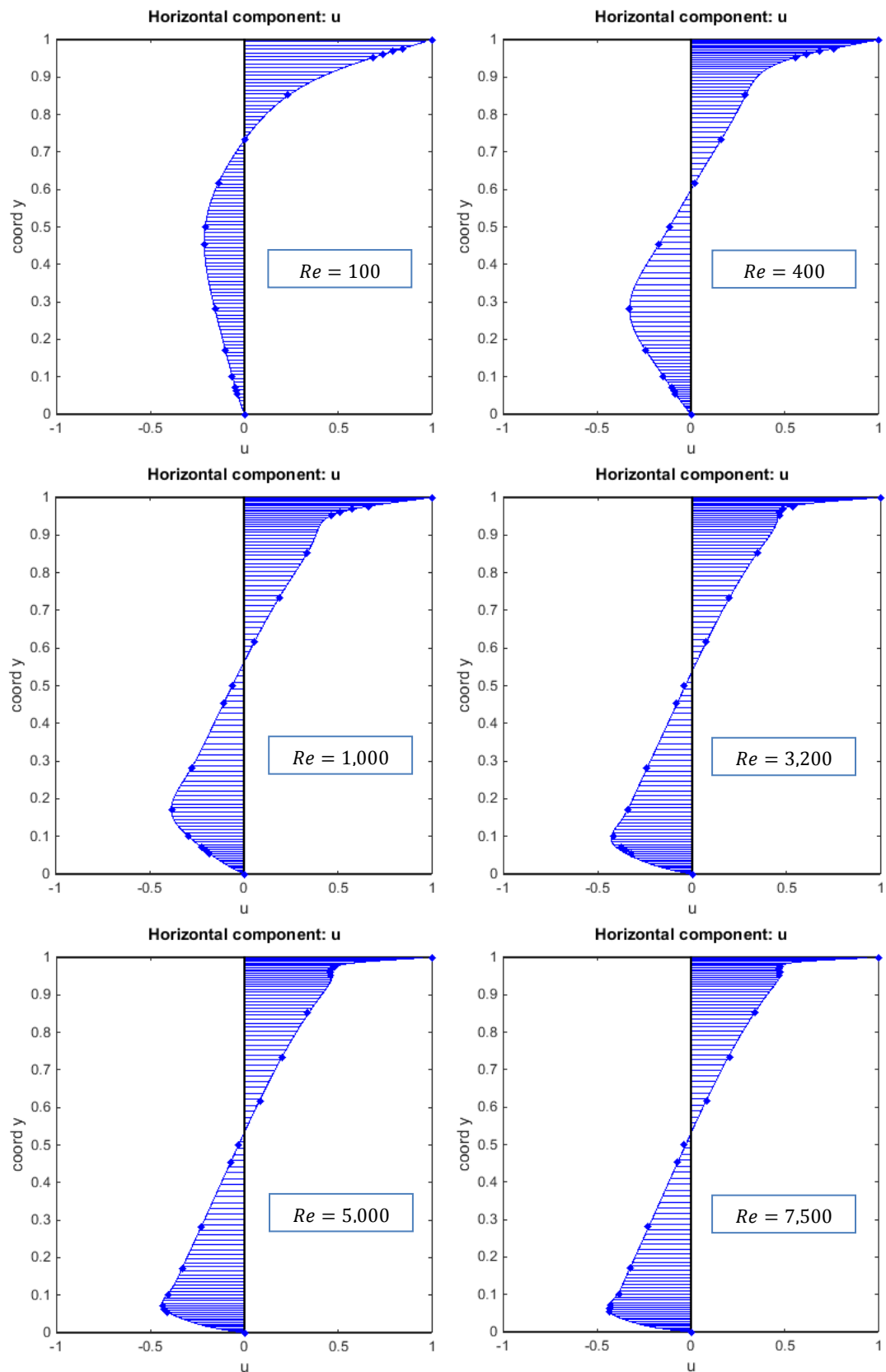
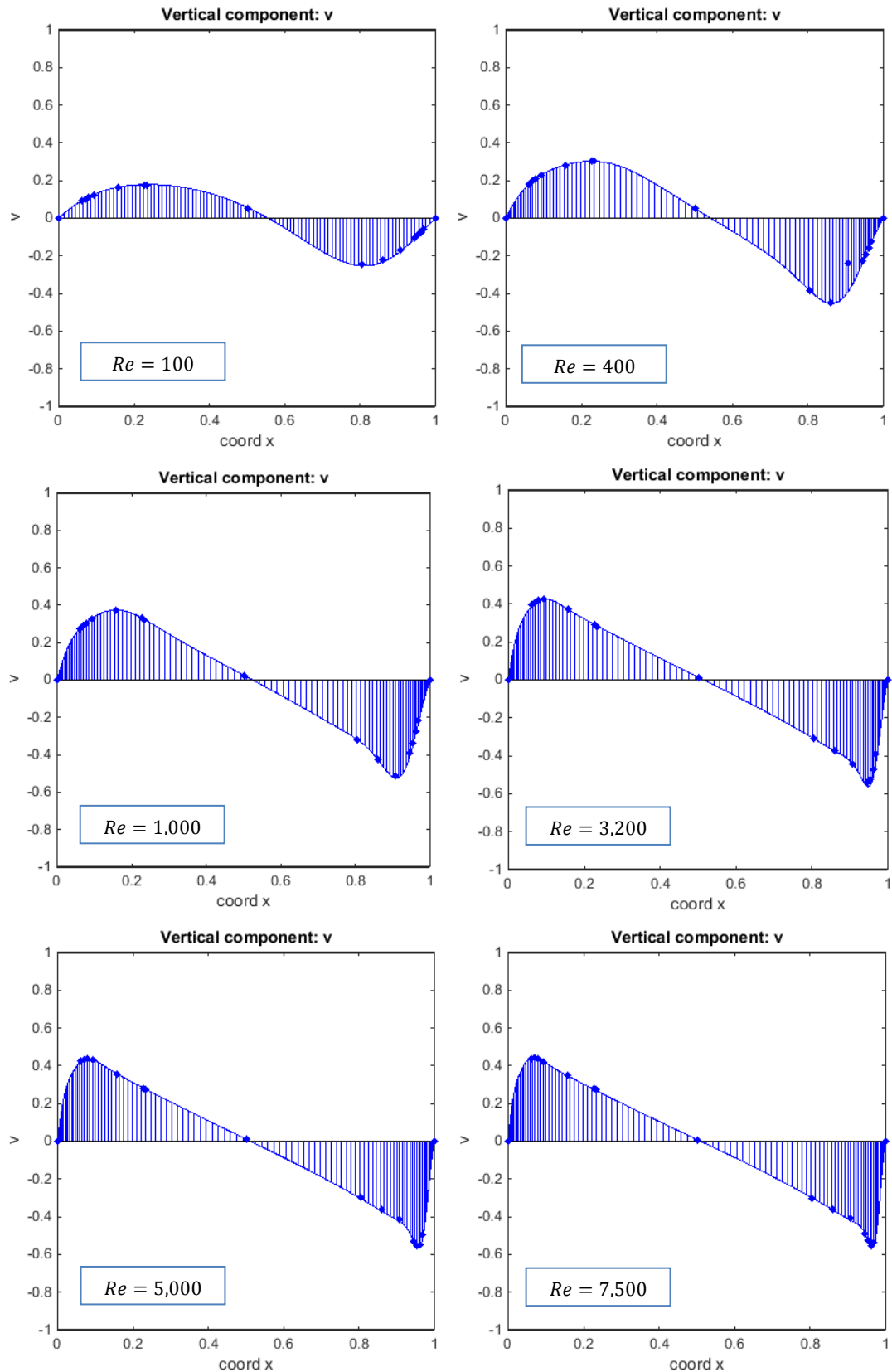


Figure 22: Comparison of horizontal component  $u$  with benchmark solution (blue dots) .



**Figure 23: Comparison of vertical component  $v$  with benchmark solution (blue dots).**

### 4.3.3 Code verification

As commented in different sections of this paper, it is very important to make sure that the obtained solution has the expected order of accuracy. Therefore, an analysis concerning the discretization of both the convective and diffusive terms in the momentum equation has been done. The process is similar to the one described in section 3.3.3.

Let  $\mathbf{v}$  be an arbitrary function. In this case, one may choose a combination of trigonometric functions such as:

$$\mathbf{v} = \begin{pmatrix} u \\ v \end{pmatrix} = \begin{pmatrix} A_u \sin(n_u \pi x) \sin(m_u \pi y) \\ A_v \sin(n_v \pi x) \sin(m_v \pi y) \end{pmatrix} \quad (4.38)$$

Then, diffusive terms and convective terms are computed analytically:

$$\begin{aligned} & (\mathbf{v} \cdot \nabla) \mathbf{v} \\ &= \begin{pmatrix} u A_u n_u \pi \cos(n_u \pi x) \sin(m_u \pi y) + v A_u m_u \pi \sin(n_u \pi x) \cos(m_u \pi y) \\ u A_v n_v \pi \cos(n_v \pi x) \sin(m_v \pi y) + v A_v m_v \pi \sin(n_v \pi x) \cos(m_v \pi y) \end{pmatrix} \end{aligned} \quad (4.39)$$

$$\nabla^2 \mathbf{v} = \begin{pmatrix} A_u \pi^2 (n_u^2 + m_u^2) \sin(n_u \pi x) \sin(m_u \pi y) \\ A_v \pi^2 (n_v^2 + m_v^2) \sin(n_v \pi x) \sin(m_v \pi y) \end{pmatrix} \quad (4.40)$$

Expressions 4.39 and 4.40 are evaluated at each node coordinates. Velocity is evaluated at each node too and the discrete convective (4.16) and diffusive terms (4.17) are computed. Both results are compared and the error is calculated as the major absolute difference between analytic and discrete values. This process is repeated for several mesh sizes and a plot is done to ensure that the error corresponds to the expected order of accuracy.

Something which must be taken into account when using velocity fields such as 4.38 is the fact that they are not incompressible. However, in the discretization of the convective term (4.16) it is assumed that  $(\mathbf{v} \cdot \nabla) \mathbf{v} = \nabla \cdot (\mathbf{v} \mathbf{v})$ . Then if no correction is done, the computed error would have no sense at all. Then, instead of using expression 4.39, one should compare the term  $\nabla \cdot (\mathbf{v} \mathbf{v})$ , that is indeed the term being approximated.

$$\begin{aligned} \nabla \cdot (\mathbf{v} \mathbf{v}) &= (\mathbf{v} \cdot \nabla) \mathbf{v} + \mathbf{v} (\nabla \cdot \mathbf{v}) \\ &= \begin{pmatrix} u A_u n_u \pi \cos(n_u \pi x) \sin(m_u \pi y) + v A_u m_u \pi \sin(n_u \pi x) \cos(m_u \pi y) \\ u A_v n_v \pi \cos(n_v \pi x) \sin(m_v \pi y) + v A_v m_v \pi \sin(n_v \pi x) \cos(m_v \pi y) \end{pmatrix} \\ &+ \begin{pmatrix} u A_u n_u \pi \cos(n_u \pi x) \sin(m_u \pi y) + u A_v m_v \pi \sin(n_v \pi x) \cos(m_v \pi y) \\ v A_u n_u \pi \cos(n_u \pi x) \sin(m_u \pi y) + v A_v m_v \pi \sin(n_v \pi x) \cos(m_v \pi y) \end{pmatrix} \end{aligned} \quad (4.41)$$

The following figure shows the error plot for  $A_u = A_v = 1.0$ ,  $n_u = 1.0$ ,  $m_u = 2.0$ ,  $n_v = 3.0$  and  $m_v = 4.0$ . The slope of the error is the expected, since it corresponds to a second order error. It is remarkable that for very coarse meshes ( $\Delta x = 0.2$ ), the error presents an anarchic behaviour. This is explained by the fact that it is not possible to reproduce a field constituted by trigonometric

functions whose smallest wavelength is 0,5 with such mesh resolution. The other aspect that may be of interest is the apparently high value of the error. This may be explained by the fact that such velocity field presents strong gradients and requires a very refined mesh to approximate it decently. As saw in the first chapter, when approximating a first derivative with a second order scheme, the error is proportional to the third derivative of the real function (see equation 1.26). Then the higher the gradients, the higher the error.

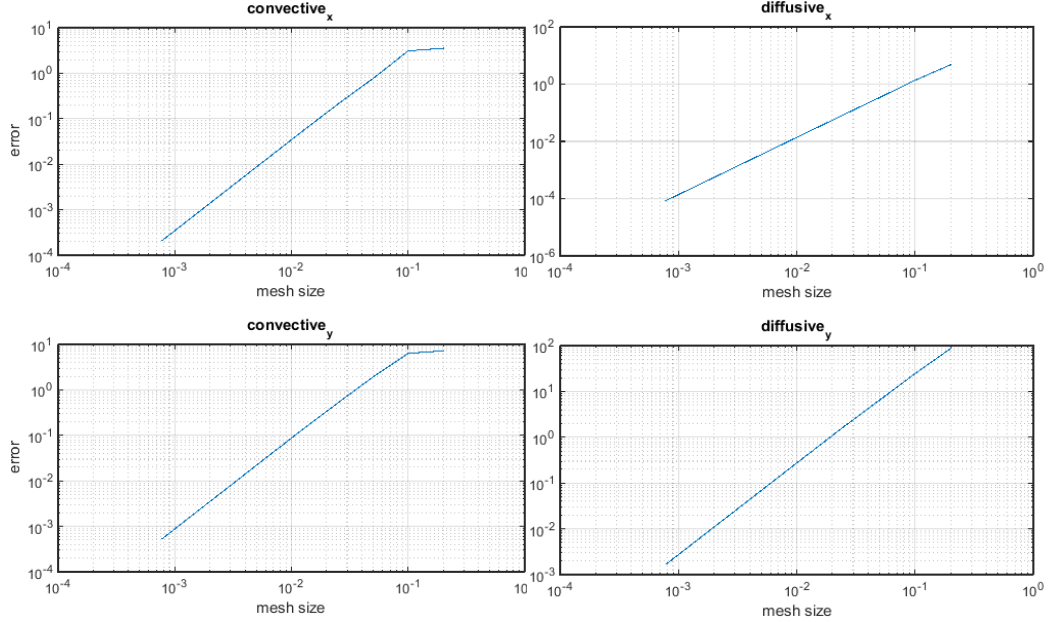


**Figure 24: Error plot for  $A_u = A_v = 1.0$ ,  $n_u = 1.0$ ,  $m_u = 2.0$ ,  $n_v = 3.0$  and  $m_v = 4.0$ .**

Next figure shows the same plot for  $A_u = A_v = 1.0$ ,  $n_u = 0.25$ ,  $m_u = 1.0$ ,  $n_v = 1.0$  and  $m_v = 0.5$ . It is seen how the error is substantially reduced and the chaotic behaviour of the error with coarser meshes is suppressed.

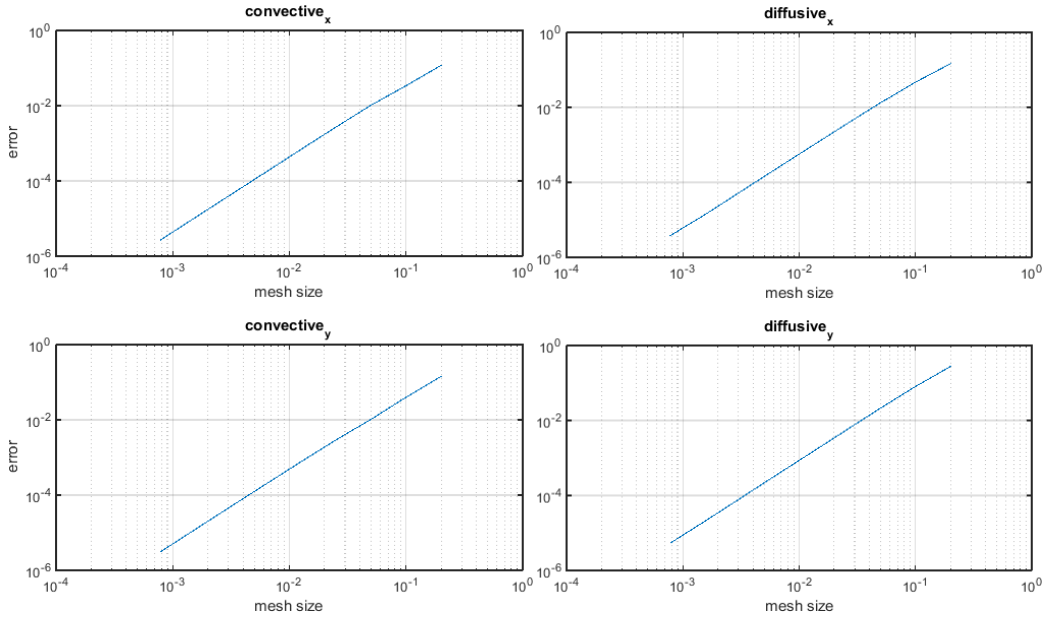


**Figure 25: Error plot for  $A_u = A_v = 1.0$ ,  $n_u = 0.25$ ,  $m_u = 1.0$ ,  $n_v = 1.0$  and  $m_v = 0.5$ .**

## 5 Differentially Heated Cavity

### 5.1 Definition of the problem

#### 5.1.1 General description

This problem consists of a fluid confined in a 2D square cavity with its lateral walls at different temperature and its upper and lower walls being adiabatic. The wall at the left side will remain at a higher temperature than the one at the right, thus leading the fluid to a clockwise rotation. Unlike in the Lid Driven Cavity problem, where the upper wall moves at a certain speed, in this case any of the walls moves, so velocity is equally prescribed in all the cavity boundary being both of its component null. A sketch of the problem may be seen in the figure below.

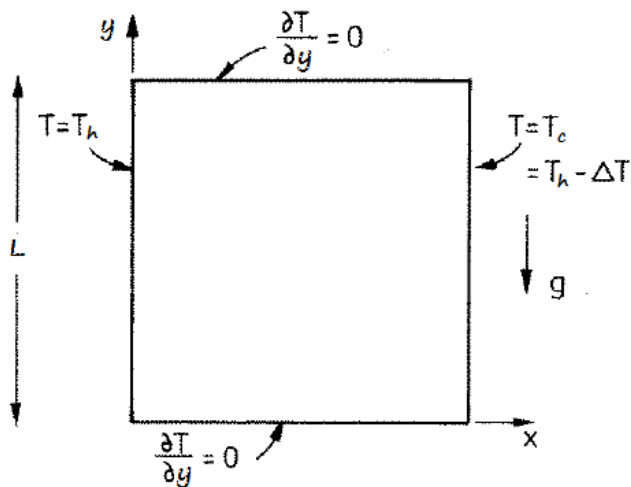


Figure 26: Sketch of the problem.

This is a case in which the source of the movement is the buoyancy term in the Navier-Stokes momentum equation. In such cases the Boussinesq approximation is applied. It basically consists in assuming that the variations in the fluid's density are neglected, thus leading to an incompressible flow, except in the volumetric forces, where these variations gain importance and are to be taken into account, since they are responsible for the fluid's movement.

### 5.1.2 Nomenclature

| Problem data                           | Numerical data  |
|--|---|
| $L$ : square cavity dimension          | $N$ : number of control volumes   |
| $T_h$ : temperature of the hot wall    | $N_x$ : number of CV in x-direction   |
| $T_c$ : temperature of the cold wall   | $N_y$ : number of CV in y-direction   |
| $\rho$ : density of the fluid          | $\Delta t$ : time step  |
| $c_p$ : specific heat coefficient      | $\Delta x$ : mesh horizontal size   |
| $\lambda$ : thermal conductivity       | $\Delta y$ : mesh vertical size   |
| $\mu$ : dynamic viscosity              | $\Delta x_d$ : horizontal nodal distance  |
| $g$ : acceleration due to gravity      | $\Delta y_d$ : vertical nodal distance  |
| $\beta$ : expansion coefficient        | $F$ : volumetric flux (i.e. $\int_{\partial\Omega}  \mathbf{v} \cdot d\mathbf{S} $ )              |
| $Pr$ : Prandtl number                  |   |
| $Ra$ : Rayleigh number                 |   |
| Problem variables                      | Subscripts  |
| $x$ : horizontal coordinate            | $\phi_n, \phi_s, \phi_e, \phi_w$ refer to the wall of the volume at which variables are evaluated |
| $y$ : vertical coordinate              | $\phi_N, \phi_S, \phi_E, \phi_W, \phi_P$ refer to the node at which variables are evaluated       |
| $\mathbf{r}$ : coordinates (vector)    |   |
| $u$ : horizontal velocity              |   |
| $v$ : vertical velocity                |   |
| $\mathbf{v}$ : velocity field (vector) |   |
| $\zeta$ : vorticity                    |   |
| $Nu$ : Nusselt number                  |   |
| $t$ : time                             |   |
| Superscripts                           |   |
|  | $\phi^{n+1}$ : current instant  |
|  | $\phi^n$ : previous instant   |
|  | $\phi^{n-1}$ : previous to previous instant   |

### 5.1.3 Governing equations

The equations that used in this problem are mass, momentum and energy conservation, assuming Newtonian fluid, incompressible flow and constant physical properties, read:

$$\nabla \cdot \mathbf{v} = 0 \quad (5.1a)$$

$$\rho \left( \frac{\partial \mathbf{v}}{\partial t} + (\mathbf{v} \cdot \nabla) \mathbf{v} \right) = -\nabla p + \mu \nabla^2 \mathbf{v} + \rho \mathbf{g} \quad (5.2a)$$

$$\rho c_p \left( \frac{\partial T}{\partial t} + (\mathbf{v} \cdot \nabla) T \right) = \lambda \nabla^2 T \quad (5.3a)$$

#### Boussinesq approximation

The Boussinesq approximation is very used in natural convection problems and it basically states that the density differences are small enough to be neglected, except where they appear multiplied by the acceleration due to gravity (also called the buoyancy term). This approximation is introduced in the equations by replacing the density in the buoyancy term by an expression which depends on

the temperature. This dependency is obtained by introducing the thermal expansion coefficient. This is:

$$\rho = \rho_0 - \beta(T - T_0), \quad \beta > 0 \quad (5.4)$$

So, the rest of the densities that appear in the equation will remain constant. Thus, equation 5.2a now reads:

$$\rho_0 \left( \frac{\partial \mathbf{v}}{\partial t} + (\mathbf{v} \cdot \nabla) \mathbf{v} \right) = -\nabla p + \mu \nabla^2 \mathbf{v} + \rho_0 \mathbf{g} - \beta(T - T_0) \mathbf{g} \quad (5.5)$$

### Non-dimensional equations

In order to provide general and scaled solutions it is convenient to convert the equations into non-dimensional expressions. The quantities which will be used to scale the variables of the problem are  $L$ ,  $\rho$ ,  $c_p$  and  $\lambda$ .

Thus, the non-dimensional variables are the following:

$$\tilde{\mathbf{r}} = \frac{\mathbf{r}}{L} \quad (5.6)$$

$$\tilde{\mathbf{v}} = \frac{\mathbf{v}}{\frac{\rho c_p L}{\lambda}} \quad (5.7)$$

$$\tilde{t} = \frac{t}{\frac{\rho c_p L^2}{\lambda}} \quad (5.8)$$

$$\tilde{p} = \frac{t}{\rho \left( \frac{c_p L}{\lambda} \right)^2} \quad (5.9)$$

$$\tilde{T} = \frac{T - T_c}{T_h - T_c} \quad (5.10)$$

Substituting the dimensional variables into 5.2a, 5.3a and 5.4a one obtains the following non-dimensional equations. The superscript  $(\sim)$  is omitted for the sake of simplicity. From this point on, it is assumed all the expressions and variables are non-dimensional.

Remark: constant terms in equation 5.5 are included in the pressure field, leading, thus, to an "abstract" pressure<sup>4</sup>, which will be called equally  $p$  for simplicity.

$$\nabla \cdot \mathbf{v} = 0 \quad (5.1b)$$

$$\frac{\partial \mathbf{v}}{\partial t} + (\mathbf{v} \cdot \nabla) \mathbf{v} = -\nabla p + Pr \nabla^2 \mathbf{v} + Pr Ra T \hat{\mathbf{u}}_g \quad (5.2b)$$

$$\frac{\partial T}{\partial t} + (\mathbf{v} \cdot \nabla) T = \nabla^2 T \quad (5.3b)$$

Where  $\hat{\mathbf{u}}_g$  is a unit vector indicating the direction of the acceleration due to gravity. One should also notice the appearance of two non-dimensional numbers. This leads to the conclusion that the non-dimensional solution of the problem depends solely on these two numbers, which in this problem are defined below:

$$Pr = \frac{c_p \mu}{\lambda} \quad (5.11)$$

$$Ra = \frac{g \beta}{\mu \frac{\lambda}{\rho c_p}} (T_h - T_c) L^3 \quad (5.12)$$

## 5.2 Numerical methods

### 5.2.1 Time-integration

In this problem one has to integrate with respect to time two different equations: momentum and energy conservation. In the first one, the same methodology used in the Lid Driven Cavity problem was followed. Energy equation may be solved by using an implicit or an explicit scheme.

#### Momentum equation

A term containing the convection, diffusive and flotation term is defined below. It differs from 4.8 because of the different problem parameters used to turn the equations into dimensionless expressions and the addition of the source term resulting from the Boussinesq approximation.

$$\mathbf{R}(\mathbf{v}) = -(\mathbf{v} \cdot \nabla) \mathbf{v} + Pr \nabla^2 \mathbf{v} + Pr Ra T \hat{\mathbf{u}}_g \quad (5.13)$$

---

<sup>4</sup> The resultant pressure would be the dynamic pressure only if the term  $\rho_0 \mathbf{g}$  was included. In such case the constant term  $\beta T_0 \mathbf{g}$  is also included, so the resultant field is not strictly the dynamic pressure.

The rest of the steps are analogous to the described in section 4.2.1. The main difference is found in the limitations on the time step. In this case, it has to satisfy the next two conditions below (CFL condition [14]):

$$\Delta t \leq \frac{C_{conv}}{\left(\frac{|u_i|}{\Delta x_i}\right)_{max}} \quad (5.14)$$

$$\Delta t \leq \frac{C_{visc}}{\left(\frac{Pr}{\Delta x_i^2}\right)_{max}} \quad (5.15)$$

Where  $C_{conv}$  and  $C_{visc}$  are constants that must be smaller than unity. It is recommended that these values were 0.35 and 0.2 respectively.

### Energy equation

As it has been said in previous lines, the energy equation may be solved using an implicit scheme as much as an explicit one. If an explicit scheme is to be used, a second order Adams-Bashforth approximation could be equally used. However, an implicit scheme has been used, as it avoids numerical instabilities and the execution time once the first temporal iterations have been done was found to be relatively short. So, integrating expression 5.3b with respect to time:

$$\begin{aligned} \int_{t^n}^{t^{n+1}} \frac{\partial T}{\partial t} dt &= T^{n+1} - T^n = \int_{t^n}^{t^{n+1}} (-(\boldsymbol{v} \cdot \nabla)T + \nabla^2 T) dt \approx \\ &\approx [-(\boldsymbol{v}^{n+1} \cdot \nabla)T^{n+1} + \nabla^2 T^{n+1}] \Delta t \end{aligned}$$

Then, integrated 5.3b equation reads:

$$\frac{T^{n+1} - T^n}{\Delta t} = -(\boldsymbol{v}^{n+1} \cdot \nabla)T^{n+1} + \nabla^2 T^{n+1} \quad (5.16)$$

It is obvious that the velocity at the current instant is needed in order to obtain the temperature distribution in the whole domain. Therefore, momentum equation must be solved in first place. Once the velocity field  $\boldsymbol{v}^{n+1}$  is obtained, one is able to solve the energy equation.

### 5.2.2 Spatial-integration

In this section the process through which the spatial continuous equations are turned into a discrete set of equations is presented.

### Momentum equation

Momentum equation's discretization follows the same procedure that the one described for the Lid Driven Cavity problem at section 4.2.2.

### Energy equation

In the next line equation 5.16 will be discretized. Integrating the whole expression over a certain control volume one gets:

$$\int_{\Omega} \frac{T^{n+1} - T^n}{\Delta t} d\Omega = - \int_{\Omega} (\mathbf{v}^{n+1} \cdot \nabla) T^{n+1} d\Omega + \int_{\Omega} \nabla^2 T^{n+1} d\Omega$$

For the sake of clarity the diverse terms will be developed separately

#### *Transient term*

$$\int_{\Omega} \frac{T^{n+1} - T^n}{\Delta t} d\Omega = \frac{T_p^{n+1} - T_p^n}{\Delta t} \Delta x \Delta y \quad (5.17)$$

#### *Convective term*

$$\begin{aligned} \int_{\Omega} \nabla \cdot (\mathbf{v}^{n+1} T^{n+1}) d\Omega &= \oint_{\partial\Omega} \mathbf{v}^{n+1} T^{n+1} \cdot \hat{\mathbf{n}} dS \approx \\ &\approx F_e^{n+1} T_e^{n+1} + F_n^{n+1} T_n^{n+1} - F_w^{n+1} T_w^{n+1} - F_s^{n+1} T_s^{n+1} \end{aligned} \quad (5.18)$$

#### *Diffusive term*

$$\begin{aligned} \int_{\Omega} \nabla \cdot (\nabla T^{n+1}) d\Omega &= \oint_{\partial\Omega} \nabla T^{n+1} \cdot \hat{\mathbf{n}} dS \approx \\ &\left( \frac{\partial T^{n+1}}{\partial x} \Big|_e - \frac{\partial T^{n+1}}{\partial x} \Big|_w \right) \Delta y + \left( \frac{\partial T^{n+1}}{\partial y} \Big|_n - \frac{\partial T^{n+1}}{\partial y} \Big|_s \right) \Delta x \approx \\ &\approx \left( \frac{T_E^{n+1} - T_p^{n+1}}{\Delta x_{d_e}} - \frac{T_p^{n+1} - T_W^{n+1}}{\Delta x_{d_w}} \right) \Delta y \\ &\quad + \left( \frac{T_N^{n+1} - T_p^{n+1}}{\Delta y_{d_n}} - \frac{T_p^{n+1} - T_S^{n+1}}{\Delta y_{d_s}} \right) \Delta x \end{aligned} \quad (5.19)$$

If the variables at the walls of the cell are computed using a CDS scheme, then a expression of the following form may be obtained for each of the control volumes.

$$a_P T_P^{n+1} + a_N T_N^{n+1} + a_S T_S^{n+1} + a_E T_E^{n+1} + a_W T_W^{n+1} = b_P \quad (5.20)$$

Where the coefficients are the following:

$$\begin{aligned} a_P = & \frac{\Delta x \Delta y}{\Delta t} + \frac{\Delta y}{\Delta x_{d_e}} + \frac{\Delta x}{\Delta y_{d_n}} + \frac{\Delta y}{\Delta x_{d_w}} + \frac{\Delta x}{\Delta y_{d_s}} + \frac{F_e^{n+1}}{2} + \frac{F_n^{n+1}}{2} - \frac{F_w^{n+1}}{2} \\ & - \frac{F_s^{n+1}}{2} \end{aligned} \quad (5.21)$$

$$a_N = -\frac{\Delta x}{\Delta y_{d_n}} + \frac{F_n^{n+1}}{2} \quad (5.22)$$

$$a_S = -\frac{\Delta x}{\Delta y_{d_s}} - \frac{F_s^{n+1}}{2} \quad (5.23)$$

$$a_E = -\frac{\Delta y}{\Delta x_{d_e}} + \frac{F_e^{n+1}}{2} \quad (5.24)$$

$$a_W = -\frac{\Delta y}{\Delta x_{d_w}} - \frac{F_w^{n+1}}{2} \quad (5.25)$$

$$b_P = \frac{T_P^n \Delta x \Delta y}{\Delta t} \quad (5.26)$$

These are the coefficients for a generic control volume. Those in contact with the domain's boundary must be slightly modified. In the case of the upper or lower walls of the cavity, where the walls are adiabatic, the condition is then:

$$\frac{\partial T}{\partial y} = 0 \quad (5.27)$$

This affects the coefficients in the following way:

$$a'_P = a_P + a_N , \quad a'_N = 0 \quad (\text{if north side}) \quad (5.28)$$

$$a'_P = a_P + a_S , \quad a'_S = 0 \quad (\text{if south side}) \quad (5.29)$$

The volumes in contact with the left and the right walls, where temperature is prescribed, suffer different changes in its coefficients:

$$b'_P = b_P - a_E T_c , \quad a'_E = 0 \quad (\text{if east side}) \quad (5.30)$$

$$b'_P = b_P - a_W T_h , \quad a'_W = 0 \quad (\text{if west side}) \quad (5.31)$$

### 5.3 Results and discussion

The results presented in this section correspond to air or a fluid with similar physical properties, since the Prandtl number has been set to 0.71. Four different Rayleigh numbers have been considered.

| <b>Ra</b>             | <b>N<sub>x</sub></b> | <b>γ<sub>x</sub></b> | <b>N<sub>y</sub></b> | <b>γ<sub>y</sub></b> | <b>N</b> | <b>order</b>    |
|-----------------------|----------------------|----------------------|----------------------|----------------------|----------|-----------------|
| <b>10<sup>3</sup></b> | 100                  | 0.0<br>(uniform)     | 100                  | 0.0<br>(uniform)     | 10K      | 2 <sup>nd</sup> |
| <b>10<sup>4</sup></b> | 100                  | 0.0<br>(uniform)     | 100                  | 0.0<br>(uniform)     | 10K      | 2 <sup>nd</sup> |
| <b>10<sup>5</sup></b> | 100                  | 0.0<br>(uniform)     | 100                  | 0.0<br>(uniform)     | 10K      | 2 <sup>nd</sup> |
| <b>10<sup>6</sup></b> | 100                  | 0.0<br>(uniform)     | 100                  | 0.0<br>(uniform)     | 10K      | 2 <sup>nd</sup> |

**Table 7: Differentially Heated Cavity problem simulation parameters.**

### 5.3.1 Contour plots

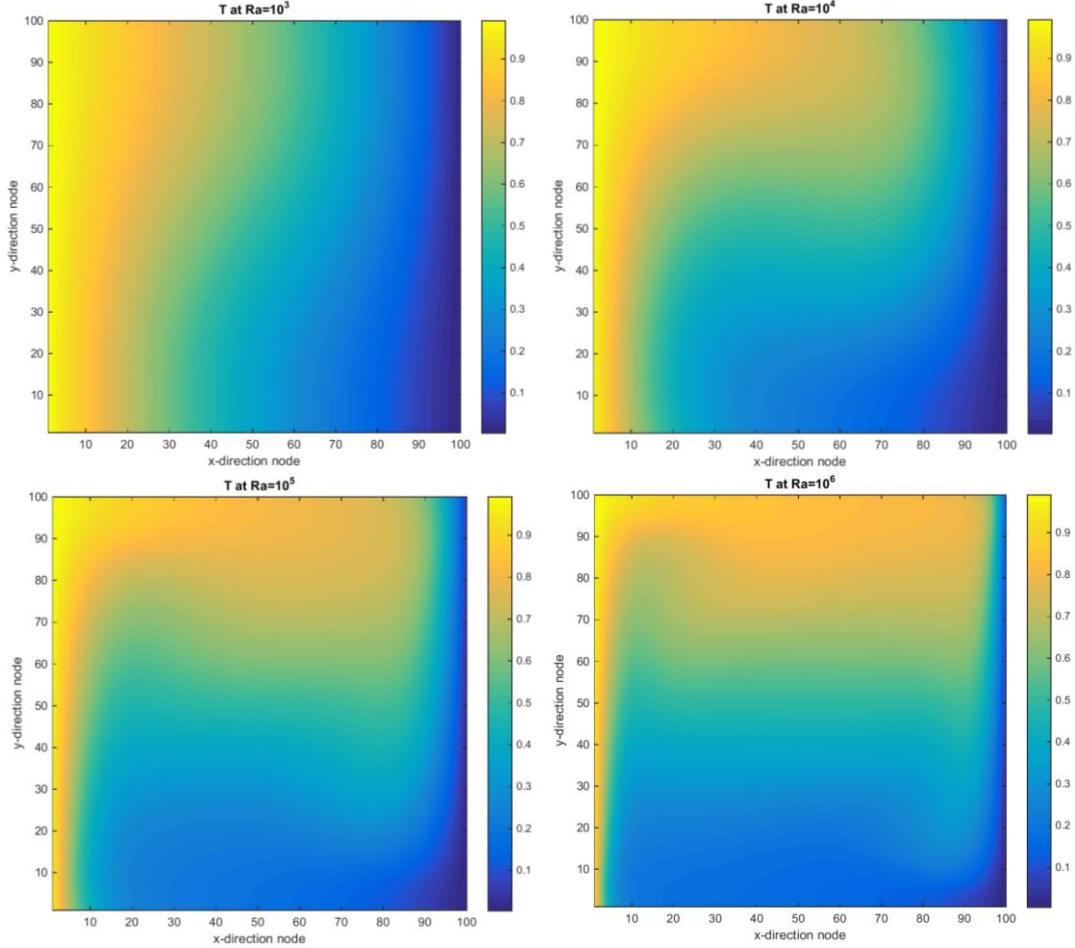
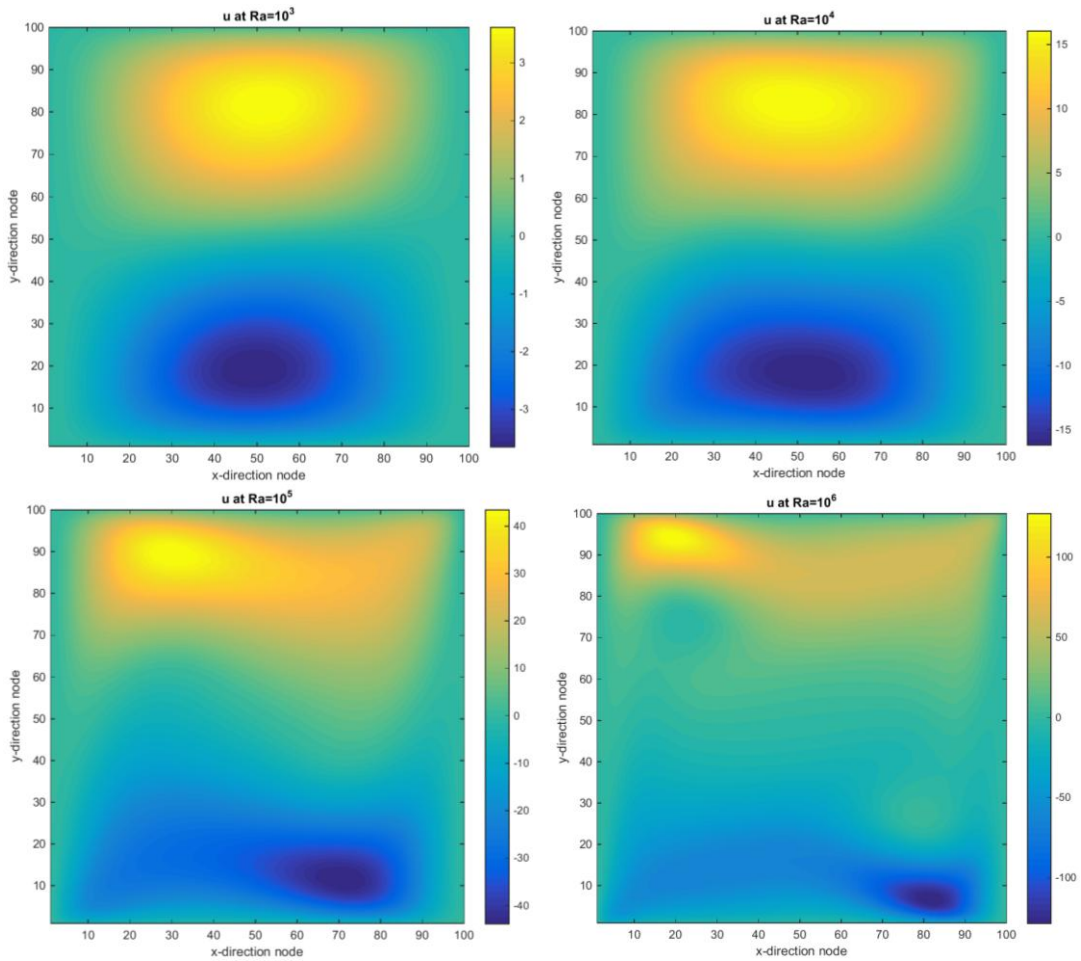


Figure 27: Temperature contour plots for different  $Ra$ .

Temperature contour plots above clearly show the  $Ra$  number influence on the steady state temperature field: for low values of  $Ra$  temperature field is stratified, increasing almost linearly from the hot wall at the left to the cold one. As  $Ra$  is incremented, convection gains importance and forces the fluid to rotate clockwise: Fluid in contact or near the left wall heats up and consequently decreases its density, causing its upward movement, while the fluid near the right-hand wall is cooled and thus increasing its density and going down.

The fluid's recirculation becomes stronger and the mixing of the fluid is more effective. At  $Ra = 10^6$  temperature is transported mainly because of convection, leaving air with not enough time for thermal conduction.



**Figure 28: Horizontal velocity component  $u$  contour plots for different  $Ra$ .**

Horizontal velocity agrees with the clockwise motion of the fluid. At lower values of  $Ra$ , the areas of maximum velocity are located at the centre of the cavity. Increasing the Rayleigh number leads to an increase in the velocity magnitude as well as the maxima of velocity move towards the corners.

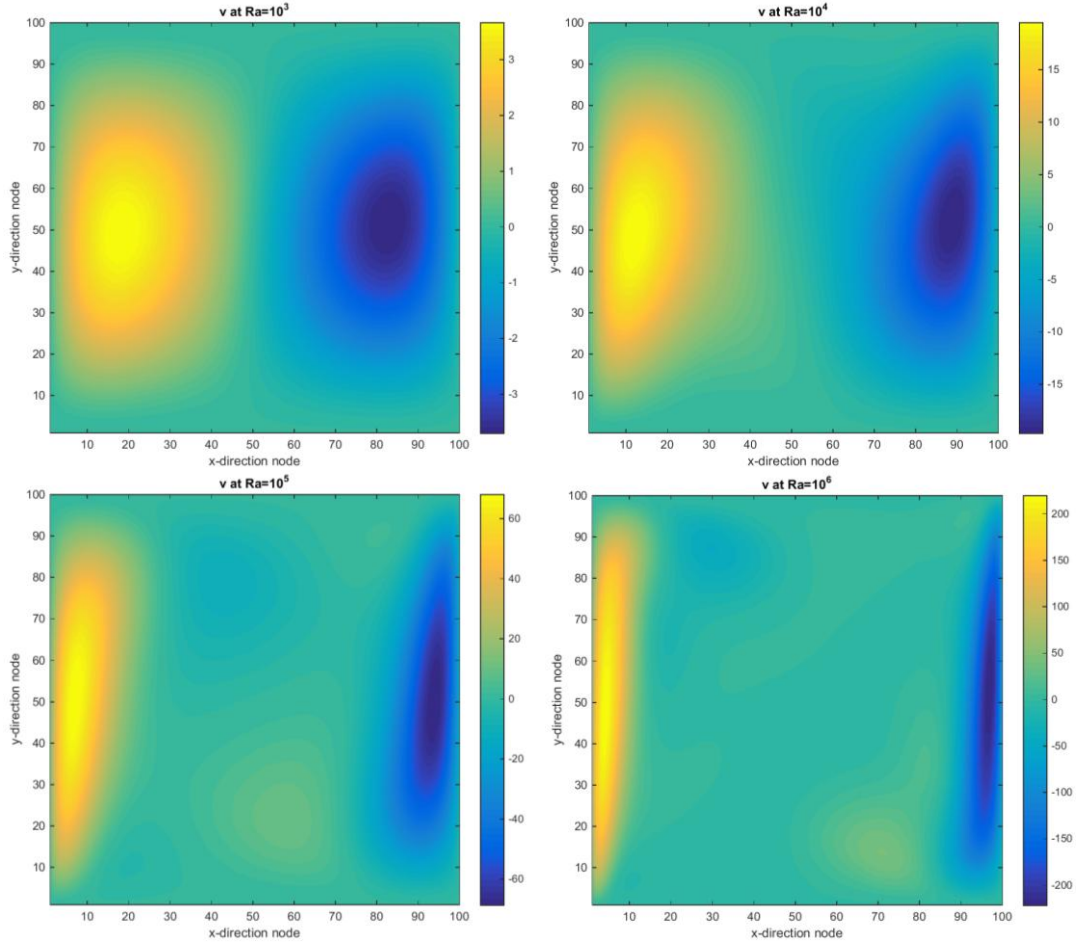


**Figure 29: Vertical velocity component  $v$  contour plots for different  $Ra$ .**

The tendency of the vertical component of the velocity is very similar to the one concerning horizontal velocity. Positive values (upwards motion) are located at the left wall while negative values (downwards motion) are located at the right wall of the cavity. Here, the main effect of  $Ra$  increase is the stretching of the areas where velocity is higher, leading to high velocity gradients at the wall proximities. One observes as the centre zone of the cavity has no important vertical movement, similarly to horizontal velocity.

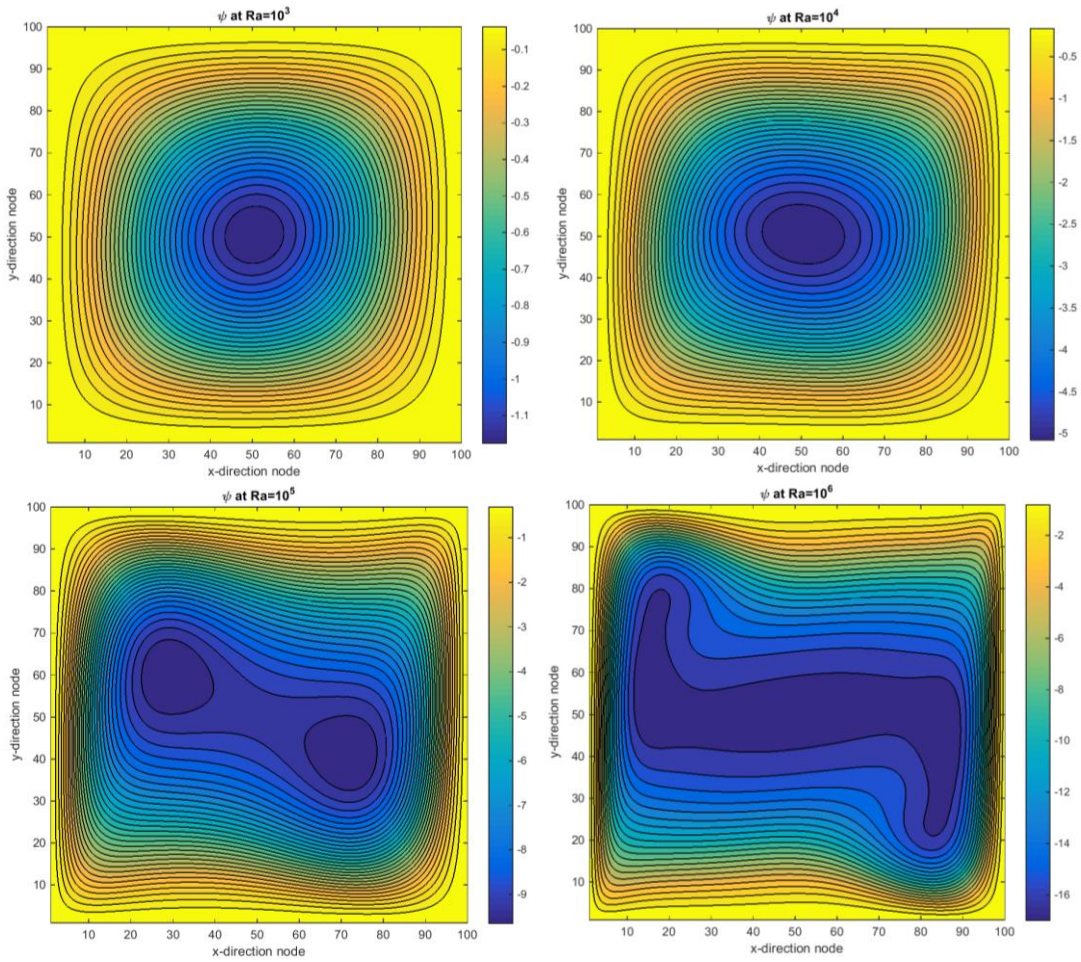


**Figure 30: Stream function  $\psi$  contour plots for different  $Ra$**

Streamlines perfectly represent the clockwise rotation of the fluid inside the cavity. For the first two values of  $Ra$  the fluid movement is very similar, though in the second case being it faster. For the third case, the main rotation vortex is divided into two. For the highest Rayleigh value the streamlines take a Z-like shape. The fluid is heated up fast and gains such vertical velocities that it makes it difficult for the fluid to follow the rotation appropriately.

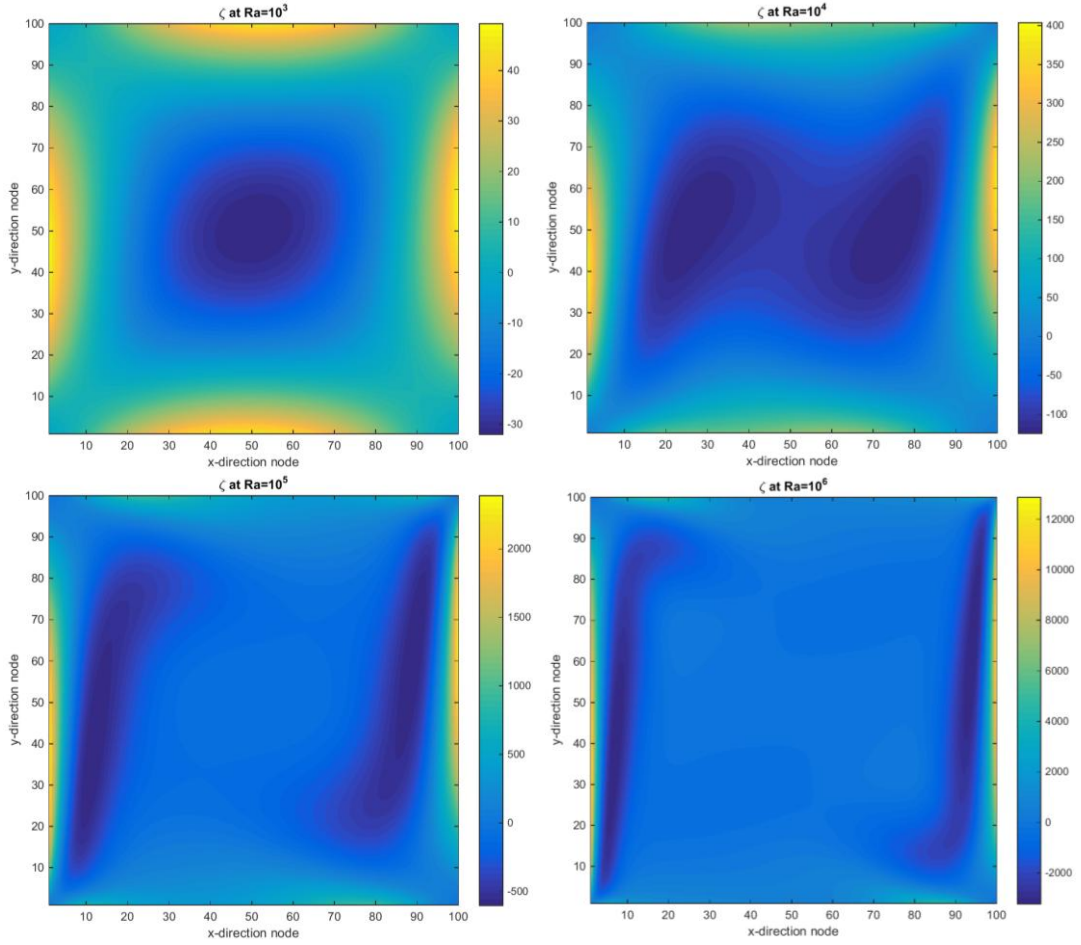


**Figure 31: Vorticity  $\zeta$  contour plots for different  $Ra$ .**

Figure above shows the contour plots of vorticity. This variable measures the local spinning motion of the fluid. It is defined:

$$\zeta = \nabla \times \mathbf{v} = \left( \frac{\partial u}{\partial y} - \frac{\partial v}{\partial x} \right) \hat{k} \quad (5.32)$$

Negative values of such variable (dark blue) indicate clockwise rotation while positive values (yellow) indicate counter clockwise rotations. In the first plot the central area presents negative vorticity, due to the global rotation of the fluid, while in the walls one observe wide areas coloured with yellow. Positive vorticity appearance at these regions is caused by the strong boundary layer that is created.

As  $Ra$  increases, this central region of negative vorticity is split in two areas which tend to get closer to the lateral walls while stretching and elongating.

### 5.3.2 Comparison with benchmark solution

In the table below some salient features of the flow are presented and compared to the benchmark solutions provided in [17]. These results are, in order of appearance:

- Stream function at the mid-point of the cavity
- Maximum absolute value of the stream function and its location.
- Maximum horizontal velocity on the vertical mid-plane of the cavity and its location.
- Maximum vertical velocity on the horizontal mid-plane of the cavity and its location.
- Average Nusselt number throughout the cavity.
- Average Nusselt number on the vertical mid-plane of the cavity.
- Average Nusselt number on the vertical boundary of the cavity (at  $x = 0$ ).
- Maximum value of the local Nusselt number on the boundary at  $x = 0$  and its location.
- Minimum value of the local Nusselt number on the boundary at  $x = 0$  and its location.

Local Nusselt number is defined below:

$$Nu(x, y) = uT - \frac{\partial T}{\partial x} \quad (5.32)$$

|                | <i>Ra</i> |         |        |         |        |         |        |         |
|----------------|-----------|---------|--------|---------|--------|---------|--------|---------|
|                | $10^3$    |         | $10^4$ |         | $10^5$ |         | $10^6$ |         |
|                | Bench     | Results | Bench  | Results | Bench  | Results | Bench  | Results |
| $ \psi _{mid}$ | 1.174     | 1.176   | 5.071  | 5.077   | 9.111  | 9.146   | 16.320 | 16.570  |
| $ \psi _{max}$ | -         | -       | -      | -       | 9.612  | 9.648   | 16.750 | 16.991  |
| $x$            | -         | -       | -      | -       | 0.285  | 0.715   | 0.151  | 0.855   |
| $y$            | -         | -       | -      | -       | 0.601  | 0.395   | 0.547  | 0.455   |
| $u_{max}$      | 3.649     | 3.650   | 16.178 | 16.182  | 34.73  | 34.768  | 64.63  | 65.055  |
| $y$            | 0.813     | 0.820   | 0.823  | 0.830   | 0.855  | 0.860   | 0.850  | 0.860   |
| $v_{max}$      | 3.697     | 3.698   | 19.617 | 19.621  | 68.59  | 68.696  | 219.36 | 220.934 |
| $x$            | 0.178     | 0.180   | 0.119  | 0.120   | 0.066  | 0.070   | 0.0379 | 0.040   |
| $\bar{Nu}$     | 1.118     | 1.118   | 2.243  | 2.247   | 4.519  | 4.538   | 8.800  | 8.926   |
| $Nu_{1/2}$     | 1.118     | 1.118   | 2.243  | 2.247   | 4.519  | 4.538   | 8.799  | 8.926   |
| $Nu_0$         | 1.117     | 1.118   | 2.238  | 2.247   | 4.509  | 4.538   | 8.817  | 8.926   |
| $Nu_{max}$     | 1.505     | 1.507   | 3.528  | 3.539   | 7.717  | 7.797   | 17.925 | 18.324  |
| $y$            | 0.092     | 0.085   | 0.143  | 0.145   | 0.081  | 0.075   | 0.0378 | 0.035   |

|            |       |       |       |       |       |       |       |       |
|------------|-------|-------|-------|-------|-------|-------|-------|-------|
| $Nu_{min}$ | 0.692 | 0.691 | 0.586 | 0.585 | 0.729 | 0.727 | 0.989 | 0.974 |
| $y$        | 1.000 | 0.995 | 1.000 | 0.995 | 1.000 | 0.995 | 1.000 | 0.995 |

Table 8: Comparison between the obtained results and the benchmark solution.

In general, results obtained are similar to those given in [17]. For the first two values of Rayleigh number, the maximum absolute value of the stream function are located at the centre of the cavity (this is the reason why no values are shown in the table). In the following next two values of  $Ra$ , the location of these maxima seem to be utterly mistaken. Nevertheless, these points are symmetric to those given in the benchmark solution with respect to the plane  $y = x$ . As one may observe, this symmetry characterises all the solutions to the problem, so the error may be computed with the corresponding symmetric points.

The most significant errors are found in the locations of the presented features. These discrepancies seem fair, since for the benchmark solution coarser meshes were used and then the results were interpolated, while in the results given in this paper are computed with a uniform mesh of  $100 \times 100$ , where no interpolations were performed. Leaving aside the errors concerning the coordinates of the compared values, these latter present a maximum error of 2.226% for the highest value of  $Ra$ , which is within the reasonable and justifiable margin of error.

|                | $Ra$   |        |        |        |
|----------------|--------|--------|--------|--------|
|                | $10^3$ | $10^4$ | $10^5$ | $10^6$ |
| $ \psi _{mid}$ | 0.170  | 0.118  | 0.384  | 1.532  |
| $ \psi _{max}$ | -      | -      | 0.375  | 1.439  |
| $x$            | -      | -      | 0.000  | 3.974  |
| $y$            | -      | -      | 0.666  | 0.366  |
| $u_{max}$      | 0.027  | 0.025  | 0.109  | 0.658  |
| $y$            | 0.861  | 0.851  | 0.585  | 1.176  |
| $v_{max}$      | 0.027  | 0.020  | 0.155  | 0.718  |
| $x$            | 1.124  | 0.840  | 6.061  | 5.541  |
| $\bar{Nu}$     | 0.000  | 0.178  | 0.420  | 1.432  |
| $Nu_{1/2}$     | 0.000  | 0.178  | 0.420  | 1.443  |
| $Nu_0$         | 0.090  | 0.402  | 0.643  | 1.236  |
| $Nu_{max}$     | 0.133  | 0.312  | 1.037  | 2.226  |
| $y$            | 7.609  | 1.399  | 7.407  | 7.407  |
| $Nu_{min}$     | 0.145  | 0.171  | 0.274  | 1.517  |
| $y$            | 0.500  | 0.500  | 0.500  | 0.500  |

Table 9: Relative error (%) of the obtained results with respect to benchmark values.

## 6 Burgers' equation

### 6.1 Definition of the problem

#### 6.1.1 General description

The Burgers' equation is a fundamental partial differential equation from fluid dynamics. Despite its simplicity (it is a one dimensional equation) and the fact that it does not represent any real problem, it serves the purpose of approaching the turbulence phenomena, as well as illustrating some of the aspects of the 3D Navier-Stokes equations.

In this chapter, this equation is solved by transforming the equation and the variables into Fourier space, this is, solving the equation by means of a spectral method. This is very useful, as it will clarify the role of the different scales which take part in the turbulence phenomenon.

#### 6.1.2 Nomenclature

| Problem data                                | Numerical data                              |
|---|---|
| $L$ : domain dimension                      | $N$ : number of modes                       |
| $\rho$ : density of the fluid               | $k, p, q$ : mode indices                    |
| $\mu$ : dynamic viscosity                   | $\Delta t$ : time step                      |
| $f$ : source term                           | $\nu_t$ : turbulent viscosity               |
| $L^*$ : characteristic length               | $\nu_t^*$ : non-dimensional eddy-viscosity  |
| $u^*$ : characteristic velocity             | $m$ : energy spectrum slope                 |
| $Re$ : Reynolds number                      | $C_k$ : Kolmogorov constant                 |
| Problem variables                           | Subscripts                                  |
| $x$ : coordinate                            | $\phi_k, \phi_p, \phi_q$ refer to the mode  |
| $u$ : velocity                              |   |
| $\hat{u}$ : velocity Fourier's coefficients |   |
| $E$ : energy                                |   |
| $t$ : time                                  |   |
|   | Superscripts                                |
|   | $\phi^{n+1}$ : current instant              |
|   | $\phi^n$ : previous instant                 |
|   | $\phi^{n-1}$ : previous to previous instant |
|   | $\bar{\phi}$ : complex conjugate            |

#### 6.1.3 Governing equations

Considering the one dimensional Navier-Stokes equation without the pressure gradient term

$$\rho \left[ \frac{\partial u}{\partial t} + u \frac{\partial u}{\partial x} \right] = \mu \frac{\partial^2 u}{\partial x^2} + f \quad (6.1)$$

With

$$x \in [0, L] ; \quad u(0) = u(L) \quad (6.2)$$

And converting it to a non-dimensional expression by means of the following dimensionless variables (denoted with superscript  $\tilde{\phi}$ )

$$\tilde{x} = \frac{x}{L^*} \quad (6.3)$$

$$\tilde{u} = \frac{u}{u^*} \quad (6.4)$$

$$\tilde{t} = \frac{t}{\frac{L^*}{u^*}} \quad (6.5)$$

By substituting these variables into 6.1 one gets

$$\frac{\partial \tilde{u}}{\partial \tilde{t}} + \tilde{u} \frac{\partial \tilde{u}}{\partial \tilde{x}} = \frac{\mu}{\rho u^* L^*} \frac{\partial^2 \tilde{u}}{\partial \tilde{x}^2} + \tilde{f} \quad (6.6)$$

Where  $U^*$  and  $L^*$  are the characteristic velocity and longitude of the problem respectively. Defining

$$Re = \frac{\rho u^* L^*}{\mu} \quad (6.7)$$

And abandoning the use of the superscript  $\tilde{\phi}$  to denote dimensionless variables (from this point on, it is assumed that all the variables are non-dimensional) one obtains the Burgers' equation:

$$\frac{\partial u}{\partial t} + u \frac{\partial u}{\partial x} = \frac{1}{Re} \frac{\partial^2 u}{\partial x^2} + f \quad (6.8)$$

As stated in previous lines, it is a simplified model that shares many of the aspects of the 3D Navier-Stokes equations.

### Burgers' equation in Fourier space

In order to transform the problem into Fourier space, one may define variable  $u$  as follows.

$$u(x, t) = \sum_{k=-\infty}^{k=+\infty} \hat{u}_k e^{ikx} ; \quad \hat{u}_k \in \mathbb{C} \quad (6.9)$$

This definition is correct if the characteristic length used to turn the equation into non-dimensional expression is the following

$$L^* = \frac{L}{2\pi} \quad (6.10)$$

Where  $L$  is the dimension of the domain. If 6.10 is not accomplished, then the periodic boundary conditions cannot be satisfied.

By direct substitution into the original equation one obtains:

*Transient term*

$$\frac{\partial u}{\partial t} = \frac{\partial}{\partial t} \left( \sum_{k=-\infty}^{k=+\infty} \hat{\mathbf{u}}_k e^{ikx} \right) = \sum_{k=-\infty}^{k=+\infty} \frac{\partial \hat{\mathbf{u}}_k}{\partial t} e^{ikx} \quad (6.11)$$

*Convective term*

$$\begin{aligned} u \frac{\partial u}{\partial x} &= \left( \sum_{p=-\infty}^{p=+\infty} \hat{\mathbf{u}}_p e^{ipx} \right) \frac{\partial}{\partial x} \left( \sum_{q=-\infty}^{q=+\infty} \hat{\mathbf{u}}_q e^{iqx} \right) = \\ &\left( \sum_{p=-\infty}^{p=+\infty} \hat{\mathbf{u}}_p e^{ipx} \right) \left( \sum_{q=-\infty}^{q=+\infty} iq \hat{\mathbf{u}}_q e^{iqx} \right) = \sum_{p=-\infty}^{p=+\infty} \sum_{q=-\infty}^{q=+\infty} \hat{\mathbf{u}}_p iq \hat{\mathbf{u}}_q e^{i(q+p)x} \end{aligned} \quad (6.12)$$

*Diffusive term*

$$\frac{\partial^2 u}{\partial x^2} = \frac{\partial^2}{\partial x^2} \left( \sum_{k=-\infty}^{k=+\infty} \hat{\mathbf{u}}_k e^{ikx} \right) = - \sum_{k=-\infty}^{k=+\infty} k^2 \hat{\mathbf{u}}_k e^{ikx} \quad (6.13)$$

So, equation 6.8 in Fourier space reads:

$$\begin{aligned} &\sum_{k=-\infty}^{k=+\infty} \frac{\partial \hat{\mathbf{u}}_k}{\partial t} e^{ikx} + \sum_{p=-\infty}^{p=+\infty} \sum_{q=-\infty}^{q=+\infty} \hat{\mathbf{u}}_p iq \hat{\mathbf{u}}_q e^{i(q+p)x} = \\ &= -\frac{1}{Re} \sum_{k=-\infty}^{k=+\infty} k^2 \hat{\mathbf{u}}_k e^{ikx} + \sum_{k=-\infty}^{k=+\infty} \hat{\mathbf{f}}_k e^{ikx} \end{aligned} \quad (6.14)$$

Which can be solved for each mode  $k$

$$\frac{\partial \hat{\mathbf{u}}_k}{\partial t} + \sum_{p+q=k} \hat{\mathbf{u}}_p iq \hat{\mathbf{u}}_q = -\frac{1}{Re} k^2 \hat{\mathbf{u}}_k + \hat{\mathbf{f}}_k \quad (6.15)$$

In this expression one is able to foresee the role of the convective term. For each mode it forces the involvement of a wide range of other modes. In some way, it mixes the different scales of the problem.

The proposed initial conditions are:

$$\hat{\mathbf{u}}_{k_0} = \frac{1}{|k|} \quad (6.16)$$

Provided that mode  $k = 0$  has no interactions with other modes, one may assume no mean flow, this is:

$$\hat{\mathbf{u}}_0 = 0 \quad (6.17)$$

The energy of each mode is computed as follows

$$E_k = \mathbf{u}_k \overline{\mathbf{u}_k} \in \mathbb{R} \quad (6.18)$$

### Large-Eddy Simulation

Since obtaining good results with Direct Numerical Simulation (DNS) has high computational costs, one may implement a Large-Eddy Simulation (LES) model, which should improve the results for coarser meshes. Though Smagorinsky model may be used, when solving the equation by means of a spectral method it cannot be used. Instead an spectral eddy-viscosity model is used. It consists basically in the addition of a non-dimensional viscosity multiplying the diffusive term, which is determined assuming some properties of the energy spectrum. This additional (turbulent) viscosity is computed as follows:

$$\nu_t = \nu_t^{+\infty} \left( \frac{E_{k_N}}{k_N} \right)^{1/2} \nu_t^* \quad (6.19)$$

$$\nu_t^{+\infty} = 0.31 \frac{5-m}{m+1} \sqrt{3-m} C_k^{-3/2} \quad (6.20)$$

$$\nu_t^* = 1 + 34.5 e^{-3.03(\frac{k_N}{k})} \quad (6.21)$$

Where  $m$  is the slope of the energy spectrum,  $E_{k_N}$  is the energy at the cut-off frequency ( $k_N$ ) and  $C_k$  is the Kolmogorov constant. In the case of the Burgers' equation  $m \approx 2$  and  $C_k \approx 0.4223$ . So, the equation for each mode that has to be solved using a LES model is:

$$\frac{\partial \hat{\mathbf{u}}_k}{\partial t} + \sum_{p+q=k} \hat{\mathbf{u}}_p i q \hat{\mathbf{u}}_q = - \left( \frac{1}{Re} + \nu_t k \right) k^2 \hat{\mathbf{u}}_k + \hat{\mathbf{f}}_k \quad (6.22)$$

## 6.2 Numerical methods

### 6.2.1 Time-integration

In this problem, it will be used an explicit scheme for the integration with respect to time. A second order Adams-Bashforth approximation may be used.

Defining:

$$\mathbf{R}_k(\mathbf{u}_k) = - \sum_{p+q=k} \hat{\mathbf{u}}_p i q \hat{\mathbf{u}}_q - k^2 \hat{\mathbf{u}}_k + \hat{\mathbf{f}}_k \quad (6.23)$$

One finally obtains the following time-integrated expression:

$$\frac{\mathbf{u}_k^{n+1} - \mathbf{u}_k^n}{\Delta t} = \frac{3}{2} \mathbf{R}_k(\mathbf{u}_k^n) - \frac{1}{2} \mathbf{R}_k(\mathbf{u}_k^{n-1}) \quad (6.24)$$

Time step must be determined by a CFL-like condition:

$$\Delta t \leq C \frac{Re}{N^2} \quad (6.25)$$

### 6.2.2 Spatial approximation

The spatial discretization of equation 6.14 is very simple. As expression 6.9 shows, the Fourier transform is a series consisting of infinite terms. In this case, the discretization is based on the truncation of this series up to a finite amount of terms. This is:

$$u(x, t) = \sum_{k=-\infty}^{k=+\infty} \hat{\mathbf{u}}_k e^{ikx} \approx \sum_{k=-N}^{k=+N} \hat{\mathbf{u}}_k e^{ikx} \quad (6.26)$$

This reduces the infinite set of equations that would result of an infinite series to a set of  $2N + 1$  equations. This number may be even reduced again taking into account assumption 6.17 and the fact that the solution to this problem has conjugate symmetry:

$$\hat{\mathbf{u}}_k = \overline{\hat{\mathbf{u}}_{-k}} \quad (6.27a)$$

Or alternatively written:

$$\begin{aligned} Re(\hat{\mathbf{u}}_k) &= Re(\hat{\mathbf{u}}_{-k}) \\ Im(\hat{\mathbf{u}}_k) &= -Im(\hat{\mathbf{u}}_{-k}) \end{aligned} \quad (6.27b)$$

This comes from the fact that  $u(x, t)$  is a real function and the Fourier transform of any real function satisfies this condition. Therefore, one may solve the problem for the positive values of  $k$ , for instance, and then obtain the values associated to negative modes by means of 6.27. Below, the fact that conjugate symmetry is characteristic of real functions is proved:

$$\begin{aligned}
 u &= \sum_{k=1}^{k=+\infty} \widehat{\mathbf{u}}_k e^{ikx} + \sum_{k=-\infty}^{k=-1} \widehat{\mathbf{u}}_k e^{ikx} = \sum_{k=1}^{k=+\infty} \widehat{\mathbf{u}}_k e^{ikx} + \widehat{\mathbf{u}}_{-k} e^{-ikx} = \\
 &= \sum_{k=1}^{k=+\infty} (Re(\widehat{\mathbf{u}}_k) + Im(\widehat{\mathbf{u}}_k)i + Re(\widehat{\mathbf{u}}_{-k}) + Im(\widehat{\mathbf{u}}_{-k})i) \cos(kx) + \\
 &\quad + \sum_{k=1}^{k=+\infty} (Re(\widehat{\mathbf{u}}_k) + Im(\widehat{\mathbf{u}}_k)i - Re(\widehat{\mathbf{u}}_{-k}) - Im(\widehat{\mathbf{u}}_{-k})i) i \sin(kx) = \\
 &= \sum_{k=1}^{k=+\infty} 2Re(\widehat{\mathbf{u}}_k) \cos(kx) - 2Im(\widehat{\mathbf{u}}_k) \sin(kx) \in \mathbb{R} \tag{6.28}
 \end{aligned}$$

Special attention must be put concerning the contribution of the convective term. As shown in 6.15, the contribution of the convective term to the  $k$  mode is:

$$\sum_{p+q=k} \widehat{\mathbf{u}}_p i q \widehat{\mathbf{u}}_q \tag{6.29}$$

So, given a mode  $k$ , the pair of modes which contribute to the convective term are those which satisfy

$$p + q = k \tag{6.30}$$

With the spatial discretization the series is truncated to a range from  $-N$  to  $N$ . When computing the different combinations of modes  $p$  and  $q$  that accomplish 6.30, one should exclude those values which are out of bounds. This is

$$\begin{aligned}
 |p + q| &< N \\
 |p| &< N ; |q| < N
 \end{aligned} \tag{6.31}$$

Besides, taking into account that only the positive modes need to be solved, all the necessary interactions between modes (shaded region) are illustrated in the following representation.

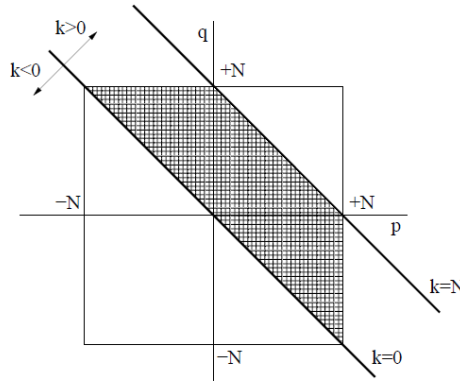


Figure 32: Possible interactions between modes. Extracted from [3].

### 6.3 Results and discussion

The diverse cases which were simulated are shown in the following table:

| Case | Method | $N$ | $C_k$ (if LES) |
|------|--------|-----|----------------|
| A    | DNS    | 20  | -              |
| B    | DNS    | 100 | -              |
| C    | LES    | 20  | 0.05           |
| D    | LES    | 20  | 0.4223         |

Table 10: Burgers' equation simulation parameters.

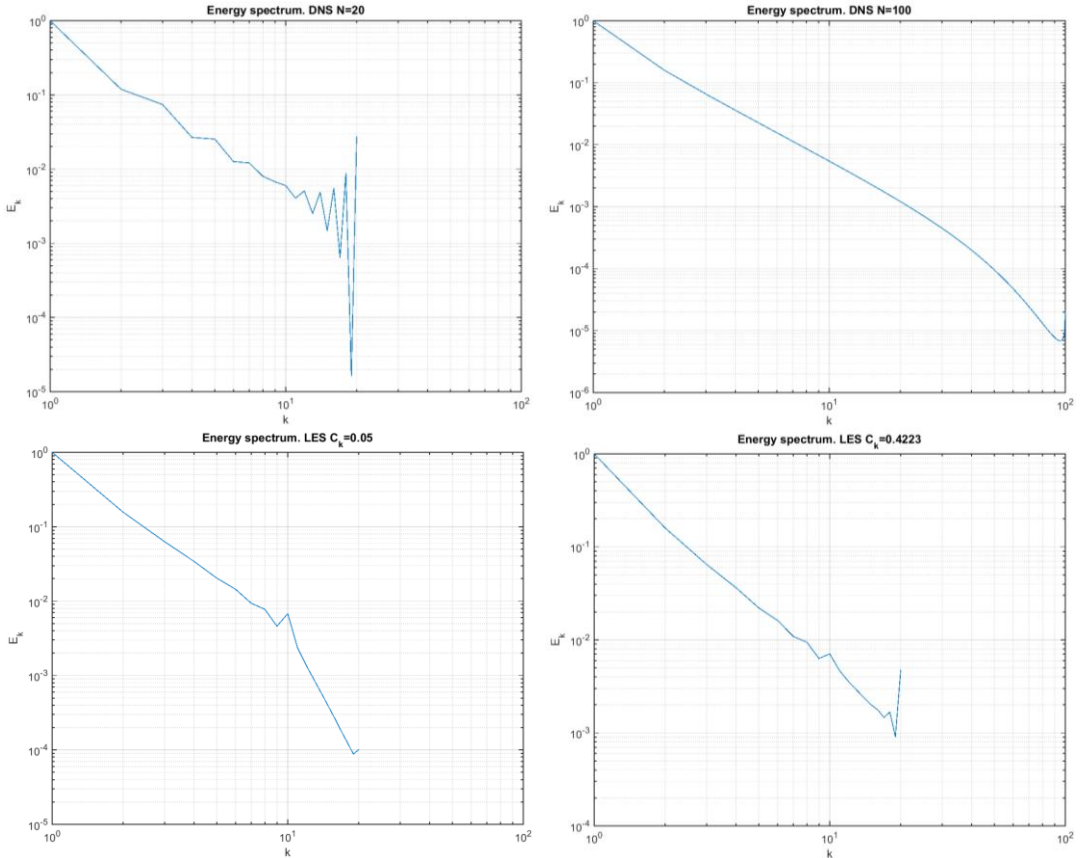


Figure 33: Energy spectrum for DNS (at the top) and LES (at the bottom).

Figure 33 displays the energy spectrum of each of the cases separately in order to improve the observation of their individual characteristics while in figure 34 all of the previous plots are put together in order to make their comparison easier.

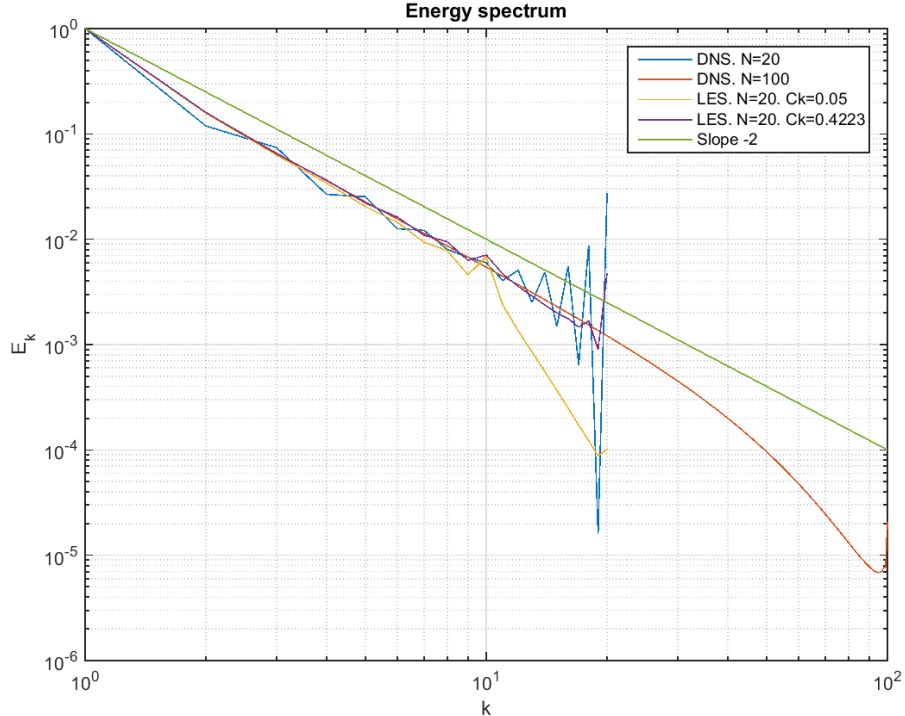


Figure 34: Superimposed energy spectra

The energy spectrum of a turbulent flow is characterized by three main parts: the area of energy input, the inertial range and the dissipation range. The energy input corresponds to the interval of low frequencies at which the energy is transferred to the fluid. The inertial range is the range in which the spectrum has almost a constant slope (in logarithmic scale). In Burgers' equation the inertial range has an approximated -2 slope. In it the diffusive term is still not very important, opposed to the dissipation range, where the diffusion gains significance and most of the energy of the flow is lost.

By means of the energy spectrum one may understand the role of each of the terms present in the Navier-Stokes equation: while the convective term is responsible for the formation of smaller scales (higher values of  $k$ ) the diffusive term tries to eliminate them, for the diffusive term acts with  $k^2$ .

With respect to figure 34, the case which reproduces most accurately the spectrum of the fluid is the one computed by means of a DNS with  $N = 100$ . Even in this case one sees a small increase in the spectrum for largest  $k$ , meaning that a finer resolution is needed. One observes that a coarser mesh ( $N = 20$ ) provides results with chaotic spectrum, explained by the fact that the scales responsible for the energy diffusion are neglected in the analysis.

Then, in order to obtain a precise solution with a DNS one must use a much finer mesh than the maximum order of magnitude of the scales of interest. Therefore, turbulence modelling methods such as LES aim to obtain these scales of interest with a mesh resolution of the same order by means of modelling the smallest scales, leading to a substantial reduction in computational costs.

The other two remaining spectra are computed with LES. Special care must be put on the election of the constants in the turbulent viscosity modelling, since the addition of more than required turbulent viscosity (case with  $C_k = 0.05$ ) may lead to invalid results, for too much energy is being dissipated (this is illustrated by the steeper slope of the spectrum). If these constants are well chosen one would obtain results which mostly agree with the actual spectrum (purple line in figure 34).

In the following figure the solution  $u(x)$  of the Burgers' equation is represented. Again, one sees as the more accurate solution is that obtained with a fine mesh with DNS. The solution obtained with the coarse mesh with a DNS presents many fluctuations, which can be soften by applying a LES model.

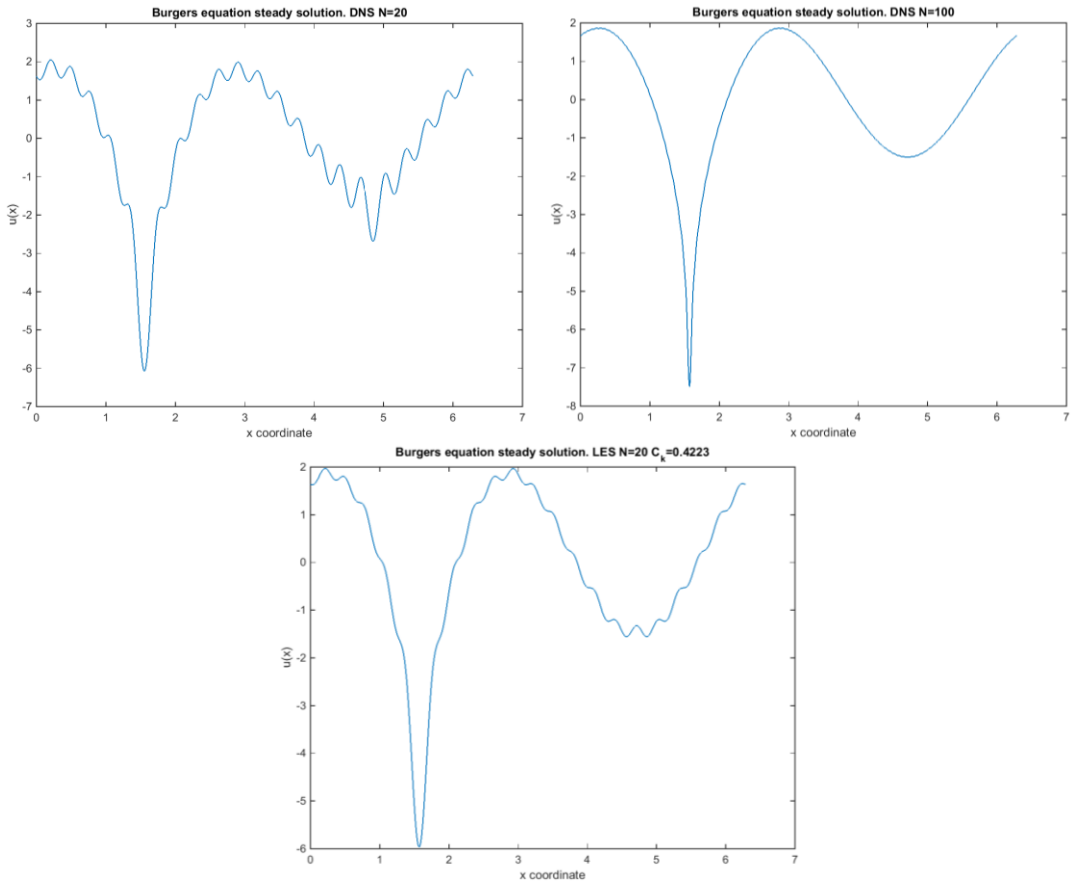


**Figure 35: Burgers' equation steady solution for DNS and LES methods**

## 7 Specific case. External Flow simulation

### 7.1 Definition of the problem

#### 7.1.1 General description

In this section, the external flow around a squared cylinder is simulated as an initial step to future more complex geometries. This case was selected since there exist several benchmark solutions. The flow is confined in a rectangular cavity, with one inlet at an extreme and an outlet at the opposite one, just as if it were the simulation of a wind tunnel test section. Also in this section, an approach to the resolution of the flow over an airfoil is performed.

The geometry of the domain, as said in previous lines, consists in a rectangle with high aspect ratio. The sketch of the domain, as well as the obstacle inside it are presented in the figure below.

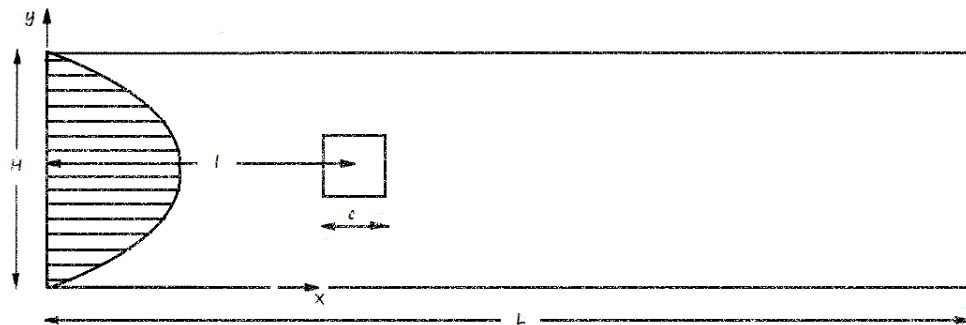


Figure 36: Domain of the problem and prescribed inlet velocity (confined flow).

#### 7.1.2 Nomenclature

| Problem data   | Numerical data   |
|--|--|
| L: length of the domain                                | N: number of control volumes   |
| H: height of the domain                                | $N_x$ : number of CV in x-direction  |
| $l_{obs}$ : obstacle's distance from inlet             | $N_y$ : number of CV in y-direction  |
| c: chord/characteristic length                         | $N_{x_u}, \gamma_{x_u}$ : number of CV and mesh concentration factor upstream in x-direction       |
| $\rho$ : density of the fluid                          | $N_{x_d}, \gamma_{x_d}$ : number of CV and mesh concentration factor downstream in x-direction     |
| $\mu$ : dynamic viscosity                              | $N_{x_{obst}}$ : number of CV along obstacle in x-direction  |
| $u_{in}$ : inlet velocity profile                      | $N_{y_u}, \gamma_{y_u}$ : number of CV and mesh concentration factor above obstacle in y-direction |
| $u_{out}$ : outlet velocity                            | $N_{y_d}, \gamma_{y_d}$ : number of CV and mesh concentration factor below obstacle in y-direction |
| $u_{max}$ : inlet parabolic profile                    | $N_{y_{obst}}$ : number of CV along obstacle   |
| maximum velocity                                       |  |
| $u_\infty$ : velocity of the undisturbed upstream flow |  |
| $p_\infty$ : pressure of the undisturbed upstream flow |  |
| $Re$ : Reynolds number                                 |  |
| Problem variables                                      |  |
| x: coordinate  |  |
| y: coordinate  |  |

|  |   |
|--|---|
| $\mathbf{r}$ : coordinates (vector)                              | in y-direction  |
| $u$ : horizontal velocity  | $\Delta t$ : time step  |
| $v$ : vertical velocity  | $\Delta x$ : mesh horizontal size   |
| $\mathbf{v}$ : velocity field (vector)                           | $\Delta y$ : mesh vertical size   |
| $\mathbf{R}(\mathbf{v})$ : convective + diffusive + source terms | $\Delta x_d$ : horizontal nodal distance  |
| $p$ : pressure   | $\Delta y_d$ : vertical nodal distance  |
| $\psi$ : stream function   | $F$ : volumetric flux (i.e. $\int_{\partial\Omega}  \mathbf{v} \cdot d\mathbf{S} $ )              |
| $\zeta$ : vorticity  | <b>Subscripts</b>   |
| $C_p$ : pressure coefficient                                     | $\phi_n, \phi_s, \phi_e, \phi_w$ refer to the wall of the volume at which variables are evaluated |
| $d$ : drag (per unit length)                                     | $\phi_N, \phi_S, \phi_E, \phi_W, \phi_P$ refer to the node at which variables are evaluated       |
| $C_d$ : drag coefficient   |   |
| $l$ : lift (per unit length)                                     | <b>Superscripts</b>   |
| $C_l$ : lift coefficient   | $\phi^{n+1}$ : current instant  |
| $L_r$ : recirculation length                                     | $\phi^n$ : previous instant   |
| $St$ : Strouhal number   | $\phi^{n-1}$ : previous to previous instant   |
| $t$ : time   |   |

### 7.1.3 Governing equations

The equations that define the problem are the same that were used in the resolution of the Lid Driven Cavity problem (see section 4.1.3): mass and momentum conservation equations.

The only difference is that the Reynolds number is based on the maximum inlet velocity  $u_{max}$  of the parabolic distribution and the chord or characteristic length of the obstacle ( $c$ ), as this parameters are the ones used for the adimensionalization process.

$$Re = \frac{\rho u_{max} c}{\mu} \quad (7.1)$$

For the confined flow, a parabolic distribution of the inlet velocity to simulate a fully-developed flow is used, and its dimensionless expression is the following:

$$u_{in}(y) = \frac{4}{H^2} (H - y) y \quad (7.2)$$

For the outlet a convective boundary condition is used:

$$\frac{\partial u}{\partial t} + u_{conv} \frac{\partial u}{\partial x} = 0 \quad (7.3)$$

$$\frac{\partial v}{\partial t} + u_{conv} \frac{\partial v}{\partial x} = 0 \quad (7.4)$$

Where  $u_{conv}$  is a characteristic velocity and may be set equal to  $u_{max}$ . This special type of boundary condition ensures that vortices can approach and pass the outflow boundary with no important disturbances and/or reflections into the inner domain [18]. A small correction factor is applied to the velocities resultant of this condition in order to ensure mass conservation over the whole domain. The integration domain behind the cylinder is set to be large enough to have no influence over the solution at all.

## 7.2 Numerical methods

### 7.2.1 Time-integration

The scheme used for the integration over time of the equations is the same as described in previous sections (namely section 4.2.1). However, in the present problem one finds an additional time-dependent expression, which is the convective boundary condition at the outlet. A second order approximation may be used as well:

$$\frac{u^{n+1} - u^n}{\Delta t} + u_{max} \left( \frac{3}{2} \frac{\partial u^n}{\partial x} - \frac{1}{2} \frac{\partial u^{n-1}}{\partial x} \right) = 0 \quad (7.5)$$

$$\frac{v^{n+1} - v^n}{\Delta t} + u_{max} \left( \frac{3}{2} \frac{\partial v^n}{\partial x} - \frac{1}{2} \frac{\partial v^{n-1}}{\partial x} \right) = 0 \quad (7.6)$$

### 7.2.2 Spatial integration

The spatial discretization of the governing equations is analogous to the process described in the section referring to the Lid Driven Cavity (4.2.2).

The main issue in the spatial integration is how to deal with such a large integration domain. For instance, if a mesh similar to the one used in the Differentially Heated Cavity (uniform mesh with a mesh resolution of  $\Delta x = 0.01$ ) is to be used, 4,000,000 control volumes would result. Obviously, this is a nonsense, as the computational costs would be extremely high as well as the requirement concerning the code's suitability to be executed on an average PC would not be satisfied. Therefore, some strategy has to be thought. One may implement a non-uniform structured mesh which provided enough accuracy and resolution in the obstacle vicinity by using an hyperbolic distribution similar to 4.32, concentrating the mesh near the object instead of doing so in regions closer to the wall. This enables a more accurate solution, as these areas are the most demanded, as well as it makes the reproduction of more complex geometries easier. In this case, the mesh is divided in three sub domains: one containing the obstacle, which is a uniform mesh, and the two other resulting, which stretch at the extreme in contact with the obstacle. Then, the size of the  $i^{th}$  node of a group of  $N$  nodes extending a certain longitude  $L$  reads:

$$\Delta x_i = L \frac{\tanh\left(\gamma \frac{i}{N}\right) - \tanh\left(\gamma \frac{i-1}{N}\right)}{\tanh \gamma} \quad (7.7)$$

In the following images, an example of this non-uniform meshes may be observed, where the CV nodes are represented. The areas with more concentration of nodes appear in the image as darker blue regions.

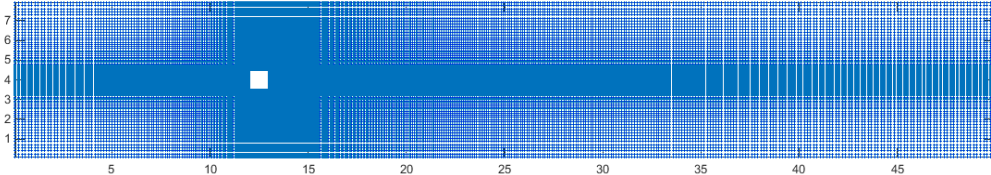


Figure 37: Non-uniform mesh example.

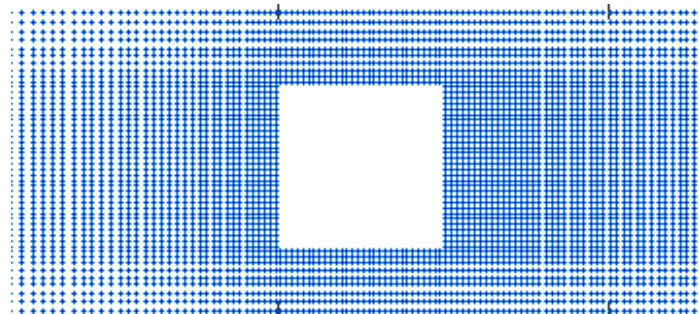


Figure 38: Detail of the mesh in the obstacle's vicinity.

In the table below the parameters with which the mesh was elaborated are gathered.

| $N_x = 500$ |                |           |                |                            | $N_y = 100$ |                |           |                |                            |
|-------------|----------------|-----------|----------------|----------------------------|-------------|----------------|-----------|----------------|----------------------------|
| $N_{x_u}$   | $\gamma_{x_u}$ | $N_{x_d}$ | $\gamma_{x_d}$ | $N_{x_{obs}}$<br>(uniform) | $N_{y_u}$   | $\gamma_{y_u}$ | $N_{y_d}$ | $\gamma_{y_d}$ | $N_{y_{obs}}$<br>(uniform) |
| 116         | 1.454          | 354       | 1.456          | 30                         | 35          | 1.448          | 35        | 1.448          | 30                         |

Table 11: Example mesh parameters.

### 7.3 Results and discussion

Two important parameters to be computed regarding external flow analysis are the drag and lift coefficients. These are defined:

$$C_d = \frac{d}{\frac{1}{2} \rho u_\infty^2} \quad (7.8)$$

$$C_l = \frac{l}{\frac{1}{2} \rho u_\infty^2} \quad (7.9)$$

Another coefficient which is often used is the pressure coefficient:

$$C_p = \frac{p - p_\infty}{\frac{1}{2} \rho u_\infty^2} \quad (7.10)$$

In this case, velocity  $u_\infty$  is set equal to  $u_{max}$  and  $p_\infty$  is equal to the pressure at the inlet of the cavity. Drag and lift per unit length are obtained through the integration of viscous and pressure forces acting all over the obstacle's surface and projecting the resulting force onto parallel and perpendicular directions of the flow.

$$d = \left( \oint \mu(\nabla v)^T \cdot \hat{n} dS - \oint p \cdot \hat{n} dS \right) \cdot \hat{i} \quad (7.11a)$$

$$l = \left( \oint \mu(\nabla v)^T \cdot \hat{n} dS - \oint p \cdot \hat{n} dS \right) \cdot \hat{j} \quad (7.12a)$$

For a Cartesian mesh with horizontal velocity inlet, these expressions are rewritten as follows:

$$d = \mu \left( \int_s \frac{\partial u}{\partial y} \Big|_s dx - \int_n \frac{\partial u}{\partial y} \Big|_n dx \right) + \int_e p_e dy - \int_w p_w dy \quad (7.11b)$$

$$l = \mu \left( \int_w \frac{\partial v}{\partial x} \Big|_w dy - \int_e \frac{\partial v}{\partial x} \Big|_e dy \right) + \int_n p_n dx - \int_s p_s dx \quad (7.12b)$$

Subscripts in equations 7.11b and 7.12b refer to the control volumes in contact with the obstacle.

### 7.3.1 Confined flow over a square cylinder

The problem of the confined flow over a square cylinder simulated in this paper has the same parameters used in [18] on the grounds that a validation of the code by direct comparison of both results may be done. These parameters (non-dimensional) are found in the following table:

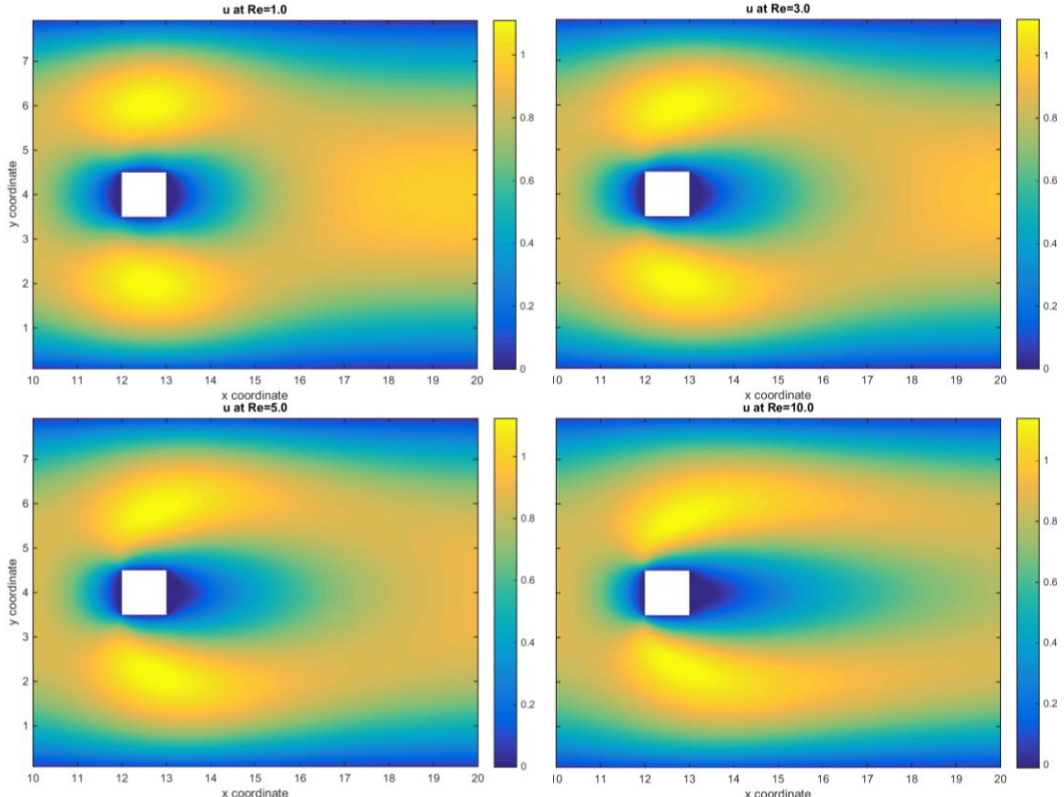
|           |      |
|-----------|------|
| <b>L</b>  | 50.0 |
| <b>H</b>  | 8.0  |
| $l_{obs}$ | 12.5 |

Table 12: Geometrical parameters of the problem.

Steady range  $0.5 \leq Re < 60$

As described in [18], for small Reynolds numbers the flow is dominated by viscous forces and it reaches steady state. When increasing  $Re$  the flow firstly separates at the trailing edges of the cylinder forming two symmetric recirculation vortices which become larger every time. This tendency remains till a certain Reynolds number is reached, when the separation of the flow occurs alternatively at the upper and lower trailing edge, giving birth to wake oscillations: the well-known von Kármán vortex street. This critical value of Reynolds oscillates around 60. In the following two figures contour plots of the horizontal (figure 39) and of the vertical velocity (figure 40) are shown.

The mesh parameters used to obtain the following results are those given in table 11.



- Specific case. External Flow simulation -

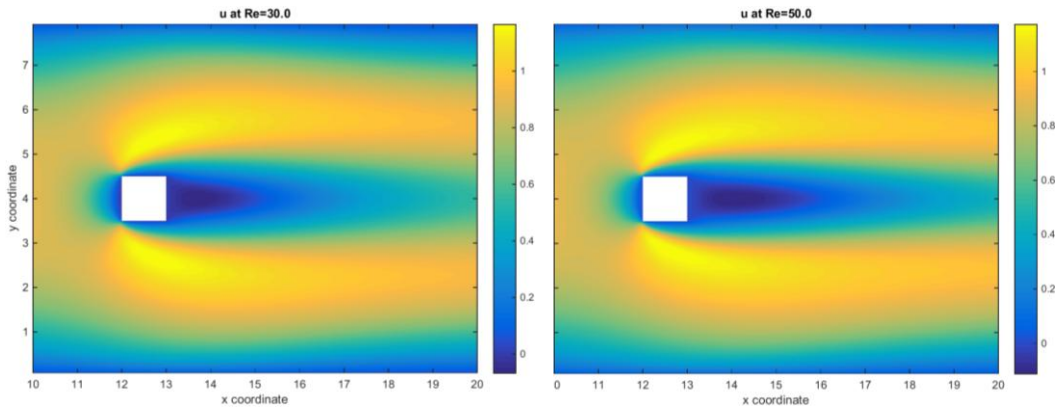


Figure 39: Horizontal velocity contour plots for different Reynolds numbers.

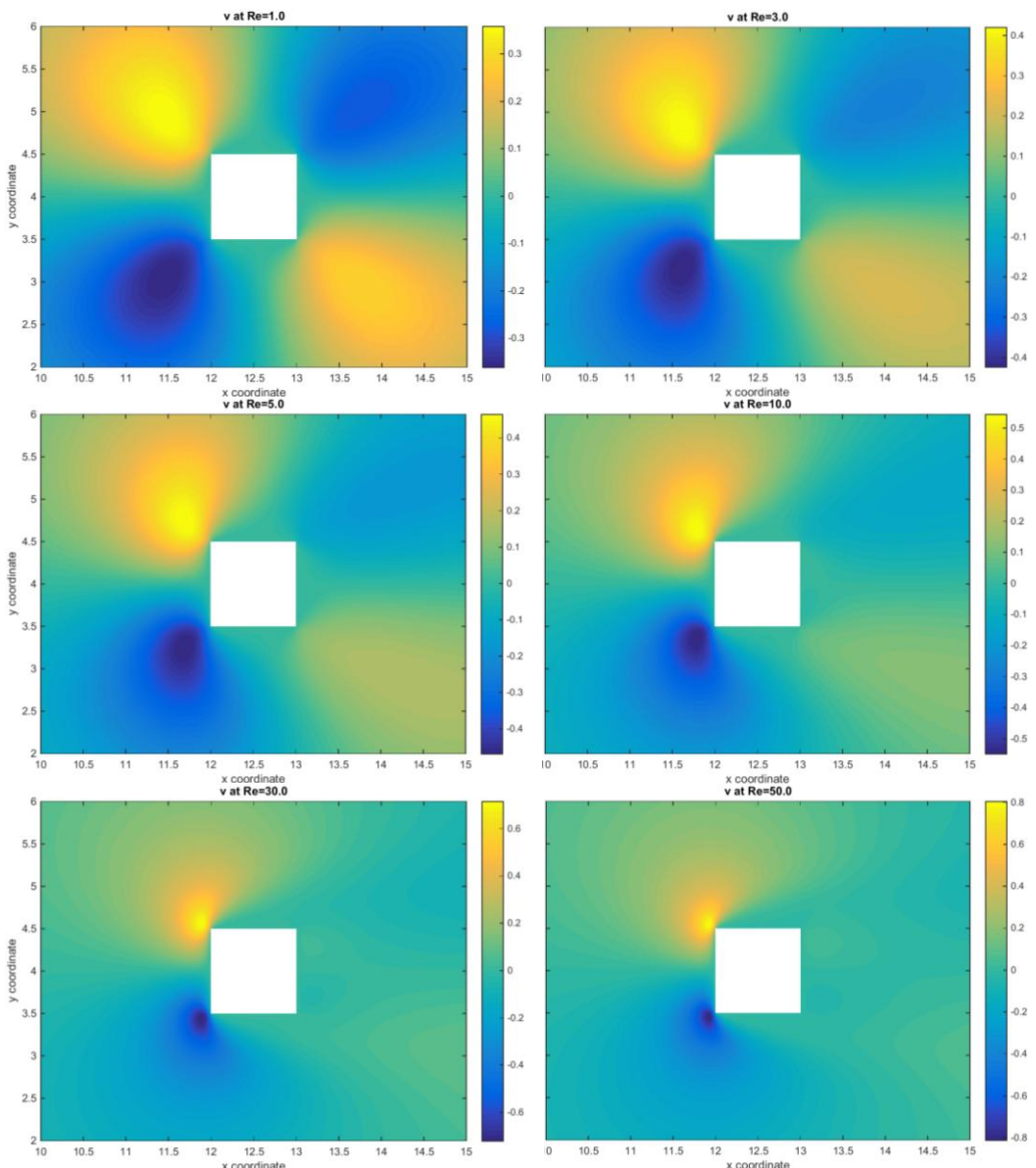
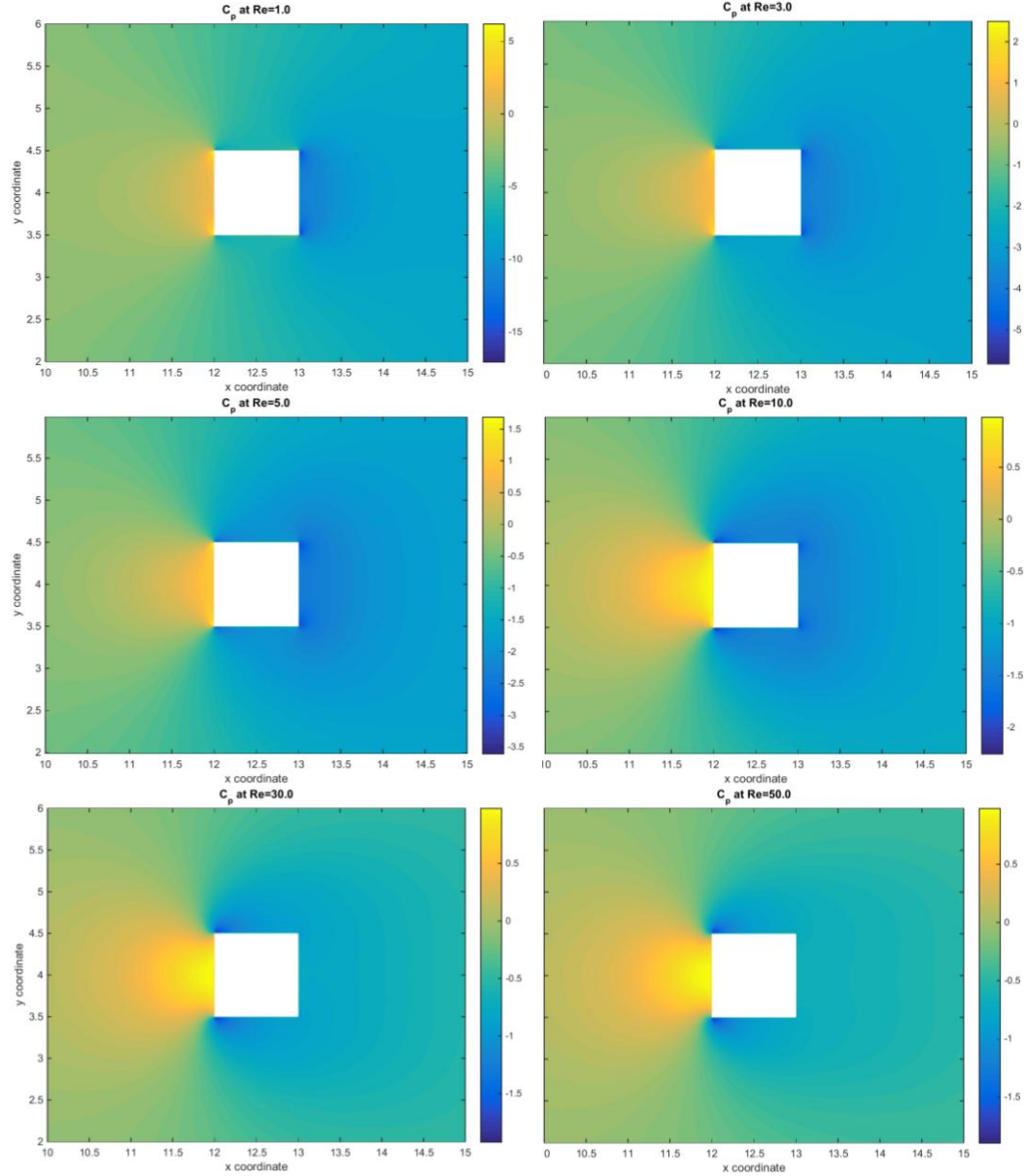


Figure 40: Vertical velocity contour plots for different Reynolds numbers.

Figure below presents contour plots of the pressure coefficient for different Reynolds numbers. They clearly show how the region in front of the cylinder is characterized for positive pressure coefficients while the rear regions suction is produced. This generates an overall resistive force, which decreases with Reynolds numbers, since  $C_p$ 's magnitude decreases.



**Figure 41: Pressure coefficient  $C_p$  contour plots for different Reynolds numbers.**

Streamline plots are, perhaps, the ones which provide more information regarding flow patterns. The tendency described in previous lines is clearly observable in the following images: the flow separates at the trailing edge even for the smallest Reynolds number considered. This separation lead to the appearance of a recirculation zone behind the cylinder (observable in the fourth plot, corresponding to  $Re = 10$ ) and two vortices. The size of this area increases with Reynolds number.

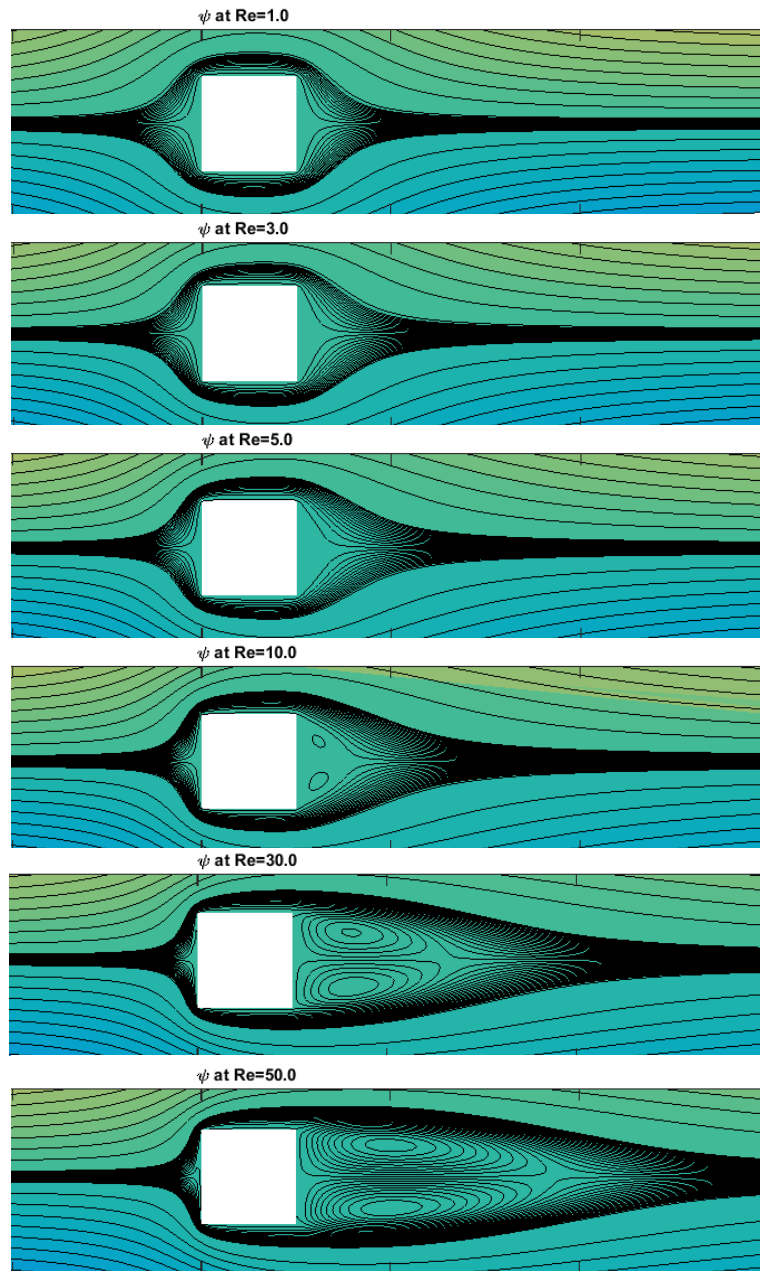


Figure 42: Streamlines for different Reynolds numbers.

In the table below the computed values of the drag and lift coefficients are presented. As expected,  $C_d$  values decrease with Reynolds number while  $C_l$  remains negligible during all the considered range, which is obvious since the problem's geometry is symmetric with respect the horizontal mid-plane.

Strong correspondence was found between the obtained  $C_d$  results and those provided by the bench mark solution (figure 43).

| $Re$ | $C_d$  | $C_l$                   |
|------|--------|-------------------------|
| 1    | 23.701 | $5.716 \cdot 10^{-11}$  |
| 3    | 8.560  | $2.718 \cdot 10^{-15}$  |
| 5    | 5.666  | $-1.067 \cdot 10^{-15}$ |
| 10   | 3.509  | $9.600 \cdot 10^{-15}$  |
| 30   | 1.923  | $-1.811 \cdot 10^{-14}$ |
| 50   | 1.534  | $-1.731 \cdot 10^{-10}$ |

Table 13: Obtained  $C_d$  and  $C_l$  results.

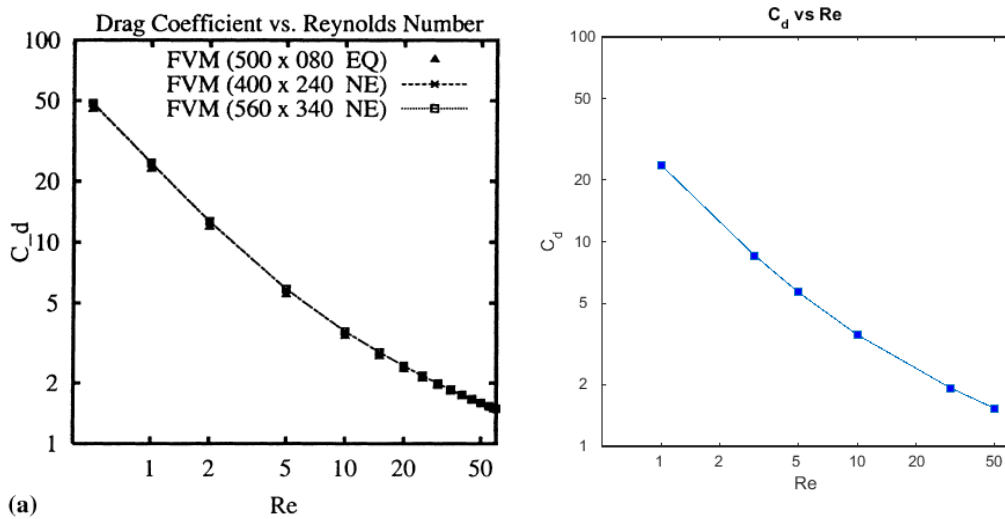


Figure 43:  $C_d$  vs  $Re$  comparison. Left graph extracted from [18].

Recirculation size was also computed and compared with the benchmark solution and convergence between both results has also been achieved.

| $Re$ | $L_r$ |
|------|-------|
| 1    | 0.000 |
| 3    | 0.065 |
| 5    | 0.205 |
| 10   | 0.490 |
| 30   | 1.630 |
| 50   | 2.700 |

Table 14: Recirculation area length obtained .

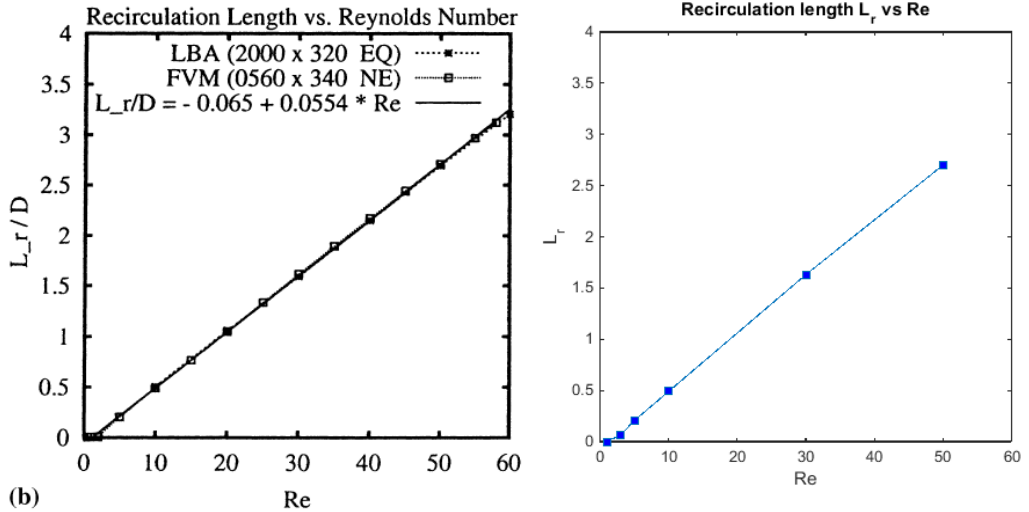


Figure 44:  $L_r$  comparison. Left graph extracted from [18].

Recirculation length has been computed by plotting the horizontal velocity at the horizontal mid-plane. When the recirculation region appears, horizontal velocity behind the cylinder becomes negative, then the end of this area is found at the point in which horizontal velocity becomes positive again.

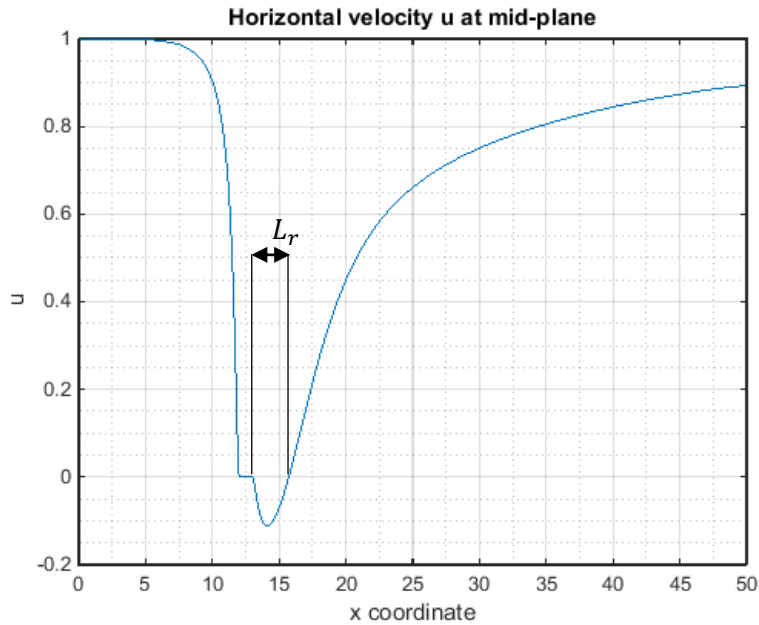
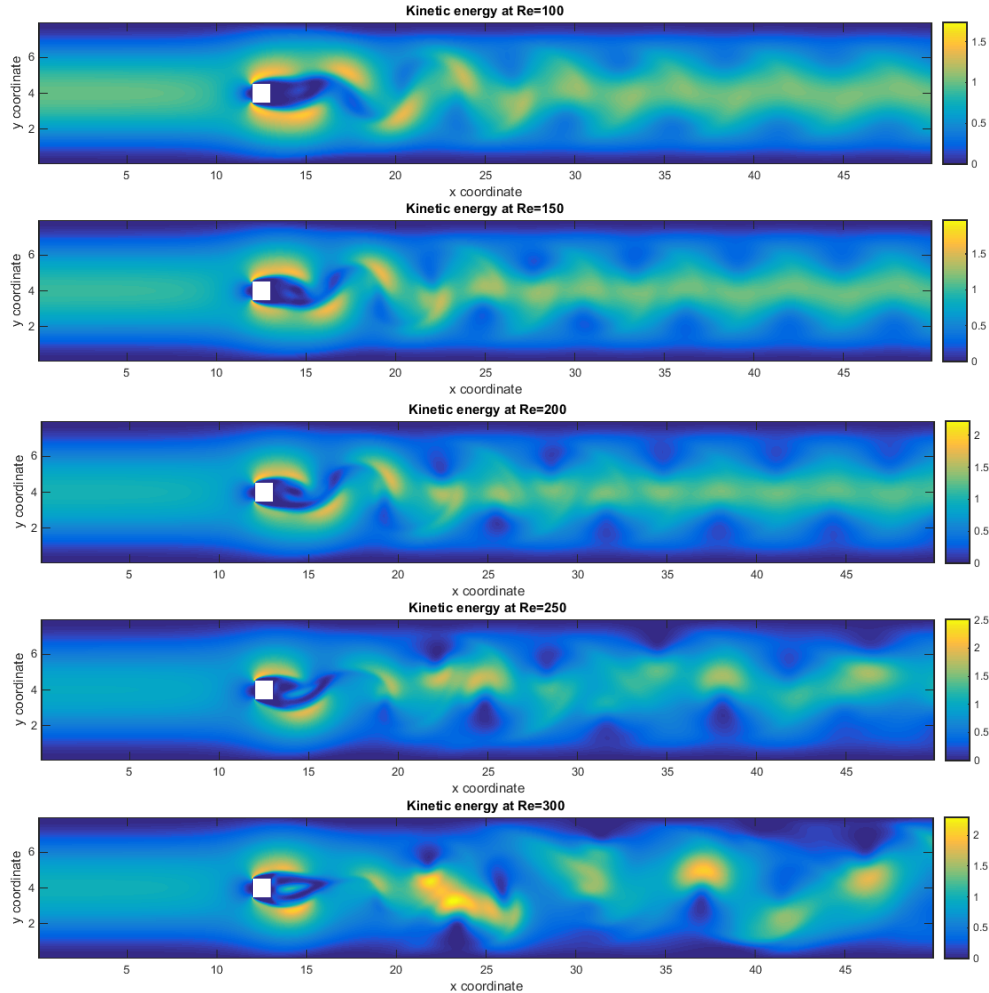


Figure 45: Recirculation length measurement

Unsteady range  $60 \leq Re \leq 300$

The following figures present the contour plots of flow's kinetic energy, the pressure coefficient and the streamlines for different Reynolds numbers. The results are very interesting, since they permit the visualization of the von Kármán vortices. These contour plots were computed at the final simulation time, which was set equal to 500.

Regarding kinetic energy contour plots, it is seen how as  $Re$  increases the plots appear every time to have more contrasted colours, as the flow is becoming less viscous. For  $Re = 200$  the von Kármán vortices are clearly visible and well-defined, while for higher Reynolds number, the vortices appear to have a more chaotic behaviour.



**Figure 46: Kinetic energy contour plots for different Reynolds numbers.**

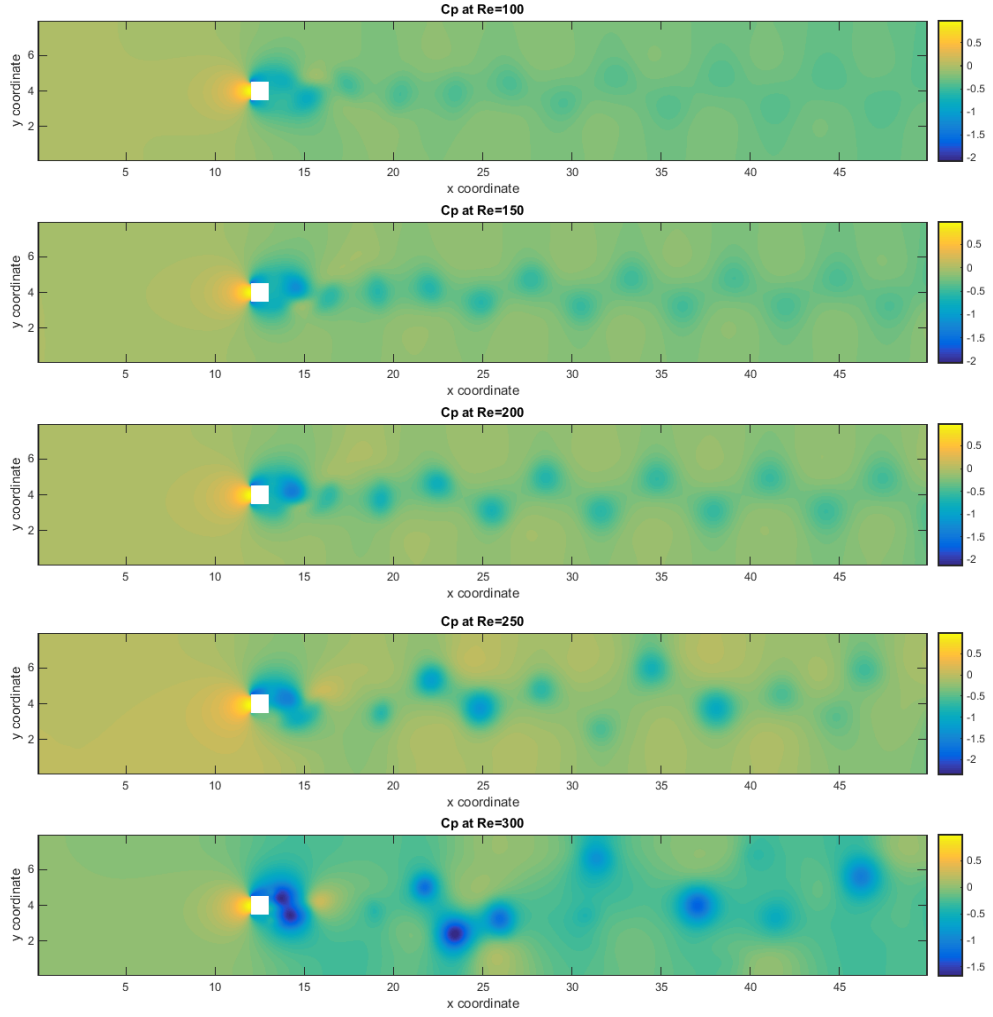


**Figure 47: Pressure coefficient contour plots for different Reynolds numbers.**

$C_p$  contour plots justify the oscillations in lift and drag coefficients. It is clear that pressure is not symmetrically distributed with respect to the horizontal mid-plane, and it is this asymmetry what gives birth to an oscillating lift force. The blue areas, which correspond to suction regions, appear alternatively at the upper and the lower sides of the cylinder, leading to a resultant net vertical force.

One may also notice how the suction regions seem to behave again in a more chaotic way for the highest Reynolds number, as well as they look more reluctant to fade away and dissipate.

Next figure presents some streamlines. It is remarkable the fact that the flow separates at the leading edges of the cylinder, opposed to the separation pattern which occurred at the steady range. The reduction of the recirculation zone with  $Re$  is also noticeable.

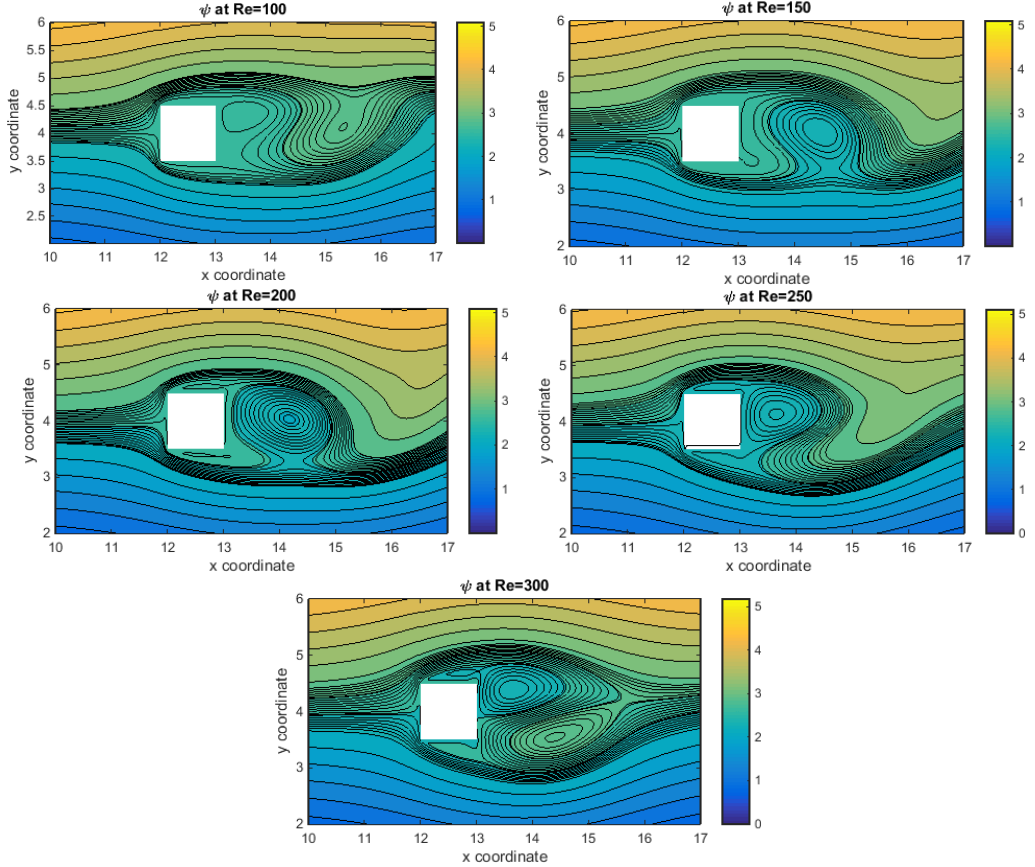


Figure 48: Streamlines for different Reynolds numbers.

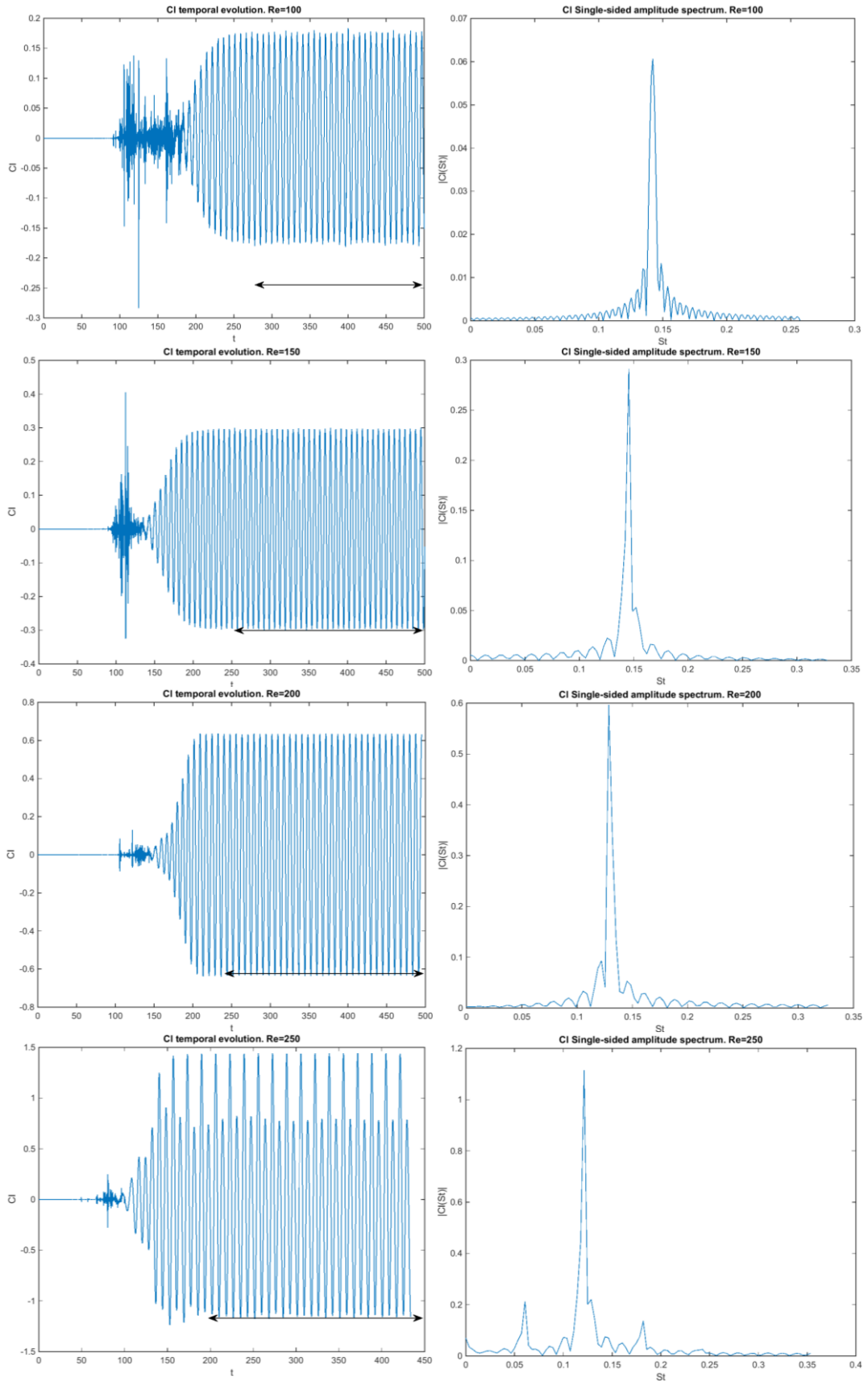
As commented in previous lines and seen in figures above, when a certain value of Reynolds is reached, the flow becomes unsteady, leading to the appearance of the von Kármán vortices. Therefore, fluctuations in the aerodynamic forces arise, which can be characterized by its frequency. This frequency may be determined by the spectral analysis of the lift coefficient, by means of a Fast Fourier Transform. The dimensionless frequency which would result from the analysis of the problem's dimensionless variables is known as Strouhal number, and it is defined as follows:

$$St = \frac{fc}{u_{max}} \quad (7.13)$$

Here are presented the time evolution plots of the lift coefficients for different Reynolds numbers, as well as the corresponding one-sided amplitude spectrum. The areas marked by arrows in the lift coefficient plots indicate the domain where the fast Fourier transform was applied, since these are the areas where the periodic oscillations are fully developed. All simulations were stopped at a dimensionless time of 500.

- Specific case. External Flow simulation -

---



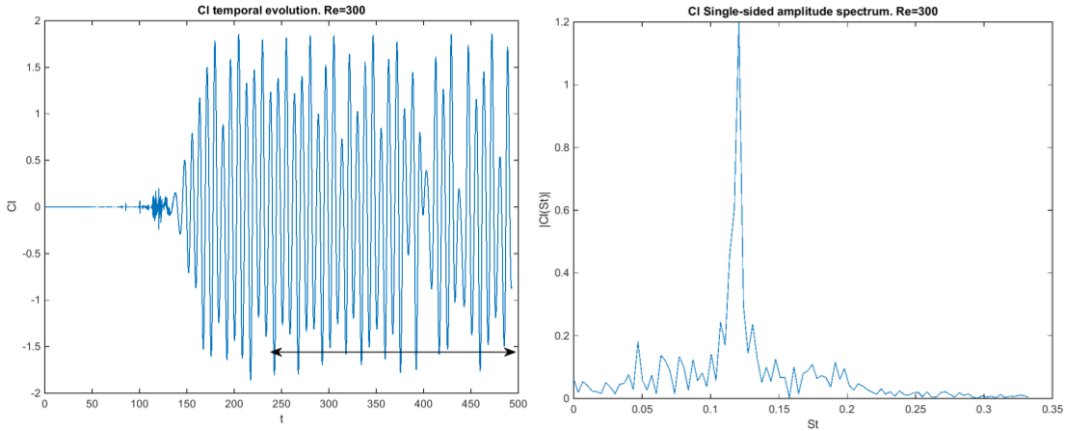


**Figure 49: Lift coefficient time evolution and amplitude spectrum for different Reynolds.**

The Strouhal numbers obtained for each of the Reynolds that were considered are gathered in the table below, as well as the  $St(Re)$  curve comparison with the values given by Breuer et al. [18].

| <i>Re</i> | <i>St</i> |
|-----------|-----------|
| 100       | 0.1422    |
| 150       | 0.1455    |
| 200       | 0.1287    |
| 250       | 0.1213    |
| 300       | 0.1208    |

**Table 15: Computed Strouhal numbers.**

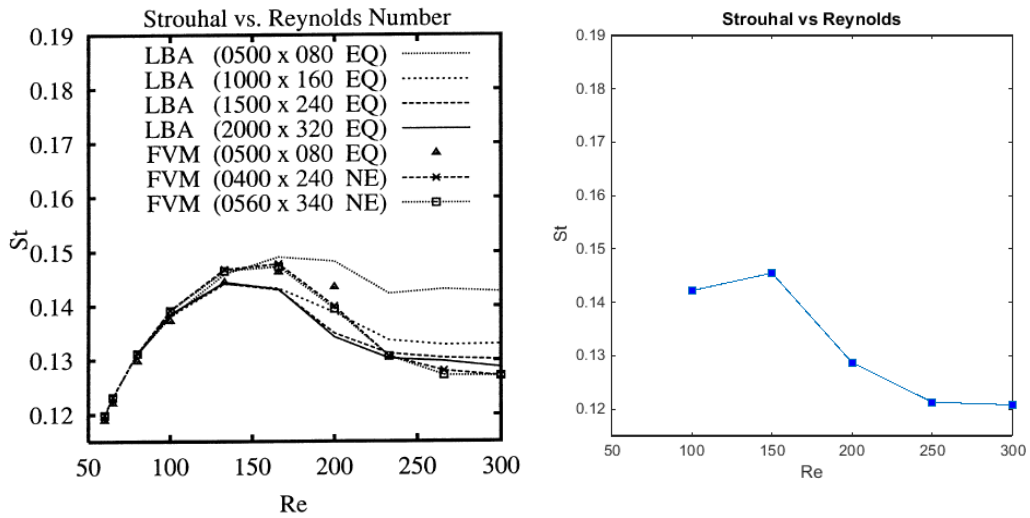


**Figure 50:  $St(Re)$  curve comparison. Left graph extracted from [18].**

Although a rigorous comparison cannot be done on the grounds that the literature does not provide exact values, the fact that the Strouhal number is very dependent on mesh and time resolutions (one may notice the variability of the results given in the benchmark solution, depending on the mesh and method

used) and the little number of cases computed, the general tendency of the Strouhal curve is similar, as so are the values. This curve presents a maximum which may be located approximately at  $Re = 150$ .

Another curve whose comparison with benchmark results may be of interest is the drag coefficient plot versus Reynolds. Since  $C_d$  presents fluctuations with respect time (figure 51), the average value has been computed by using the same time intervals which were used for the lift coefficient's FFT.

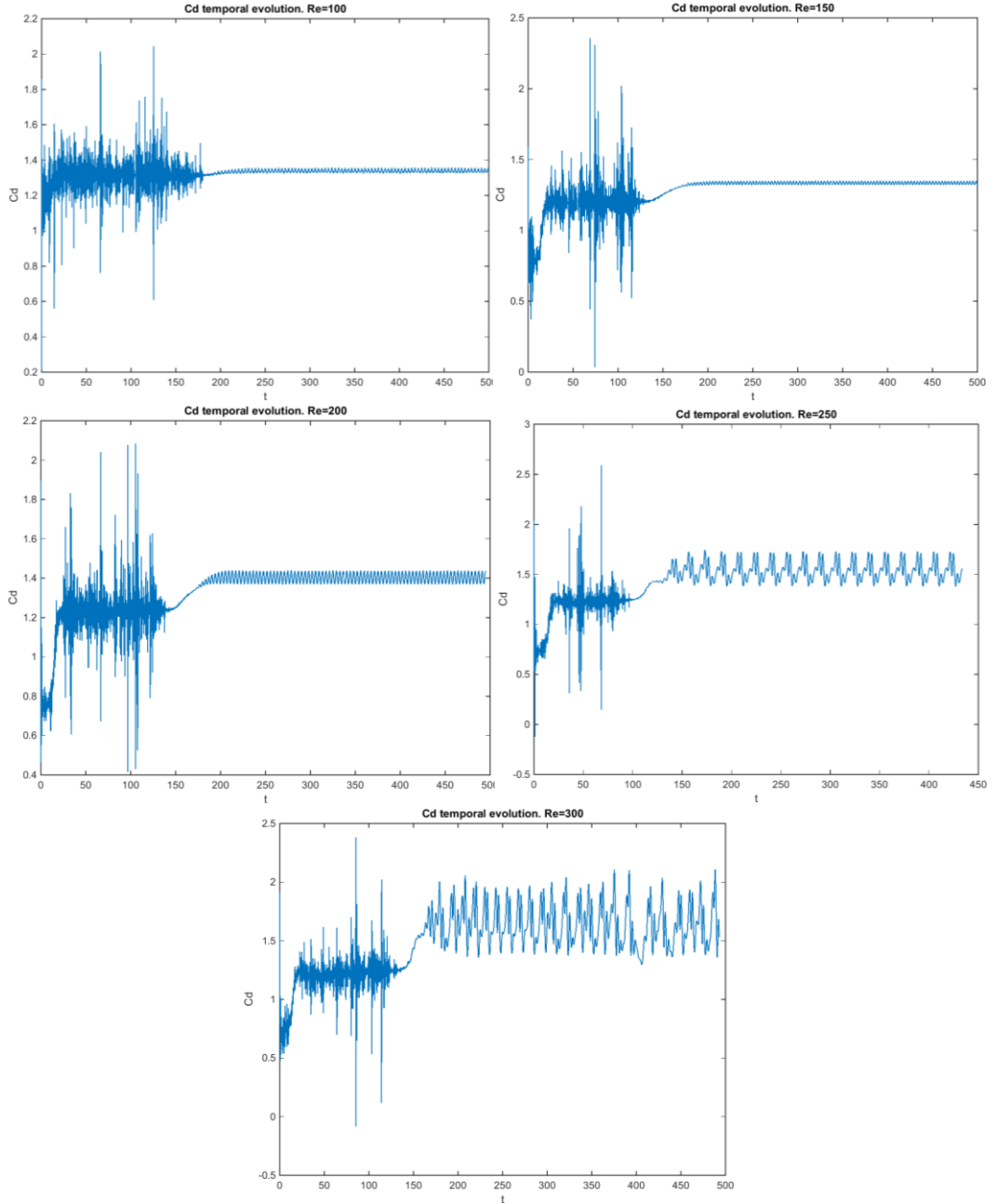


**Figure 51: Drag coefficient time evolution for different Reynolds.**

It is noticeable that the amplitude of the oscillations increase with  $Re$ , as occurs with lift coefficient. Table 16 gathers the computed mean drag coefficients.

| $Re$ | $C_d$  |
|------|--------|
| 100  | 1.3385 |
| 150  | 1.3343 |
| 200  | 1.4036 |
| 250  | 1.5402 |
| 300  | 1.6425 |

Table 16: Computed mean drag coefficients.

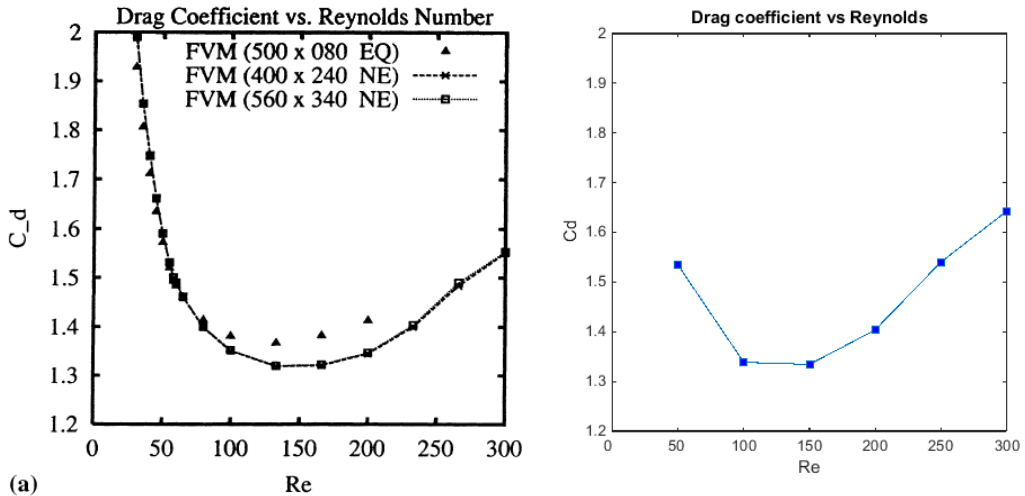


Figure 52:  $C_d(Re)$  curve comparison. Left graph extracted from [18].

Again, although the comparison may not be much accurate, the general trend of the  $C_d$  curve is followed, with a relative minimum around  $Re = 150$ .

By observing both figures 49 and 51, one sees that for the maximum Reynolds number the lift and drag oscillations begin to lose the strict periodicity present in lower Reynolds cases. This may be a consequence of approaching the region in which the flow cannot be regarded as a 2-D flow anymore, because of the appearance of the turbulence phenomenon and its 3D vortex structures. Breuer et al. [18] comment on this very same fact, and assume  $Re = 300$  to be a diffuse border between the laminar and the turbulent flow for this problem.

Another aspect of the lift and drag evolutions with respect to time which may attract attention is the appearance of strong perturbations from the initial time to the time at which the periodic oscillations commence to settle. This may be due to the initial conditions of the simulation, as the fluid has to evolve from an initial motionless state with a prescribed inlet velocity to a fully developed flow all over the domain.

### 7.3.2 Confined flow over an airfoil

The simulation of the external flow over a simple geometry obstacle, for instance a square, permitted the development of general code which is able to solve more complex geometries. With the certainty that the code is correct, since it is formed by means of the inclusion of the already validated codes used in benchmark problems such as Smith Hutton or Lid Driven Cavity and the fact that the previous simulations with the square cylinder were proven to reach a good agreement with reference results, it may be applied to the resolution of a flow over an airfoil. However, the fact that the mesh is Cartesian adds a strong limitation concerning accuracy, for it is extremely difficult to reproduce such complex shapes with rectangular control volumes. In order to achieve a fair approximation of the airfoil, the mesh has to be extremely refined at its vicinity, thus requiring a large number of nodes and high computational costs.

The selected airfoil to conduct some tests was a NACA 7414, since it is an airfoil with high camber which produces lift for null angle of attack. The flow is again confined in order to directly reuse the code developed for the square cylinder, though it may be implemented for free flows by imposing convective boundary conditions (7.3 and 7.4) at both the upper and the lower walls (the derivatives in this case with respect to the normal boundary direction). The integration domain was reduced in order to increase the resolution of the mesh without increasing the total number of nodes. This should not affect in great measure the results, since unsteady flow is not to be simulated and therefore unsteady wakes are not expected to appear. Then, the geometrical parameters for this case appear below:

|           |      |
|-----------|------|
| $L$       | 15.0 |
| $H$       | 4.0  |
| $l_{obs}$ | 5.0  |

Table 17: Geometrical parameters of the airfoil case.

The mesh generated may be seen in the following figure:

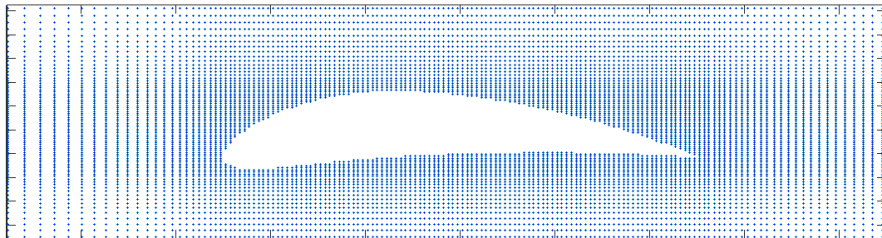


Figure 53: Mesh detail at the airfoil's vicinity.

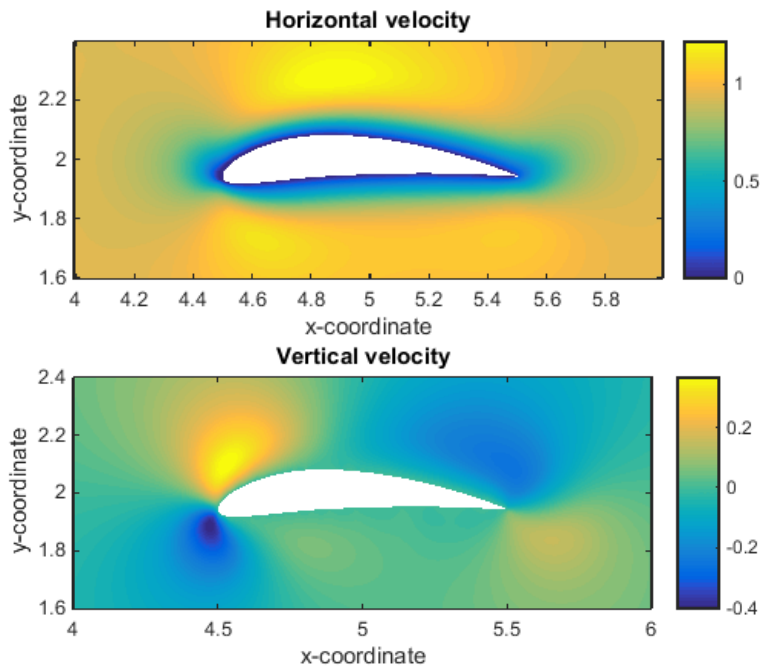
The grid was also elaborated by means of hyperbolic tangent distributions, whose main parameters are gathered in table 18.

| $N_x = 300$ |                |           |                |                            | $N_y = 150$ |                |           |                |                            |
|-------------|----------------|-----------|----------------|----------------------------|-------------|----------------|-----------|----------------|----------------------------|
| $N_{x_u}$   | $\gamma_{x_u}$ | $N_{x_d}$ | $\gamma_{x_d}$ | $N_{x_{obs}}$<br>(uniform) | $N_{y_u}$   | $\gamma_{y_u}$ | $N_{y_d}$ | $\gamma_{y_d}$ | $N_{y_{obs}}$<br>(uniform) |
| 65          | 2.0299         | 135       | 135            | 100                        | 55          | 2.1711         | 55        | 2.1711         | 40                         |

Table 18: Airfoil's case mesh parameters.

Many cases with different Reynolds numbers were investigated but none of them reached steady state or presented a fully developed flow, despite low Reynolds numbers were used. The main issue is the extremely slowness with which every time step is solved, since a large number of iterations is required to solve the pressure Poisson equation (see 4.19). Therefore, it would take hours and hours of simulation for the flow to evolve from the initial conditions to a fully developed flow. At the time this paper was submitted, some cases were being analysed and neither steady solution was reached nor periodic oscillations were detected.

Nevertheless, amongst the different cases mentioned, some plots at a certain instant with  $Re = 50$  are presented, in order to visualize some of the variables computed.



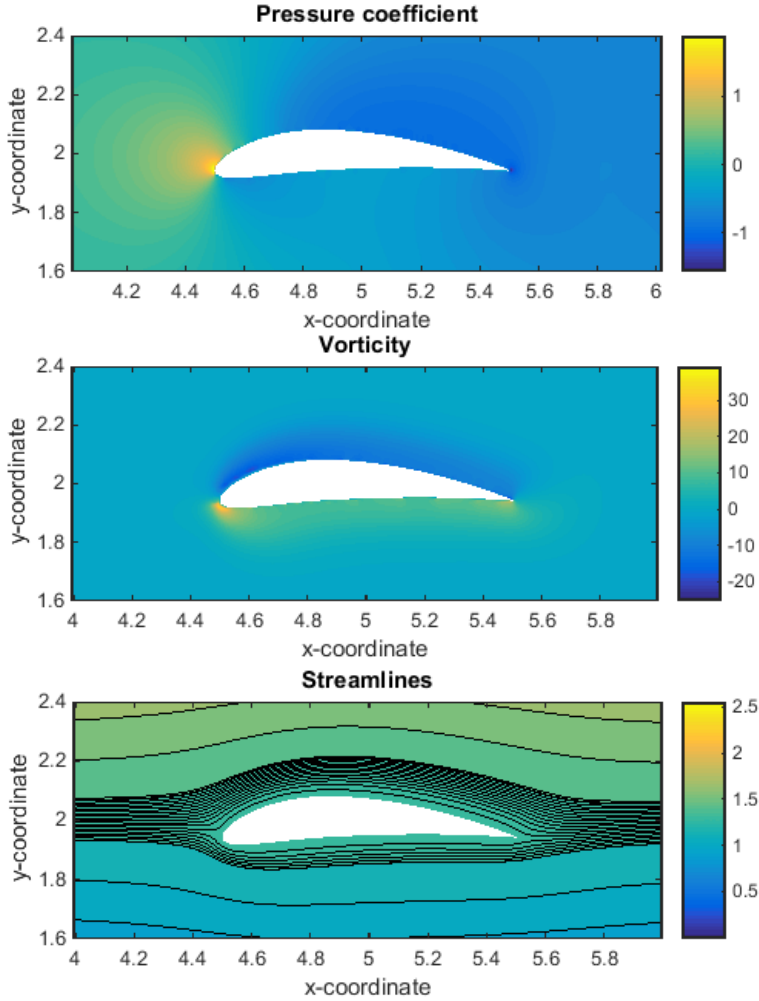


Figure 54: Contour plot of different computed variables at a certain time.

The corresponding computed values of  $C_l$  and  $C_d$  are gathered in the following table:

|       |        |
|-------|--------|
| $C_l$ | 0.2326 |
| $C_d$ | 0.8072 |

Table 19: Computed lift and drag coefficients.

These results may not be representative, as they are computed from data which may not be neither real nor accurate. However, the presented results appear to be reasonable. It is noticeable the significance of the viscous terms, which translates in a  $C_d$  higher than the lift coefficient, since the Reynolds considered is very low.

## 8 Conclusions and recommendations for future research

This study was intended to provide the author of this paper with expertise in the field of Computational Fluid Dynamics. As stated in the justification chapter, courses on this field are not offered in the vast majority of the undergraduate programmes in aerospace engineering and may be found in rather specific graduate programmes (MSc) on CFD and related topics. Therefore, having acquired a general and basic knowledge of the methods and numerical algorithms used to solve complex equations such Navier-Stokes may bring the opportunity to stand out academically among peer students.

In general terms, the scope and the specifications of the study have been accomplished. If something has to be pointed out regarding the first part of the study (the resolution of benchmark problems) it is that the developed codes produced results which coincided with benchmark solutions almost perfectly, with slight discrepancies probably due to the different numerical methods and approximations that were used or to the different types and refinements of meshes, amongst other reasons.

One of the most remarkable achievements of this study is the fact that one learns how to obtain good solutions with a desired order of accuracy. In CFD it is difficult to make sure that a code has no errors or that it provides a correct solution. However, by means of the comparison of the obtained results with benchmark solutions and the confirmation that the order of accuracy of the obtained solutions matches the predictions, the certainty that the codes are correctly developed increases.

With respect to the resolution of the specific case on external flows it may be said that the scope has been accomplished, since this study focused primarily on the obtaining of robust and valid codes to be applied to the aerodynamics of airfoils. However, much more research should be done regarding strategies which would permit to obtain fully-converged solutions. Reynolds number ranges which ensure laminar flows have to be investigated, as well as proper domain dimensions and mesh distributions in order to gain in accuracy without shooting computational costs up. In addition, free flow cases may be investigated too, as they are the most natural conditions to which airfoils are subjected.

Furthermore, typical external flows over airfoils comprehend much more complex problems such as turbulent regimes and compressible flows. These aspects, though, are out of the scope of this study.

Then, the "natural step" forward concerning the study of external flows is to take a closer look to the turbulence phenomenon. In this study a brief introduction to turbulence has been done by solving the one-dimensional Burgers' equation. This has served the purpose of understanding the behaviour of each of the terms of the Navier-Stokes equation in a turbulent flow, and the mechanics involved in the formation of smaller and smaller eddies every time. However, future research may involve the Direct Numerical Simulation (DNS) of 3D turbulent flows and its resolution by turbulence modelling, such as Large-Eddy Simulation (LES).

The analysis of turbulent flows by DNS do not require different codes to the already developed yet at all. However, in order to perform proper turbulence simulations a

series of conditions on symmetry and skew-symmetry of the matrixes involved in the resolution of the equations must be satisfied [19]. Despite the codes developed were intended to solve laminar cases, these symmetry preserving conditions were taken into account. Nevertheless, if a turbulent case were to be simulated, further reviews of this conditions should be done. Besides, an statistical analysis of the solution must be done in order to stop the simulation (it does not reach steady state) [20]. Another aspect that must be taken into account is the fact that to obtain a good solution by a DNS the resolution of the mesh has to be extremely fine, so most certainly the simulation would not be suitable for a normal computer, as it demands high computational resources.

The final target of the study on external flows would be the resolution of compressible flows. The codes required to solve such cases may differ substantially from the ones developed in this study intended to solve both laminar and turbulent cases, as they are developed under the hypothesis of incompressibility.

Since most of the general and commercial aviation is capable to fly at speeds where compressibility effects may not be neglected (typical commercial cruise speeds are around Mach 0.80) it seems obvious that compressible flows must be studied. These flows are also very turbulent, so the study of this two aspects is essential to simulate and understand the vast majority of the cases of engineering usefulness.

As a summary of the future tasks necessary to reach a good command of CFD and in particular of the external flows of aerospace engineering interest, the following list is presented. In it the tasks are ordered chronologically.

- Further analysis and investigation focused on the laminar resolution of airfoils, including free flow analysis.
- Review of the developed codes in order to make them suitable to turbulent flow simulations.
- Resolution of 3D turbulent cases by Direct Numerical Simulation (DNS).
- Resolution of 3D turbulent cases by turbulence modelling. The most appropriate model to begin with is the Large-Eddy Simulation (LES).
- Study of compressible flows and the numerical methods and schemes associated.
- Development of codes able to solve both turbulent and compressible flows.
- Resolution, validation and verification of a specific case. This case would range from the analysis of a commercial aircraft airfoil to the atmosphere re-entry of a probe or a rocket launch.

## 9 Study's Budget

Regarding the budget estimation of this study four main aspects have to be taken into account:

- Human resources: this paper has been elaborated by a non-graduated aerospace engineering student (currently at last year of an Undergraduate Degree). The hourly payment that a student in such career stage would receive is difficult to estimate, for the majority of the employed ones are enrolled in internships or apprenticeships and the salaries are very variable. Therefore, it has been considered the current minimum wage in Spain[21], in order to set an inferior limit. The total amount of hours devoted to the study is 300, distributed along 114 days (3.68 months).
- Software: this includes all the programmes and software licenses that have been used during the study. Its costs are proportional to the time-extension of the study with respect to the life expectancy of the computer, as it is assumed each time the computer is replaced, the newest licenses are bought.
- Hardware resources: it refers to the computer that was used. Following the requirements, the generated codes had to be suitable for its execution on a standard computer (avoiding the use of supercomputers, clusters, etc.). Thus, this aspect would include the laptop with which the programmes have been developed. For the cost computation, laptop's life expectancy will be assumed to be 5 years while its acquisition cost was 1,200.00 €. Therefore, the proportional part corresponding to its usage in the study with respect to its total life expectancy will be due.
- Energy resources: it basically takes into account the electricity consumed by the computer along the study. The average power consumption of the computer and the hours in which the computer has been active are to be taken into account.

The budget is presented in the table below:

| Concept          | Item                      | Unit price     | Unities            | Total             |
|------------------|---------------------------|----------------|--------------------|-------------------|
| Human resources  | Payment                   | 648.60 €/month | 3.68<br>(114 days) | 2,386.85 €        |
|                  |                           |                |                    | <b>2,386.85 €</b> |
| Software         | Microsoft Office License  | 1.15 €/month   | 3.68               | 4.23 €            |
|                  | Dev-C++                   | 0.00 €/month   | 3.68               | 0.00 €            |
|                  | Matlab Education License  | 8.33 €/month   | 3.68               | 30.65 €           |
|                  |                           |                |                    | <b>34.88 €</b>    |
| Hardware         | Laptop Acer Aspire 5830TG | 20.00 €/month  | 3.68               | 73.60 €           |
|                  |                           |                |                    | <b>73.60 €</b>    |
| Energy resources | Electricity               | 0.22 €/kWh     | 40W·300h           | 2.64 €            |
|                  |                           |                |                    | <b>2.64 €</b>     |
|                  |                           |                |                    | <b>2,497.97 €</b> |

Table 20: Budget of the study.

## 10 Environmental impact

CFD provides a powerful alternative to established flow simulation techniques such as wind tunnels and many would agree with the idea that as CFD matures and improves it will replace them.

Many are the arguments which support this idea [22]: CFD provides a full domain analysis, it permits creating the models by means of CAD design instead of physical prototypes (therefore changes in the geometry of the models are easier and economically feasible), it provides better visualization of the results and the most significant advantage: in general terms its costs are significantly lower, which is basically due to the lower power consumption.

It is very difficult to compare power consumption of a CFD simulation with a wind tunnel simulation's, as there are too many parameters to take into account. Concerning the vast majority of cases, CFD needs much less amount of power: ordinary computers have power requirements of the order of some hundreds of W, and supercomputers or computer clusters may reach a figure of the order of kW. On the other hand, small and modest wind tunnels may have a power consumption around kW, while larger ones may reach MWs. Then, wind tunnels have a power consumption which is typically 1,000 or 10,000 times larger than the computer which would be used to perform the same analysis.

Nevertheless, it is obvious that CFD simulations require considerably more time to get results when compared to the direct simulations with a wind tunnel. Despite this fact, the celerity with which wind tunnels provide results does not compensate their larger power requirements, and therefore the total amount of energy remains favourable to the CFD analysis.

Besides the major impact of wind tunnels to the environment regarding power consumption, these constructions also affect environment since they usually require a vast extension of land to be installed, as well as the installation of large electrical transformation stations in its vicinity (figure 55).



Figure 55: World's largest wind tunnel at NASA Ames Research Center, in California. Extracted from [23].

Despite CFD's weaker environmental impact, wind tunnels are not to be replaced entirely by computational simulations since the former are more accepted in industry standard, they provide more realistic results concerning turbulence phenomena, they have been proved to be representative of real world situations as well as they permit the analysis of more complex projects. All in all, CFD and wind tunnels will most likely keep being used together in a symbiotic process where one technique fills in knowledge gaps left by the other.

## 11 References

- [1] Wikipedia, “Navier–Stokes existence and smoothness.” [Online]. Available: [http://en.wikipedia.org/wiki/Navier%20%93Stokes\\_existence\\_and\\_smoothness](http://en.wikipedia.org/wiki/Navier%20%93Stokes_existence_and_smoothness). [Accessed: 08-Jun-2015].
- [2] A. Jameson, “Computational fluid dynamics past, present and future.” [Online]. Available: [http://aero-comlab.stanford.edu/Papers/NASA\\_Presentation\\_20121030.pdf](http://aero-comlab.stanford.edu/Papers/NASA_Presentation_20121030.pdf). [Accessed: 21-May-2015].
- [3] CTTC, “Burgers’ equation in Fourier space.” pp. 1–8, 2014.
- [4] CTTC, “Numerical solution of convection.” pp. 1–15.
- [5] Wikipedia, “Jacobi method.” [Online]. Available: [http://en.wikipedia.org/wiki/Jacobi\\_method](http://en.wikipedia.org/wiki/Jacobi_method). [Accessed: 25-May-2015].
- [6] Wikipedia, “Gauss-Seidel method.” [Online]. Available: [http://en.wikipedia.org/wiki/Gauss%20%93Seidel\\_method](http://en.wikipedia.org/wiki/Gauss%20%93Seidel_method). [Accessed: 25-May-2015].
- [7] Wikipedia, “Tridiagonal Matrix Algorithm.” [Online]. Available: [http://en.wikipedia.org/wiki/Tridiagonal\\_matrix\\_algorithm](http://en.wikipedia.org/wiki/Tridiagonal_matrix_algorithm). [Accessed: 25-May-2015].
- [8] Wikipedia, “Conjugate gradient method.” [Online]. Available: [http://en.wikipedia.org/wiki/Conjugate\\_gradient\\_method](http://en.wikipedia.org/wiki/Conjugate_gradient_method). [Accessed: 25-May-2015].
- [9] Wikipedia, “Biconjugate gradient method.” [Online]. Available: [http://en.wikipedia.org/wiki/Biconjugate\\_gradient\\_method](http://en.wikipedia.org/wiki/Biconjugate_gradient_method). [Accessed: 25-May-2015].
- [10] Wikipedia, “Biconjugate gradient stabilized method.” [Online]. Available: [http://en.wikipedia.org/wiki/Biconjugate\\_gradient\\_stabilized\\_method](http://en.wikipedia.org/wiki/Biconjugate_gradient_stabilized_method). [Accessed: 25-May-2015].
- [11] CTTC, “A Two-dimensional transient conduction problem.” p. 3.
- [12] CTTC, “A Two-dimensional steady convection-diffusion equation: the Smith-Hutton problem,” no. 1. pp. 2–4.
- [13] F. X. Trias, “Verification of the code. The Method of Manufactured Solutions (MMS),” UPC.
- [14] CTTC, “Introduction to the Fractional Step Method.” pp. 1–10.
- [15] CTTC, “Course on Numerical Methods in Heat Transfer and Fluid Dynamics. Unit 4, Part 1.” .

- [16] U. Ghia, K. N. Ghia, and C. T. Shin, “High-Re solutions for incompressible flow using the Navier-Stokes equations and a Multigrid Method,” *J. Comput. Phys.*, vol. 48, pp. 387–411, 1982.
- [17] D. V. Davis, “Natural convection of air in a square cavity. A bench mark numerical solution.,” *Int. J. Numer. Methods Fluids*, vol. 3, pp. 249–264, 1983.
- [18] M. Breuer, J. Bernsdorf, T. Zeiser, and F. Durst, “Accurate computations of the laminar flow past a square cylinder based on two different methods: lattice-Boltzmann and finite-volume,” *Int. J. Heat Fluid Flow*, pp. 186–196, 2000.
- [19] CTTC, “Symmetry-preserving discretization of Navier-Stokes equations.” 2011.
- [20] CTTC, “Introduction to the DNS of turbulent flows — Part II,” no. June. 2012.
- [21] “Salario mínimo interprofesional.” [Online]. Available: <http://www.salariominimo.es/>. [Accessed: 24-May-2015].
- [22] J. D. Mcalpine, “Computational Fluid Dynamics or wind tunnel modeling?” pp. 1–5.
- [23] NASA, “Langley Research Center. Fact Sheets.” [Online]. Available: <http://www.nasa.gov/centers/langley/news/factsheets/WindTunnel.html>. [Accessed: 06-Jun-2015].
- [24] Wikipedia, “FLOPS,” 2015. [Online]. Available: <http://en.wikipedia.org/wiki/FLOPS>. [Accessed: 22-May-2015].
- [25] Wikipedia, “Diagonally dominant matrix.” [Online]. Available: [http://en.wikipedia.org/wiki/Diagonally\\_dominant\\_matrix](http://en.wikipedia.org/wiki/Diagonally_dominant_matrix). [Accessed: 25-May-2015].

